Investigating the Impact of Low-Intensity Therapeutic Ultrasound on Hormonal Regulation in the Pancreas

by John Kevin Hill

B.S. in Human Nutrition, Foods and Exercise, May 2020, Virginia Polytechnic and State University

A Dissertation submitted to

The Faculty of
The School of Engineering and Applied Science
of The George Washington University
in partial fulfillment of the requirements
for the degree of Doctor of Philosophy

May 19, 2024

Dissertation directed by

Vesna Zderic
Professor of Biomedical Engineering

The School of Engineering and Applied Science of The George Washington University certifies that John Kevin Hill has passed the Final Examination for the degree of Doctor of Philosophy as of April 1, 2024. This is the final and approved form of the Dissertation.

Investigating the Impact of Low-Intensity Therapeutic Ultrasound on Hormonal Regulation in the Pancreas

John Kevin Hill

Dissertation Research Committee:

Vesna Zderic, Professor of Biomedical Engineering, Dissertation Director

Aleksandar Jeremic, Professor of Biological Sciences, Committee Member

Anne-Laure Papa, Professor of Biomedical Engineering, Committee Member

Zhenyu Li, Professor of Biomedical Engineering, Committee Member

Rohan Fernandes, Associate Professor of Medicine, Committee Member

Dedication

I would like to dedicate this dissertation to my wife and my Dad. To my wife, for her unwavering support and steadfast belief in my ability to complete this degree with success, and for her constant encouragement and uplifting spirit that has sustained me throughout this journey. I am deeply grateful for your presence by my side; without you, reaching this milestone would not have been possible. And to my Dad, for nurturing within me a profound sense of curiosity and an insatiable thirst for knowledge from a young age. It is with gratitude that I acknowledge the values he has imparted on me, which have shaped my academic journey in ways I never imagined. To all who have provided guidance and assistance along this path, I extend my sincere appreciation.

Acknowledgments

I would like to thank my advisor, Dr. Vesna Zderic, for the support and aide she provided to me over the course of my studies. With her guidance, I was able to further myself as both a researcher and academic, learning how to solve problems in a different way through her positive mentorship. Likewise, I thank Dr. Aleksandar Jeremic, for his biological expertise and his willingness to answer any question, no matter how small, as thoroughly as possible. With his help, I broadened my knowledge outside of an engineering standpoint, and gained invaluable interdisciplinary experience that will be immensely useful in my future studies. I would also like to think my other committee members, Dr. Zhenyu Li, Dr. Anne-Laure Papa and Dr. Rohan Fernandes, for acting as a pillar of support both in my research and as a student in their classes. To Zderic lab member Andrew Chen, I would like to thank him for his reliable mentorship and willingness to teach me how to operate in this setting at the beginning of my graduate studies. I would also like to thank Zderic Lab members James Messina, for his assistance with a large part of the work done in this dissertation, and Bridget Thorpe for her support. Finally, I would like to thank Jeremic lab members, Lydia Burnett and Mallory Brayer, for the training, collaboration, and aide they provided in shaping my biological understanding of the problems we address in this dissertation.

Abstract of Dissertation

Investigating the Impact of Low-Intensity Therapeutic Ultrasound on Hormonal Regulation in the Pancreas

A clinically promising approach gaining momentum involves leveraging the therapeutic potential of low-intensity ultrasound to elicit systemic responses. Previous research conducted in our lab demonstrated the capacity of this modality to stimulate insulin release and induce biologically significant alterations in pancreatic tissue across various models, including primary cell lines and human pancreatic islet cells from donors. These findings have prompted further investigation into the effects of therapeutic ultrasound, both *in vitro* and *in vivo*, with a specific focus on hormonal regulation of pancreatic secretagogues, such as insulin and glucagon. One significant application of this approach lies in its potential as a non-invasive therapy for managing type 2 diabetes mellitus, a widespread and complex metabolic disorder. The appeal of therapeutic ultrasound in this context stems from its ability to induce bioeffects while selectively targeting deep tissues, facilitating the modulation of hormone secretion within the pancreas.

In this dissertation, we studied the usability of therapeutic ultrasound in combating type 2 diabetes, emphasizing its potential to induce specific biological effects deep within tissues. Using low-intensity ultrasound at a frequency of 800 kHz and an intensity of 0.5 W/cm², we conducted experiments on insulinoma β-cell lines, human pancreatic islet cell models, and excised rat pancreases to assess hormonal regulation at various physiological levels. Initially, we evaluated the influence of ultrasound on gene expression in human pancreatic islets using RT-qPCR analysis, placing emphasis on the

regulation of insulin, glucagon, amylin, and binding immunoglobulin protein (BiP). Subsequently, we employed computational modeling and experimental perfusion systems to investigate the effects of ultrasound on insulinoma β-cells, focusing on both thermal and mechanical impacts. Real-time analysis of insulin and amylin secretion was performed using enzyme-linked immunosorbent assays (ELISA) to assess the immediate effects of ultrasound treatment. Further experimentation involved applying low-intensity ultrasound to excised rat pancreases, followed by ELISA analysis of insulin, glucagon, and alpha-amylase secretion. The observed effects warrant continued exploration of therapeutic ultrasound in pancreatic modulation.

Future studies should aim to deepen our understanding of the mechanisms underlying ultrasound-mediated effects in the pancreas and their potential clinical implications for diabetes management.

Table of Contents

Dedication……..iii

Acknowledgements……...iv

Abstract of Dissertation……v

List of Figures……xi

List of Tables……xv

Glossary of Terms……..xvii

Specific Aims……...1

Chapter 1: Introduction……3

1.1 Diabetes and the Pancreas……..3

1.2 An Overview of Therapeutic Ultrasound……10

1.3 Bioeffects of Ultrasound……..14

1.4 Perfusion……..17

1.5 Previous Relevant Work……...19

1.6 Significance of Work……....27

Chapter 2: Optimizing Methods for Ultrasound Administration and Gene Expression Analysis……..29

2.1 Rationale……..29

2.2 Methods……29

2.2.1 Cell Culture……...29

2.2.2 INS Cell Plating……30

2.2.3 Cell Treatments……31

2.2.4 Ultrasound Administration……31

2.2.5 RNA Extraction and Quantification……..32

2.2.6 cDNA Synthesis……33

2.2.7 RT-qPCR……...34

2.3 Results……..37

Chapter 3: Analysis of Gene Expression of Donor Human Pancreatic Islet Cells……39

3.1 Methods……39

3.1.1 Donor Pancreatic Islet Cell Acquisition……39

3.1.2 Islet Cell Preparation……40

3.1.3 Cell Treatments……40

3.1.4 Ultrasound Administration……41

3.1.5 RNA Extraction and Quantification……..41

3.1.6 cDNA Synthesis……42

3.1.7 RT-qPCR……...42

3.1.8 Cell Viability……44

3.2 Results……..45

3.3 Discussion and Conclusions……53

3.4 Alternative Approaches……55

Chapter 4: Ultrasound Stimulation of Insulinoma β-cells in a Perfusion Chamber……..57

4.1 Computational Modeling……57

4.1.1 K-Wave……57

4.1.2 Perfectly Matched Layer (PML) ……..58

4.1.3 Establishment of Propagation Medium……59

4.1.4 Creation of Transducer Signal……..61

4.1.5 Pressure Simulation……..62

4.1.6 Thermal Simulation……..63

4.2 Conclusions……..65

4.3 Protein Secretion of Insulin in INS β-cell lines……...65

4.3.1 Quantification of Protein Secretion (ELISA) ……..65

4.3.1.1 Sandwich ELISA……...65

4.4 Methods……67

4.4.1 INS Cell Preparation……67

4.4.2 Preparation of Coverslips……..67

4.4.3 Coverslip Coating……68

4.4.4 Plating Coverslips……68

4.4.5 Preparation of Treatments……68

4.4.6 Perfusion……...69

4.4.7 Treatment Protocol and Sample Collection……..70

4.4.8 Rat/Mouse Insulin ELISA……71

4.5 Results……..73

4.6 Discussion……77

4.7 Conclusion……...81

4.7.1 Follow-Up Studies……81

Chapter 5: Analysis of Ultrasound-Mediated Effects on Protein Secretion in a Sliced Rat Pancreas Model……..83

5.1 Methods……83

5.1.1 Rat Pancreas Acquisition……...83

5.1.2 Ultrasound Administration……85

5.1.3 Sandwich ELISA……..86

5.1.4 Rat/Mouse Insulin ELISA…….86

5.1.5 Rat/Mouse Glucagon ELISA……89

5.1.6 Rat/Mouse Alpha-Amylase ELISA……...92

5.1.7 Statistical Analysis……94

5.2 Results……..94

5.2.1 Rat/Mouse Insulin ELISA…….94

5.2.2 Rat/Mouse Glucagon ELISA…….97

5.2.3 Rat/Mouse Alpha-Amylase ELISA……...99

5.3 Discussion……..101

5.4 Conclusions……105

5.4.1 Follow-Up Studies……..105

Chapter 6: Histological Analysis and Safety Testing of Ultrasound Frequencies on Rat Pancreas Tissue……107

6.1 Methods……..107

6.1.1 H&E Staining……..107

6.2 Results……107

6.3 Discussion……..108

6.4 Conclusions……109

References……111

Appendices……...123

Appendix I……...123

List of Figures

Figure 1. Overview of Pancreas; specific anatomical structures in the pancreas are shown, of special note are exocrine, delta, alpha, and beta cells, as well as exocrine pancreas cells—these are implicated in the context of the work presented here [7]. ……4

Figure 2. Role of Insulin and Glucagon in Blood Glucose Homeostasis; Insulin is released when blood sugar levels are high, stimulating glucose uptake from the blood. Glucagon is released in a low blood sugar condition, stimulating glycogen breakdown [11]. ……..6

Figure 3. Physiological Role of Amylin; Amylin is co-secreted with insulin by pancreatic β-cells and dysregulation can cause insulin resistance or inhibition of insulin release in respect to type 2 diabetes [19]. ……...8

Figure 4. Reflection, Scattering, Absorption of Ultrasound Waves; This image provides a display of the different fates that ultrasonic waves can have when administered to a given medium [31]. ……11

Figure 5. Near-field vs. Far-field in Ultrasound; In the near field, ultrasonic waves can be both circulating and propagating, as they reach the transition zone. Once past the transition zone, the wave will only propagate, extending to infinity in the far field—our work mainly focuses on interactions in the transition zone [36]. ……12

Figure 6. Acoustic Cavitation: Oscillation of a Microbubble When Exposed to Ultrasound Frequency of 2.5 MHz; This repetitive oscillation shown relates to noninertial cavitation [47]. ……...15

Figure 7. Perfusion; Schematic illustrating perfusion system with chamber, tubing, pump, and media reservoir [59]. ……...17

Figure 8. *In Vivo* Insulin Release; Compared to SHAM treatments, high glucose, ultrasound of 1 MHz and 800 kHz frequency all caused a significant release in insulin, with the greatest increase in insulin concentration shown at 800 kHz [72]. …….23

Figure 9. Insulin Levels in β-cells Exposed to 800 kHz Ultrasound; Insulin release was significant when ultrasound was administered for both 15 s and 5 min, with the greatest increase shown at 5 min exposure [73]. ……24

Figure 10. Insulin Output in Control and Perfused Wild-type, GLP-1 Receptor Knockout Mice Pancreas; It was shown that at higher concentrations of glucose infusion, perfused pancreases released a significant amount of insulin, illustrating a dose-dependent relationship [74]. ……...25

Figure 11. Results of Hormone Secretion Measured with an ELISA Kit after TUS Treatment; It was shown that with the ultrasound parameters used in this study, a significant increase in insulin content was observed, whereas no significant changes were shown with glucagon or amylase [75]. ……..27

Figure 12. Experimental Set-Up for Ultrasound Administration; 24-well culture plate was positioned above a water bath at 37°C, with the ultrasound transducer oriented in the water bath 2.5 cm below the surface of the plate. Ultrasound was applied for 5 min continuously, at a frequency of 800 kHz and intensity of 0.5 W/cm^2. …….32

Figure 13. PCR Plate for INS Cell Gene Expression Analysis; Samples were plated in each well for each treatment and corresponding gene. “A” corresponds to suspension from 1 dish, whereas “B” are samples that came from a different dish. …….....36

Figure 14. PCR Plate for Human Pancreatic Islet Cell Gene Expression Analysis; Samples were plated in duplicate for each treatment with the corresponding gene to analyze the different effects. …….44

Figure 15. Effects of Different Treatments on Fold Change of Insulin; average fold change values appear as dots on the graph. The x-axis pertains to treatment groups, while the y-axis shows the different fold change values. The figure is color-coded to differentiate each of the treatment groups compared to the control. The data is shown as mean +/- standard deviation with individual fold change values shown as dots on the graph. ……47

Figure 16. Effects of Different Treatments on Fold Change of Glucagon; average fold change values appear as dots on the graph. The x-axis pertains to treatment groups, while the y-axis shows the different fold change values. The figure is color-coded to differentiate each of the treatment groups compared to the control. The data is shown as mean +/- standard deviation with individual fold change values shown as dots on the graph. ……49

Figure 17. Effects of Different Treatments on Fold Change of Amylin; average fold change values appear as dots on the graph. The x-axis pertains to treatment groups, while the y-axis shows the different fold change values. The figure is color-coded to differentiate each of the treatment groups compared to the control. The data is shown as mean +/- standard deviation with individual fold change values shown as dots on the graph. ……51

Figure 18. Effects of Different Treatments on Fold Change of BiP; average fold change values appear as dots on the graph. The x-axis pertains to treatment groups, while the y-axis shows the different fold change values. The figure is color-coded to differentiate each of the treatment groups compared to the control. The data is shown as mean +/- standard deviation with individual fold change values shown as dots on the graph. ….....52

Figure 19. Illustration of Perfusion Chamber with Dimensions of Material Layers; From top to bottom in the system, we applied gel to couple the transducer to the chamber, followed by the coverslip with the INS cells adhered to the surface, with the media perfusing through the system and the bottom of the plexiglass layer. …….....59

Figure 20. Experimental Space for Simulation; In this simulation, the ultrasound transducer is oriented at the top of the figure, followed by the gel, glass coverslip, INS cell layer, media, and the plexiglass layer—these are separated based on points in the y-direction. The units for the x- and y-axis correspond to each point within the space, while the legend on the right of the figure is in units of m/s, relating to medium sound speed……..61

Figure 21. Results of Acoustic Pressure Simulation; Most of the pressure exerted by the transducer is emitting from the actual location of the transducer, with an observed gradual attenuation throughout the experimental space. ……63

Figure 22. Temperature After Heating from Ultrasound Administration; Temperature increases are shown in yellow near the ultrasound transducer and the plexiglass layer of the experimental space. …….64

Figure 23. Volume Rate of Heat Deposition; No significant heat deposition was shown throughout the system, with any responses shown near the ultrasound transducer……...65

Figure 24. Sandwich ELISA Principle; Specific steps in the mechanism of how this kit works to analyze protein secretion [102].…….....66

Figure 25: Perfusion Chamber and Plexiglass Layer; The coverslip is adhered to the plexiglass layer via high-vacuum grease and the whole component is sealed within the chamber and screwed shut as shown. Tubing is fed through the inlet and outlet of the plexiglass layer to allow the perfusate to travel through to reach the cells……...70

Figure 26. Changes in Insulin Concentration (ng/mL) Over Time in a Perfused System; Baseline measurements were taken 30 min prior to treatment administration, through collection of 5 mM glucose KBS. Treatments began at t = 0 min with 800 kHz ultrasound for 5 min continuously, followed by a 30 min treatment of 20 mM high glucose and a 5 min treatment of 50 μM thapsigargin. Specific treatments are differentiated by color, shown in the legend on the right. Between each treatment, system was perfused with 5 mM glucose KBS to wash out previous treatment. "**" denotes significant data with a $p < 0.01$ and "***" denotes significant data with a $p < 0.001$ ($n = 3$). ……77

Figure 27. Insulin Standard Calibration Curve; mean absorbance for each standard was plotted on the x-axis, with the corresponding insulin concentration for the standards was plotted on the y-axis in ng/mL. A line of best fit to interpolate the insulin concentration for each sample and R^2 value to assess the goodness of fit for the line was added to the curve. ……88

Figure 28. Glucagon Standard Calibration Curve; mean absorbance for each standard was plotted on the x-axis, with the corresponding glucagon concentration for the standards was plotted on the y-axis in pg/mL. A line of best fit to interpolate the glucagon concentration for each sample and R^2 value to assess the goodness of fit for the line was added to the curve. ……91

Figure 29. Alpha-Amylase Standard Calibration Curve; mean absorbance for each standard was plotted on the x-axis, with the corresponding alpha-amylase concentration for the standards was plotted on the y-axis in IU/mL. A line of best fit to interpolate the alpha-amylase concentration for each sample and R^2 value to assess the goodness of fit for the line was added to the curve. ……...93

Figure 30. Insulin Fold Change 5 min, 35 min Post-Ultrasound Treatment Compared to t = 0 min; Fold Change is plotted on the y-axis compared to each time point, plotted on the x-axis. Individual data points for each rat pancreas are shown as dots. ……97

Figure 31. Glucagon Fold Change 5 min, 35 min Post-Ultrasound Treatment Compared to t = 0 min; Fold Change is plotted on the y-axis compared to each time point, plotted on the x-axis. Individual data points for each rat pancreas are shown as dots. "*" corresponds to significant findings ($p < 0.05$). …….....99

Figure 32. Alpha-Amylase Fold Change 5 min, 35 min Post-Ultrasound Treatment Compared to t = 0 min; Fold Change is plotted on the y-axis compared to each time point, plotted on the x-axis. Individual data points for each rat pancreas are shown as dots. ……..101

Figure 33. Histological Analysis of Sham vs. Ultrasound-Treated Rat Pancreases; Pancreases were minced in to 2 sections, 1 serving as a sham and the other exposed to ultrasound at 800 kHz at intensity of 0.5 W/cm^2 for 5 min continuously. Sections of 10x and 40x of both sham-treated and ultrasound-treated pancreases appear next to each other in the figure……..108

List of Tables

Table 1. Primer Sequences for Tested Genes; Primer sequences were derived from rat primers for the housekeeping gene, actin, and the tested genes, insulin, glucagon, amylin, and BiP. …….35

Table 2. PCR Master Mix; Components of the PCR master mix were combined based on calculations of the number of samples + 2 to create enough mix to dispense into each well for the PCR reaction. …….35

Table 3. Summary of Fold Change Values for Optimization with INS cells; A fold change of greater than 1 indicates an upregulation in expression and a fold change of less than 1 reflects a downregulation. …….37

Table 4. Primer Sequences for Tested Genes; Primer sequences were derived from human samples for each of the tested genes. ……43

Table 5. Summary of Fold Change Values for each Treatment on Insulin Expression; A fold change of greater than 1 signifies an upregulation in expression, whereas a fold change of less than 1 indicates a downregulation. ……..46

Table 6. Summary of Fold Change Values for each Treatment on Glucagon Expression; A fold change of greater than 1 signifies an upregulation in expression, whereas a fold change of less than 1 indicates a downregulation. ……..48

Table 7. Summary of Fold Change Values for each Treatment on Amylin Expression; A fold change of greater than 1 signifies an upregulation in expression, whereas a fold change of less than 1 indicates a downregulation. ……..50

Table 8. Summary of Fold Change Values for each Treatment on BiP Expression; A fold change of greater than 1 signifies an upregulation in expression, whereas a fold change of less than 1 indicates a downregulation. …….50

Table 9. Descriptive Statistics for Fold Change Data of Insulin, Glucagon, Amylin and BiP; Mean, standard deviation (STD), standard error of mean (SEM) and p-value are shown for each condition. ……...53

Table 10. Defining Properties of Propagation Medium for Perfusion System; Values were obtained from a literature surface to identify the different data necessary for each parameter that k-wave called for. ……60

Table 11. Relevant Definitions of Components in an ELISA; Streptavidin-HRP serves as the detection antibody, with TMB substrate as the substrate solution to continue the reaction. …….67

Table 12. Treatment Protocol and Sample Collection for Perfusion; A 30 min equilibration with 5 mM glucose KBS was done, followed by 5 min ultrasound, 30 min 20 mM high glucose, 5 min 50 μM thapsigargin and a 10 min period with 5 mM glucose KBS. In between each treatment, system was flushed with 5 mM glucose KBS to wash out previous treatment. ……...71

Table 13. Changes in Insulin Concentration (ng/mL) Over Time After Administration of 800 kHz Ultrasound at intensity of 0.5 W/cm^2 for 5 min, continuously; Concentration for each data set is shown in the table with mean and standard error of mean. "**" denotes significant data ($p < 0.01$). ……74

Table 14. Changes in Insulin Concentration (ng/mL) Over Time After Administration of 20 mM High Glucose for 30 min; Concentration for each data set is shown in the table with mean and standard error of mean. "*" = ($p< 0.05$), "**" = ($p < 0.01$), "***" = ($p <0.001$). ……74

Table 15. Changes in Insulin Concentration (ng/mL) Over Time After Administration of 50 μM Thapsigargin for 5 min; Concentration for each data set is shown in the table with mean and standard error of mean. ……76

Table 16. Manipulations of Rats Before Pancreas Acquisition; Manipulations were done at different periods of life for the rat donors. All rats were from the Sprague Dawley Strain and were female, with an age of 55 weeks at sacrifice. ……..85

Table 17. Contents of Rat/Mouse Glucagon ELISA kit; Standards and wash buffer required preparation before starting the experiment, following the protocol provided. 89

Table 18. Insulin Fold Change Data Post-Ultrasound Treatment; t = 0 min served as an internal control with collection prior to ultrasound treatment. Data for t = 5 min and t = 35 min was compared to t = 0 min to assess the impact of ultrasound treatment on the rat pancreases. Average fold change, standard deviation, and p-value is shown at bottom of the table to determine conclusions. …….....96

Table 19. Glucagon Fold Change Data Post-Ultrasound Treatment; t = 0 min served as an internal control with collection prior to ultrasound treatment. Data for t = 5 min and t = 35 min was compared to t = 0 min to assess the impact of ultrasound treatment on the rat pancreases. Average fold change, standard deviation, and p-value is shown at bottom of the table to determine conclusions. "*" denotes significant data ($p < 0.05$). ……98

Table 20. Alpha-Amylase Fold Change Data Post-Ultrasound Treatment; t = 0 min served as an internal control with collection prior to ultrasound treatment. Data for t = 5 min and t = 35 min was compared to t = 0 min to assess the impact of ultrasound treatment on the rat pancreases. Average fold change, standard deviation, and p-value is shown at bottom of the table to determine conclusions. ……..100

Glossary of Terms

RT-qPCR – Reverse Transcription-Quantitative Polymerase Chain Reaction Analysis; a laboratory technique used to quantify gene expression as quantification cycle (Cq) values

Cq Value – Quantification Cycle Value

FC – Fold Change

GLP-1 Receptor – Glucose-like peptide 1 receptor

IAPP – Islet Amyloid Polypeptide

BiP – Binding Immunoglobulin Protein

UPR – Unfolded Protein Response

ER – Endoplasmic Reticulum

GSIS – Glucose-Stimulated Insulin Secretion

ATAC – Acoustically Targeted Chemogenetics

FUS-BBBO – Focused Ultrasound Blood–Brain Barrier Opening (FUS-BBBO)

AAV – Adenoassociated Virus

TNF-α – Tumor-Necrosis Factor

DREADDS – Designer Drugs

Tn – Tunica Mycin

Tg – Thapsigargin

Hg – High Glucose

ELISA – Enzyme linked immunosorbent assay; a chemical assay utilized in protein secretion studies to detect and quantify hormones

KBS – Krebs Ringer Buffer; Krebs Bicarbonate Solution

pFUS – Pulsed Focused Ultrasound

FUS – Focused Ultrasound

US – Ultrasound

TUS – Therapeutic Ultrasound

ROS – Reactive Oxygen Species

RT-qPCR – Reverse Transcription-Quantitative Polymerase Chain Reaction Analysis; a laboratory technique used to quantify gene expression as quantification cycle (Cq) values

INS β-cell Line – Insulinoma β-cell Line; Cell line derived from rat donor

Specific Aims

Specific Aim 1. To analyze gene expression of donor human pancreatic islet cells after administration of low-intensity, continuous ultrasound. Optimization of the gene expression protocol was done through use of rat INS β-cell lines and reverse transcription-quantitative polymerase chain reaction analysis (RT-qPCR), using ultrasound parameters that have been previously shown to induce insulin release in a rat β-cell model. Here, we apply these protocols to a donor human islet cell model to analyze gene expression of key pancreatic hormones after administration of low-intensity, continuous ultrasound. We express these genetic changes through analysis of quantification cycle (Cq) values and fold change, to determine how much the expression was changed after administration. We also analyze the safety of these ultrasound frequencies on the human islet cells through the use of a trypan blue dye exclusion test.

Specific Aim 2. To examine protein secretion of insulinoma β-cells after administration of low-intensity, continuous ultrasound using a perfusion chamber. In this aim, we develop an *in vitro* system for ultrasound stimulation of insulin release; to do so, we refined the mechanics of perfusion chamber through use of modeling with k-wave software in MATLAB to provide a final design. From there, we measure protein secretion of insulin in INS β-cell lines using the perfusion chamber after continuous ultrasound application for 5 minutes at 800 kHz with intensity of 0.5 W/cm^2; quantification of protein secretion was done using specific rat/mouse ELISA kits.

Specific Aim 3: Testing of safety and effectiveness of ultrasound application for stimulation of insulin release in a minced diabetic rodent pancreas model *in vitro*. Here, we test the effectiveness of this modality in stimulating insulin, glucagon and alpha-

amylase release from the rat pancreas model through use of ELISA kits to quantify fold change between ultrasound-treated slices and an internal control. We use a SpectraMax iD5 spectrometer to measure the optical density values of each condition, followed by generation of a standard curve to calculate protein concentration. Data is expressed as fold change between treated pancreas slices at different time points vs. an internal control. We analyze the safety of this testing through use of histological analysis and image analysis.

Chapter 1: Introduction

1.1 Diabetes and the Pancreas

Diabetes mellitus is a heterogeneous metabolic disease that effects more than 37 million Americans in the United States [1]. Globally, this number rises to almost 415 million, with a projected total of half a billion to be effected by 2040 [2]. Diabetes affects the pancreas, as well as the whole body with severe side effects in the kidneys, eyes, and other areas. This disease contains three main types: type 1, type 2, and gestational diabetes, all of which have their own unique morbities. However, for the purposes of this research, our lab has focused mainly on the treatment of type 2 diabetes, as previous work has shown the efficacy of utilizing therapeutic ultrasound to combat this disease.

The most prevalent form of diabetes, type 2 diabetes, effects more than 90-95% of the American population who are diagnosed with this disease [3]. Generally, this form of the disease effects adults over the age of 45, but recently, more children, teens and young adults have been known to suffer from this disease. Specifically, it results from the interplay of multiple metabolic abnormalities including decreased insulin sensitivity of peripheral tissues, insufficient insulin secretion from pancreatic β-cells, and amylin-derived islet β-cell death [4]. It is believed that a sharp rise in blood glucose due to insulin resistance leads β-cells to try to compensate and adapt to the hyperglycemia by hypersecretion of insulin. While such compensation may reflect normal glucose homeostasis temporarily, β-cell exhaustion eventually sets in, resulting in reduced insulin secretion and hypoinsulinemia [4], [5]. This eventually leads to chronic hyperglycemic levels resulting in progressive loss of β-cell mass with a prolonged increase in the rate of β-cell apoptosis, a process often referred to as glucotoxicity.

Although diabetes has wide-ranging effects on different organs in the body, its main pathogenicity involves the pancreas. The pancreas has both exocrine and endocrine functions, aiding in digestion and regulation of blood sugar [6]. As an exocrine organ, the pancreas produces enzymes such as trypsin and chymotrypsin, both of which digest proteins. Additionally, it releases amylase and lipase to break down carbohydrates and fats, respectively. From an endocrine perspective, and that of which is greatly affected by diabetes, the pancreas releases both insulin and glucagon to regulate blood sugar. The endocrine component of the pancreas is comprised of islet cells, or islets of Langerhans, that both create and release these two critical hormones into the bloodstream. In turn, this maintains blood sugar levels of other important organs, such as the brain, liver, and kidneys. An overview of the anatomy of the pancreas is shown in *Figure 1*.

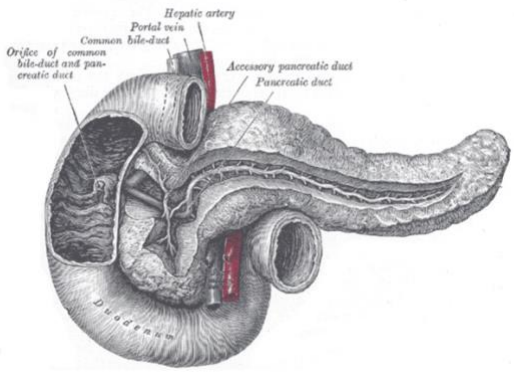

Figure 1: Overview of Pancreas; specific anatomical structures in the pancreas are shown, of special note are exocrine, delta, alpha, and beta cells, as well as exocrine pancreas cells—these are implicated in the context of the work presented here [7].

Insulin is secreted by β-cells in the islets of Langerhans and functions in maintaining normal blood sugar levels by facilitating glucose uptake when blood glucose is high [8]. This peptide hormone is secreted by the pancreas and plays crucial roles in maintaining homeostasis of blood glucose levels through facilitation of glucose uptake in

organs such as the liver, skeletal muscle, and adipose tissue. Secondarily, this hormone functions in the regulation of carbohydrate, lipid, and protein metabolism, as well as cell division and growth—all of which aide in maintaining blood glucose. However, dysregulation of insulin's hormone levels can cause many negative effects, such as insulin resistance and compensatory hyperinsulinemia, both of which are directly implicated in diabetes. Insulin resistance refers to elevated insulin levels that cause impaired sensitivity to insulin-mediated glucose uptake. This leads to hyperglycemia, or increased blood glucose levels, eventually causing prediabetes and type 2 diabetes [9]. Hyperinsulinemia, which directly corresponds to insulin resistance, occurs when pancreatic β-cell (i.e. islet cells) secretion increases to maintain a normal blood glucose level when peripheral tissue insulin resistance occurs [8]. Further, this complication is characterized by unrestrained insulin signaling, which greatly increases the likelihood of development of obesity, type 2 diabetes, and cardiovascular disease [10]. Generally, both insulin and glucagon function to counterbalance the effects of the other, ultimately stabilizing blood glucose; if dysfunction of one of these hormones occurs, many negative side effects can occur; most of which relate to development of diabetes. The role of insulin and glucagon in blood glucose homeostasis is further illustrated in *Figure 2*.

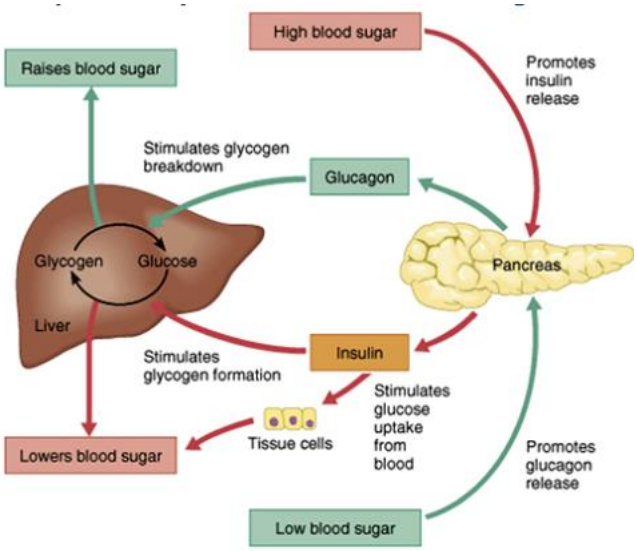

Figure 2: Role of Insulin and Glucagon in Blood Glucose Homeostasis; Insulin is released when blood sugar levels are high, stimulating glucose uptake from the blood. Glucagon is released in a low blood sugar condition, stimulating glycogen breakdown [11].

Controlling type 2 diabetes is often difficult as pharmacological management routinely requires complex therapy with multiple medications and loses its effectiveness over time. Treatments for type 2 diabetes include medications such as metformin, sulfonylureas, meglitinides, thiazolidinediones, DPP-4 inhibitors, GLP-1 receptor agonists, and SGLT2 inhibitors [5]. More specifically, a popular GLP-1 receptor agonist that has been gaining traction in the treatment of this disease, Ozempic, works to selectively bind to and activate GLP-1 receptors, in turn lowering fasting a post-prandial blood glucose by stimulating insulin secretion [12]. Disease progression and further β-cell failure requires for the patient to be administered insulin through injections, pens or insulin pumps. Further, current pharmacological treatments have many potential side effects and may accelerate the progression of the disease by promoting β-cell failure. Medication also comes in doses not optimized for individual patients; leading to unwanted side effects. Due to these complications, significant research has been executed to determine an alternative

approach to treat this disease, with strides being made in the field of therapeutic ultrasound application to induce biological effects [13]. Further, therapeutic applications of ultrasound rely on the ability to selectively focus deep within tissues and produce thermal and mechanical bioeffects noninvasively.

Other hormones that warrant exploration with therapeutic ultrasound exist, such as amylin, which can have wide-reaching effects both in the pancreas and related to diabetes. This hormone, also referred to as islet amyloid polypeptide (IAPP), is a hormone produced alongside insulin by pancreatic β-cells, playing a pivotal role in managing glucose levels and satiety [14]. Synthesis of amylin involves the conversion of proislet amyloid polypeptide (proIAPP), a precursor to amylin, to mature amylin, which is then stored separately from insulin granules [15]. Upon glucose stimulation, amylin is released into the bloodstream alongside insulin, peaking after meals and decreasing during fasting. Its functions include regulating glucose homeostasis by inhibiting glucagon secretion, delaying gastric emptying, and curbing hepatic glucose output [16]. Additionally, amylin contributes to satiety and reduces food intake by acting centrally in the brain [17]. Dysregulation of amylin is implicated in conditions such as type 1 and type 2 diabetes, where reduced amylin levels or impaired secretion contribute to glucose dysregulation and increased risk of complications [17], [18]. The physiological role of amylin is further described in *Figure 3*.

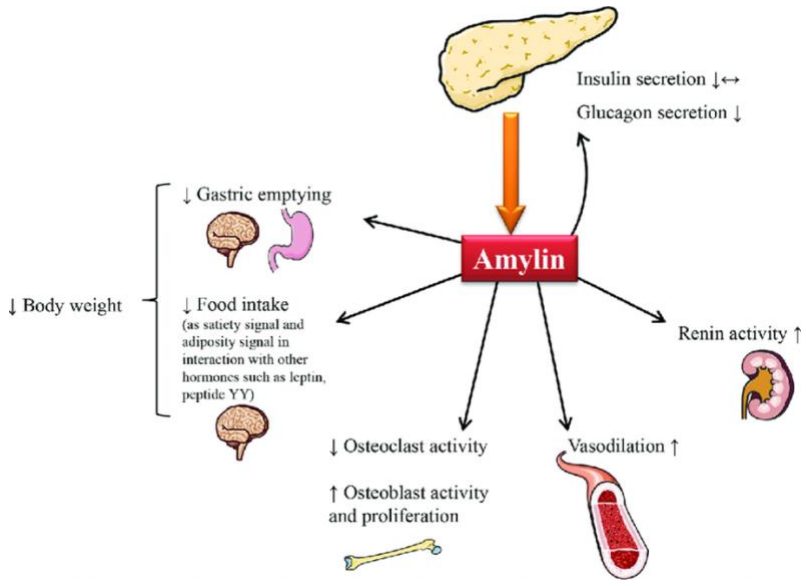

Figure 3: Physiological Role of Amylin; Amylin is co-secreted with insulin by pancreatic β-cells and dysregulation can cause insulin resistance or inhibition of insulin release in respect to type 2 diabetes [19].

In the pancreas, amylin is primarily secreted alongside insulin by β-cells in the islets of Langerhans, reflecting their coordinated roles in glucose metabolism. In type 1 diabetes, amylin deficiency exacerbates impaired glucose regulation and hypoglycemia risk due to diminished inhibition of glucagon secretion [20]. In type 2 diabetes, impaired amylin secretion and amyloid deposition in pancreatic islets contribute to beta cell dysfunction and worsen glucose dysregulation. Moreover, dysregulation of amylin signaling is associated with obesity, where reduced circulating amylin levels may lead to increased food intake and impaired satiety signaling [20], [21]. Amylin's relationship with insulin is characterized by synergistic actions in regulating glucose homeostasis, with both hormones being co-secreted in response to elevated blood glucose levels [22]. Understanding the intricate interplay between amylin and insulin is crucial for developing targeted therapeutic strategies for diabetes and metabolic disorders.

Finally, an important protein that is key in understanding the strategies outlined here and how we can analyze hormonal regulation in the pancreas is binding immunoglobulin protein (BiP). BiP, also known as glucose-regulated protein 78 (GRP78), is a pivotal molecular chaperone residing in the endoplasmic reticulum (ER) of eukaryotic cells [23]. Initially recognized for its role in immunoglobulin folding and secretion in B cells, this protein's functions extend far beyond the immune system, impacting numerous cellular processes. Synthesized as a precursor protein, BiP undergoes post-translational modifications, including glycosylation, within the ER [24]. Its primary function lies in ensuring proper protein folding, assembly, and trafficking within the ER lumen, crucial for maintaining cellular homeostasis. Additionally, BiP plays a pivotal role in the unfolded protein response (UPR), a stress response pathway activated during ER stress conditions, such as protein misfolding [25]. BiP's multifaceted roles encompass protein folding and quality control, ER stress response, regulation of ER calcium homeostasis, and modulation of apoptosis pathways [25], [26]. Its stable abundance within the ER and consistent expression levels make BiP an ideal control for comparing the actions of other hormones or signaling molecules. Its presence influences protein folding and trafficking, indirectly impacting the cellular response to hormonal stimuli. Furthermore, BiP's integration into cellular stress response pathways, such as the UPR, underscores its broader significance beyond hormone regulation. Utilizing BiP as a control allows researchers to assess changes in cellular responses to hormonal stimuli accurately. Its involvement in protein folding, ER homeostasis, and stress response pathways provides valuable insights into cellular physiology and disease mechanisms; by understanding BiP dynamics and its interactions

with hormonal pathways, researchers gain a deeper comprehension of cellular processes and can elucidate novel therapeutic targets for various diseases.

1.2 An Overview of Therapeutic Ultrasound

Although ultrasound has found applications in clinical settings as far back as 1942, it was not until the mid-1950s that this diagnostic imaging method gained widespread acceptance and utilization in both medical practice and research endeavors [27]. Ultrasound, in essence, pertains to the propagation of the frequency of > 20 kHz sound waves through a given medium [28]. This modality harnesses the capabilities of a specialized transducer that is capable of emitting and receiving reflected sound waves, thereby furnishing valuable insights pertaining to tissue characteristics, blood flow dynamics, and the identification of pathological anomalies such as tumors. Beyond its diagnostic utility, ultrasound serves as a versatile tool for non-invasively visualizing various anatomical structures within the human body [13]. Moreover, it can be employed in a functional capacity to assess parameters such as blood velocity, tissue elasticity, and the intricate details of organ structures. Furthermore, ultrasound exhibits a plethora of applications, with therapeutic ultrasound, for instance, being employed for thermal ablation of specific target tissues or the modulation of cellular membranes to facilitate drug delivery and influence cellular behavior.

The propagation of ultrasound through a given medium instigates mechanical oscillations within the constituent particles, thereby leading to the production of sound waves. These waves, upon encountering distinct structures along their path, undergo processes such as reflection or absorption [29]. These ultrasound waves are represented as sine curves, featuring fundamental characteristics such as wavelength, amplitude

(indicative of wave strength), and frequency. Notably, the amplitude and intensity of ultrasound waves may diminish as they traverse through biological tissues, a phenomenon recognized as attenuation [30]. Attenuation encompasses various outcomes for ultrasound waves, including reflection, refraction, scattering, and absorption. These fundamental concepts are further shown in *Figure 4*.

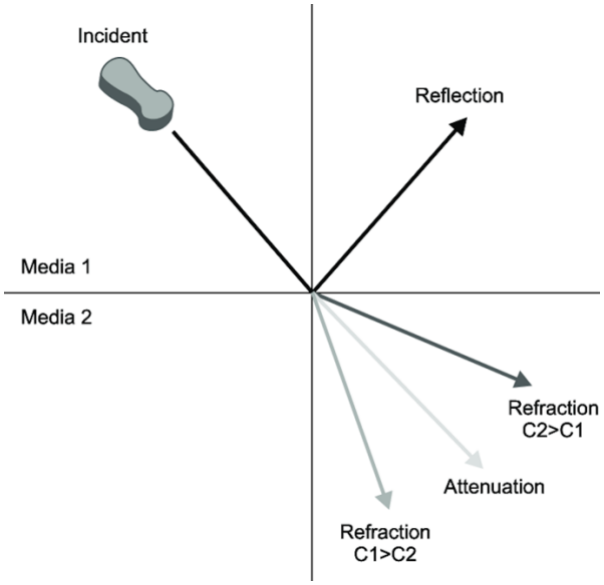

Figure 4: Reflection, Scattering, Absorption of Ultrasound Waves; This image provides a display of the different fates that ultrasonic waves can have when administered to a given medium [31].

The generation and reception of ultrasound signals hinge on a transducer equipped with a functional component constructed from piezoelectric materials capable of converting electrical energy into mechanical energy [32]. Additionally, the properties of the ultrasound beam deserve mention due to their significance in characterizing sound waves. Ultrasound typically operates in two distinct fields: the near-field and the far-field. The near-field, situated proximate to the transducer, is characterized by a converging beam [32]. This convergence results from the interplay of constructive and destructive

interference patterns that manifest as individual wave patterns interact. Consequently, the ultrasound beam in the near-field is tightly collimated and confined to the dimensions of the transducer's active surface area. Pressure characteristics in the near-field are profoundly influenced by these interference wave patterns, with peak ultrasound pressure occurring at the far end of the near-field. Conversely, as ultrasound frequencies progress into the far-field, pressure variations exhibit a rapid decline. The far-field, designated as the region where the beam diverges, is typified by a decrease in ultrasound intensity with increasing distance from the transducer. There is also what is known as the distance from the far field (dff), or the measurement referring to the distance away from the transducer at which the field transitions from near-field to far-field [33]. The dff distance is determined by the properties of the transducer used, such as the frequency, transducer aperture, and acoustic impedance, among other things [34]. Within the transition zone, it has been shown that treatment efficiency, treatment consistency and safety of ultrasound delivery are all improved, supporting the use of ultrasound experiments that make use of this distance [35]. Further depiction of the near-field and far-field within ultrasound propagation can be seen in *Figure 5*.

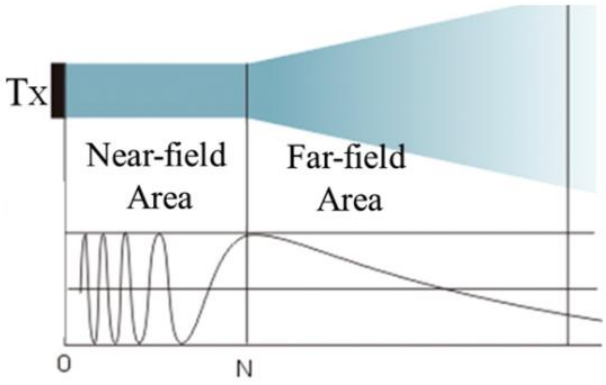

Figure 5: Near-field vs. Far-field in Ultrasound; In the near field, ultrasonic waves can be both circulating and propagating, as they reach the transition zone. Once past the transition zone, the wave will only propagate, extending to infinity in the far field—our work mainly focuses on interactions in the transition zone [36].

Ultrasound serves as an indispensable tool for noninvasive diagnostic imaging and therapy. It is widely recognized for its noninvasive nature, real-time imaging capabilities, cost-effectiveness, and portability [37]. Further, current research suggests that promising new therapeutic applications of ultrasound can be utilized in the delivery of drugs and genetic material, thrombolysis, and tumor therapy. The safety and efficacy of diagnostic ultrasound are well-established, with regulatory standards in place to monitor acoustic output levels. For example, pulsed ultrasound (PUS) is used widely as a diagnostic imaging tool for specialized imaging applications, such as imaging of the eye or skin, or for imaging cellular structures using acoustic microscopy. Understanding the acoustic mechanisms of ultrasound interaction with tissues has led to the development of advanced imaging techniques. This review emphasizes the distinction between the acoustic mechanisms used in diagnostic and therapeutic applications of ultrasound. While diagnostic ultrasound aims to minimize tissue interaction, therapeutic ultrasound relies on direct tissue interaction to produce beneficial bioeffects.

Irrespective of diagnostic ultrasound, therapeutic applications of this modality rely on the ability to focus within tissues and produce a therapeutic bioeffect noninvasively [38]. Therapeutic applications of ultrasound rely on the ability to selectively focus deep within tissues and produce thermal and mechanical bioeffects noninvasively. Many of the mechanical effects of therapeutic ultrasound are mediated through acoustic cavitation [39], and other factors including acoustic radiation forces, acoustic microstreaming and shear stress. Acoustic cavitation enhances therapeutic effects through coupling with microbubbles. This type of cavitation refers to the formation, growth or collapse of a microbubble that is induced by an ultrasound wave. The mechanical effects of ultrasound

have been shown to cause modification of cell membrane permeability leading to different rates of transports of ions and molecules across the membrane. Ultrasound-induced changes in the cell membrane permeability have been strongly correlated with cavitation activity, which leads to formation of reversible pits in the cell membranes thus allowing delivery of genes, drugs, and macromolecules into the cells or release of the cellular components.

On the other hand, ultrasound frequencies can cause thermal effects, largely seen as an increase in temperature with application. The thermal effects of ultrasound occur when a tissue absorbs the some of the energy from the wave and converts it to heat.

1.3 Bioeffects of Ultrasound

Ultrasound-induced bioeffects have great potential for utilization in treatment of many different diseases [39]. These bioeffects can be generated through heating, or other nonthermal mechanisms, such as acoustic cavitation, or mechanically-induced changes, such as increases in rates of transports of ions and molecules across the membrane [13]. Perhaps exhibiting the most utility, ultrasound-induced changes in the cell membrane permeability have been strongly correlated with cavitation activity, which leads to formation of reversible pits in the cell membranes allowing for delivery of genes, drugs, and macromolecules into the cells or release of the cell components, such as calcium and insulin [40]. Because of the positive effects of therapeutic ultrasound, this modality has been proposed for and used in numerous clinical applications including bone healing, cartilage repair, pain management, essential tremor treatment, drug delivery, carpel tunnel syndrome treatment, and tumor ablation [41], [42], [43].

Acoustic cavitation, the most widely studied nonthermal mechanism, involves the interaction of a sound field with a gas bubble and requires a stabilized gas body or nucleus to occur [44]. When exposed to an acoustic field, a bubble in liquid will oscillate around a radius—the maximum response by the bubble to the acoustic field occurs at the resonance frequency, which is dependent on the initial size of the bubble. An example of this oscillation is shown in *Figure 6,* where the predicted response of a microbubble in water exposed to 2.5 MHz ultrasound with an amplitude of 0.4 MPa is plotted. Here, we are interested in the effects of noninertial cavitation, which describes a repetitive oscillation of a bubble over many acoustic cycles [45], [46]. Due to noninertial cavitation, things such as acoustically-driven bubble oscillation causing heat production can occur, or a microstreaming of fluid near the bubble as well as localized shear stresses. Additionally, interactions between bubbles and particles in a sound field can result in the attraction of nearby particles or cells to an oscillating bubble [46].

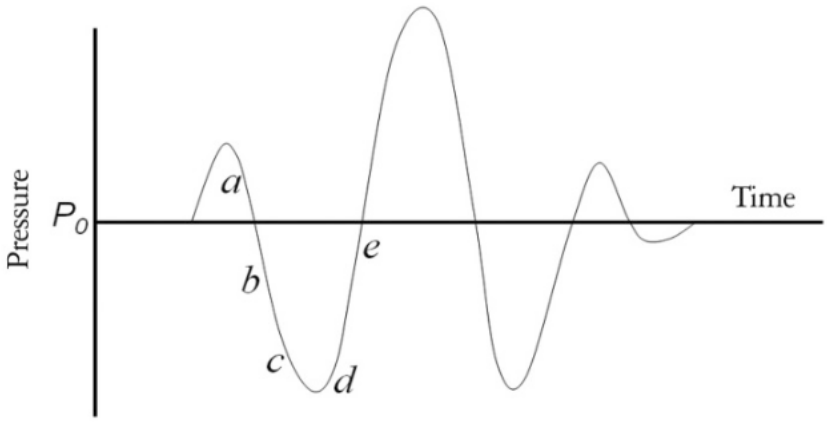

Figure 6: Acoustic Cavitation: Oscillation of a Microbubble When Exposed to Ultrasound Frequency of 2.5 MHz; This repetitive oscillation shown relates to noninertial cavitation [47].

Previous studies have thoroughly established that ultrasound can produce a variety of biological effects both *in vivo* and *in vitro*, and the acoustic mechanisms responsible for

some of these bioeffects are well-known [48], [49]. For instance, cavitation can occur *in vivo* if suitable microbubbles are present, such as in the intestine or in tissues containing microbubble contrast agents. But, the environment for some acoustic mechanisms, such as heating, cavitation, and acoustic streaming, are much different *in vitro* than in *in vivo* models, which is a critical difference to understand when considering strategies for employment of therapeutic ultrasound.

An emerging area of therapeutic ultrasound that is gaining traction in the field is the use of this technology to regulate gene expression. For instance, it has been previously shown that thermal bioswitches triggered by ultrasound can be utilized as a mechanism for sonogenetic control [50], [51], [52]. Furthermore, ultrasound can be used to influence gene expression through oxidative stress or the production of reactive oxygen species (ROS). More specifically, ultrasound has been shown to activate custom made promoters via generation of ROS [53], [54]. One approach with perhaps the most significant application of therapeutic ultrasound to gene regulation involves bone healing therapies to induce upregulation of the COX-2 gene [55]. This gene is activated during the process of mechanically induced bone formation. This example is one of the only instances of ultrasound mediated gene expression of an endogenous gene, as other studies have devised a transgenic model to show the effectiveness of ultrasound-mediated gene expression. The results of this study provide promising new insights to the potential use of ultrasound to induce gene regulation in both *in vivo* and *ex vivo* models.

1.4 Perfusion

Perfusion, a vital technique in the realm of cell biology, is a precise and controlled process that involves the continuous delivery of a fluid, typically a specialized medium or

solution, to specific cells or tissues [56]. This method facilitates the creation of a stable microenvironment around the cells, thereby enabling in-depth investigations into the cellular responses evoked by a diverse array of external stimuli. These systems, integral to both *in vitro* and *in vivo* experimental setups, are meticulously engineered to ensure an uninterrupted and regulated flow of targeted mediums, ranging from nutrient-rich solutions to pharmacological agents, directed towards a cellular suspension [57]. These systems are customarily equipped with various components, including advanced pumps, precisely calibrated tubing, and specialized chambers, thereby conferring the user with precise control over crucial parameters such as flow rate, temperature, and the composition of the perfusion medium. A simple schematic of a type perfusion system can be seen in *Figure 7*. The perpetual flow, characteristic of these systems, mirrors the physiological conditions, effectively avoiding any potential artifacts arising from stagnant environments [58].

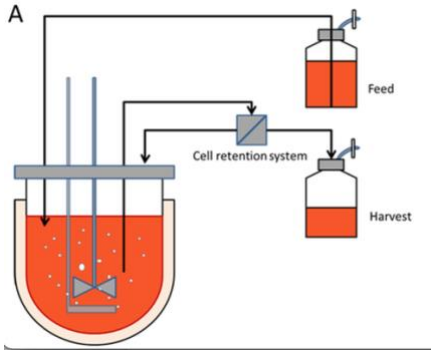

Figure 7: Perfusion; Schematic illustrating perfusion system with chamber, tubing, pump, and media reservoir [59].

The utility of these types of systems is that it allows researchers to precisely control the biochemical and physical parameters surrounding the cells, thereby creating an environment that closely resembles the *in vivo* conditions. With continuous flow, researchers can continuously monitor the cellular response to a stimulus over a prolonged period, enabling them to capture dynamic changes and long-term effects [60]. Perfusion

systems help eliminate concentration gradients that can occur in static cell cultures, ensuring uniform exposure of cells to the stimulus and minimizing the risk of biased experimental results. Further, perfusion systems provide advantages over static systems seen when considering negative feedback loop mechanisms of hormone release. For example, in a static system, cells will trigger feedback regulation to stop releasing contents into the stagnant environment, complicating interpretation of experimental results. With a perfusion setup, the medium is constantly refreshed and negative feedback mechanisms are minimized, allowing for a clearer assessment of the direct effects on stimuli in the cellular microenvironment. By mimicking the flow of nutrients, hormones, or other biochemical signals in the body, perfusion systems can better replicate the physiological conditions experienced by cells *in vivo* [61].

Perfusion is often used in cell biology to measure cellular responses to a given stimulus because it provides a more accurate representation of how cells behave in their natural environment [62]. By controlling the delivery of specific substances or factors to the cells, researchers can assess how cells react to changes in their environment, such as alterations in nutrient availability, exposure to specific drugs, introduction of different cellular treatments, or variations in oxygen levels. This technique is particularly valuable in studying cellular processes such as signaling cascades, receptor-ligand interactions, and metabolic pathways, allowing for a better understanding of the mechanisms underlying cellular responses to different stimuli [63]. This strategy plays a critical role in enabling researchers to study cellular responses under controlled conditions that closely resemble physiological environments. By maintaining a continuous flow of specific solutions or substances to the cells, perfusion systems provide valuable insights into the dynamic

behavior of cells and their responses to various stimuli, contributing to advancements in fields such as drug development, tissue engineering, and understanding fundamental biological processes.

1.5 Previous Relevant Work

Over the course of recent years, experimentation with therapeutic ultrasound to yield hormonal effects in the pancreas have become increasingly explored. One such study by Yoon et al. explored the effects of ultrasound-mediated calcium (Ca^{2+}) oscillations in a HIT-T15 pancreatic β-cell line [64]. Insulin secretion has been previously shown to be stimulated by many different hormones as well as neurotransmitters like glucose-like-peptide-1 (GLP1) and carbon monoxide (CO), but the major secretagogue of this hormone is glucose [65]. When blood glucose levels rise in the body, the metabolism of pancreatic β-cells is increased, elevating the ATP/ADP ratio, which closes ATP-sensitive potassium (K^+) channels, depolarizing the membrane. This in turn opens voltage-dependent Ca^{2+} channels, causing an influx of calcium into the extracellular space—elevating free cytosolic calcium and triggering the release of insulin. Yoon et al. [64] set out to investigate these mechanisms of insulin secretion, especially focusing on glucose-stimulated insulin secretion (GSIS) and the role that both ATP and Ca^{2+} play in this phenomenon. To do so, a 45 MHz ultrasound transducer with a pulse repetition frequency of 1 kHz and duty cycle of 2% was used as to deliver low-intensity pulsed ultrasound. Overall, the results of this study indicated that low-intensity pulsed ultrasound could indeed activate these calcium responses from the HIT-T15 pancreatic β-cells and these distinctive oscillatory Ca^{2+} patterns were triggered by the release of ATP as a signaling mediator.

An article written in 2004 by Dalecki highlights the extensive use and multifaceted applications of ultrasound in the field of medicine [66]. Low-intensity, PUS has been demonstrated clinically to accelerate the rate of fracture healing; however, the acoustic mechanism for this interaction of ultrasound and bone is still yet unknown. Similarly to PUS, high-intensity, focused ultrasound (HIFU) has promising applications for the nonsurgical treatment of tumors and for noninvasive hemostasis, employing intensities higher than 1,000 W/cm^2 to elicit a response. An important aspect to consider when designing new therapeutic strategies with ultrasound are the intricate acoustic mechanisms by which these frequencies interact with tissue. These interactions can occur through both thermal or nonthermal physical mechanisms. For example, absorption of ultrasound by the tissue can result in the conversion of ultrasonic energy to heat. Ultrasound-induced temperature increases depend on tissue properties, such as absorption coefficient, density, or perfusion, as well as ultrasound parameters used (i.e., frequency, amplitude, pulse duration, pulse repetition frequency (PRF), etc.), allowing for generation of heat in tissues to be easily controlled.

The current body of evidence shows that ultrasound may be responsible for the production of reactive oxygen species (ROS) which can contribute to cell apoptosis, and that in an *in vitro* cardiac model, ultrasound administered at 1-3.6 MHz increased intracellular oxidative stress [67]. Further, the increased ROS production after ultrasound was confirmed with analysis of the morphology of the tissue, showing significant endothelial damage after 30 s, and increased DNA scattering after 15 s. Additionally, ultrasound has been shown to influence cellular regeneration. In a study by Tarantal et al., repeated ultrasound exposure reduced both leucocyte production and the number of somites

present in an embryonic culture of monkey uteri with exposure over a period of 15 min at 40 °C [68].

Another interesting effect of ultrasound that has been researched extensively recently, is its effect on the modulation of gene expression. A study done Szablowski et al., investigated acoustically targeted chemogenetics (ATAC) for the control of neural circuits through the use of focused ultrasound (FUS) [69]. The motivation for this study was to propose an alternative approach to pharmacological treatments that are currently employed for the treatment of neurological and psychiatric disease that delivered spatial, cell-type and temporal control through neuromodulation, without the need for surgery. To do so, the researchers combined three recently developed technologies: focused ultrasound blood–brain barrier opening (FUS-BBBO) for spatial targeting, adenoassociated virus (AAV) vectors for delivery of genes to specific cell types, and engineered chemo-genetic receptors for modulation of targeted neurons using orally bioavailable compounds. In particular, designer receptors exclusively activated by designer drugs (DREADDs) were used as these proteins are modified versions of natural activatory or inhibitory G-protein-coupled receptors, engineered to respond to synthetic molecules rather than endogenous ligands. DREADDs are becoming widely used in clinical settings since they have shown a strong ability to selectively control neural circuits. To evaluate the ability of ATAC to target the expression of DREADDs to a specific location in the brain, the researchers first performed FUS-BBBO on the hippocampus of wild-type mice, hoping to find a change in expression of hM4Di, a well-known inhibitory of neuronal activity in the brain. The FUS was applied with a 1.5 MHz transducer, guided by MRI, and after allowing for 6-8 weeks for transgene expression, the targeted locations showed a significant increase in hM4Di expression,

while mice who did not receive ultrasound treatment showed no change in expression. This finding confirmed that ultrasound-stimulated BBBO was required for gene delivery, indicating that FUS could have potential effects on modulation of expression within neural circuits.

One study that we expect gain similar results to was a study done by Razavi et al., where the effects of pFUS on the pancreas were investigated [70]. pFUS was applied to a rodent pancreas model at 1.1 MHz with a 5 Hz pulse repetition frequency, first at a low-intensity of 11.5 W/cm^2, then at a high-intensity of 18.5 W/cm^2. After treatment, molecular analysis was done to determine the effects of pFUS on cytokine expression in both a low-intensity and high-intensity condition. 24 hr post-treatment in the low-intensity condition exhibited significant downregulation of many different cytokines, including granulocyte-macrophage colony-stimulating factor (GM-CSF), many different interleukins (e.g., IL-13, IL-15, IL-2, etc.), and tumor-necrosis factor α (TNF-α). When pFUS was increased to the high-intensity condition, significant increases in the expression of these components were observed. This study illustrated the potential of pFUS to induce changes in expression and regulation of different genetic factors in the microenvironment of the pancreas, demonstrating that at higher intensities than used in this study, therapeutic ultrasound could indeed cause an effect. Another study done by this same group demonstrated the efficacy of therapeutic ultrasound for use in islet cells explored the idea of experimenting with pulsed focused ultrasound (pFUS) to enhance the function of pancreatic islets [71]. This study mainly focused on applications to type 1 diabetes, however the researchers were able to present interesting findings that support our hypothesis that low-intensity ultrasound can induce an insulin response in human islets. For example, it was found that an intensity of

0.71 W/cm^2, insulin secretion was increased with a subsequent increase in intracellular calcium [71]. In both a low-glucose and high-glucose condition, following pFUS application, a significant increase in insulin production was shown of 1.44 $\pm$ 0.09 ng/mL.

Furthermore, past studies from our lab have illustrated the use of low-intensity ultrasound on insulin secretion and calcium channel activation, pointing to its potential for therapeutic applications for the pathogenesis of diabetes [72]. Insulin is naturally secreted from pancreatic β-cells in a calcium-dependent manner, where calcium influx is the last triggering step before exocytosis of insulin containing vesicles in glucose-stimulated insulin secretion. Previously, we have shown that therapeutic ultrasound can induce a release of insulin from rat pancreatic insulinoma β-cells and that the presence of calcium ions is necessary for this release [72], [73]. These results are shown in *Figure 8*.

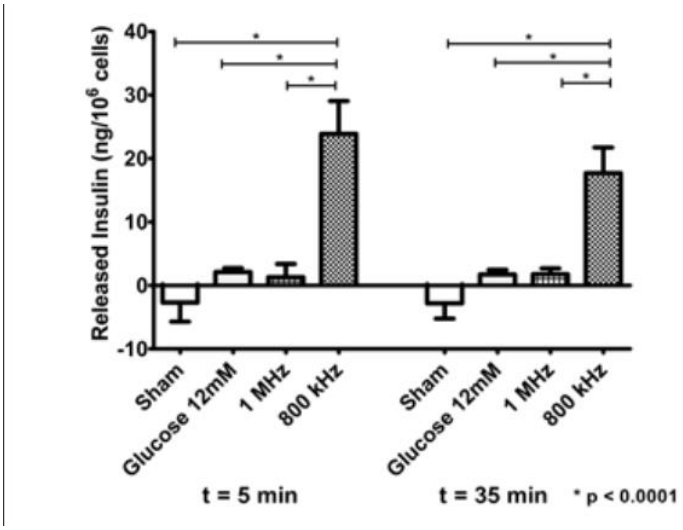

Figure 8: *In Vivo* Insulin Release; Compared to SHAM treatments, high glucose, ultrasound of 1 MHz and 800 kHz frequency all caused a significant release in insulin, with the greatest increase in insulin concentration shown at 800 kHz [72].

Our past studies made use of carbon fiber amperometry to detect secretion from INS β-cells in real time. The levels of released insulin were also measured in response to ultrasound treatment using insulin-specific ELISA kits. β-cells were exposed to continuous

wave 800 kHz ultrasound at intensities of 0.1, 0.5 and 1 W/cm^2 for several seconds [73]. Carbon fiber amperometry experiments showed that application of 800 kHz ultrasound at intensities of 0.5 and 1 W/cm^2 was capable of stimulating secretory events. *Figure 9* shows the measured levels of released insulin from β-cells exposed to 800 kHz ultrasound at intensity of 0.5 W/cm^2 for durations of 15 s and 5 min compared to levels from sham-treated cells. No released insulin was detected in sham-treated groups. Cells treated with 800 kHz continuous ultrasound at intensity of 0.5 W/cm^2 for duration of 15 s released approximately 16.8 ng/mL of insulin, while cells exposed to 5 min using the same parameters released approximately 34.6 ng/mL of insulin. Both 15 s and 5 min ultrasound exposure stimulated significant insulin release from β-cells as compared to sham-treated cells.

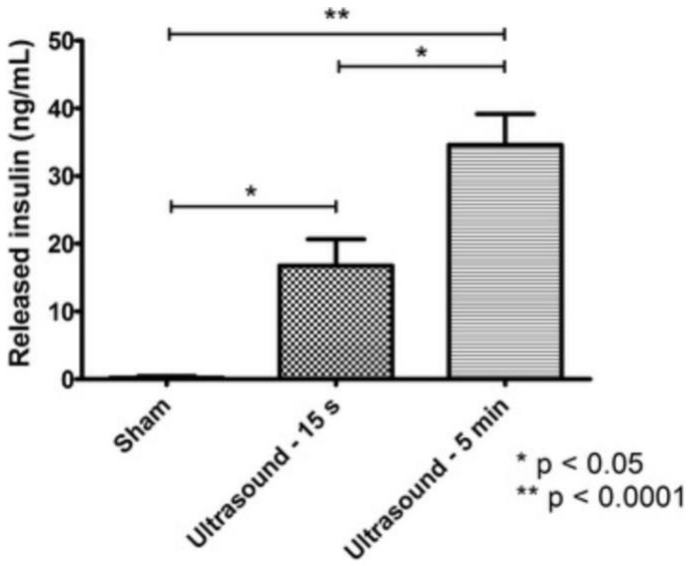

Figure 9: Insulin Levels in β-cells Exposed to 800 kHz Ultrasound; Insulin release was significant when ultrasound was administered for both 15 s and 5 min, with the greatest increase shown at 5 min exposure [73].

An important study by Svendsen et al. was done that assessed whether insulin secretion depended on intra-islet glucagon signaling [74]. In this study, the researchers

made use of a perfused mouse pancreas to investigate the mechanisms that regulate intra-islet communication, mainly looking at paracrine relationships within islets. Local glucagon signaling was disrupted using different genetic or pharmacological approaches while glucagon secretion was acutely eliminated from alpha cells using diphtheria toxin (DT)-induced destruction of pro-glucagon-producing alpha cells. Interestingly, with the perfused mouse pancreas the researchers observed that glucagon was only able to stimulate insulin secretion at elevated glucose (12 mM) levels whereas no response was observed at 3.5 mM glucose. Furthermore, infusions of glucagon (0.1-10 nM) stimulated insulin secretion in a dose-dependent manner with 2.0-3.7 fold increases and it was found that in all control mice, switching from low (3.5 mM) to high (12 mM) glucose led to an 4.5-fold increase in insulin ($p < 0.05$) and a simultaneous drop in glucagon secretion (3-fold, $p < 0.05$). Further visualization of these conclusions can be seen in *Figure 10*. These findings are important to our study as it establishes a baseline of the concentration of glucose that will be needed to cause a response in insulin secretion in our model.

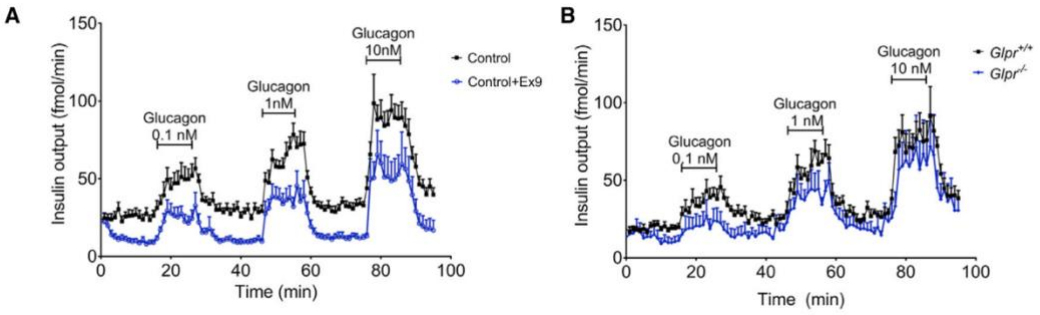

Figure 10: Insulin Output in Control and Perfused Wild-type, GLP-1 Receptor Knockout Mice Pancreas; It was shown that at higher concentrations of glucose infusion, perfused pancreases released a significant amount of insulin, illustrating a dose-dependent relationship [74].

A further study, completed by Suarez-Castellanos et. al, explored the potential of using therapeutic ultrasound (TUS) to stimulate and regulate the activity of pancreatic

endocrine cells, specifically insulin-producing β-cells [75]. Previous studies have shown that US energy can stimulate insulin release from pancreatic β-cells *in vitro* and increase blood insulin levels in mice without adverse effects. However, this study aimed to reproduce these results using human pancreatic islets and investigate the effects of TUS on alpha cells that produce glucagon and acinar cells that secrete digestive enzymes. The researchers conducted experiments using *ex vivo* human pancreatic islets and rabbit pancreases. They applied TUS treatment at a frequency of 800 kHz with an intensity of 0.5-1 W/cm^2 for 5 minutes and collected extracellular fluid samples to measure insulin, glucagon, and alpha-amylase release at the start of treatment (t = 0 min), immediately after TUS treatment (t = 5 min) and 30 min after treatment ended. Quantification of insulin, glucagon, and alpha-amylase levels was done using an ELISA Kit specific to each hormone. These hormones were chosen, as they are all crucial for the proper functioning of the exocrine pancreas in maintaining blood glucose levels and aiding in the digestion of carbohydrates [76]. Their coordinated action ensures that the body can efficiently utilize nutrients from the diet for energy and other essential metabolic processes. The results showed that TUS treatment increased insulin release immediately after treatment, but the effect diminished after 30 minutes. Glucagon release appeared to increase briefly after treatment, but no significant difference was observed compared to the control group. Alpha-amylase release did not show significant changes due to TUS treatment. Results of the hormone secretion after TUS treatment can be seen in *Figure 10.* The study suggests that TUS has the potential to stimulate insulin release without harming pancreatic tissue. However, further research is needed to understand the spatial and temporal characteristics of TUS-stimulated hormone secretion and its impact on glycemic control.

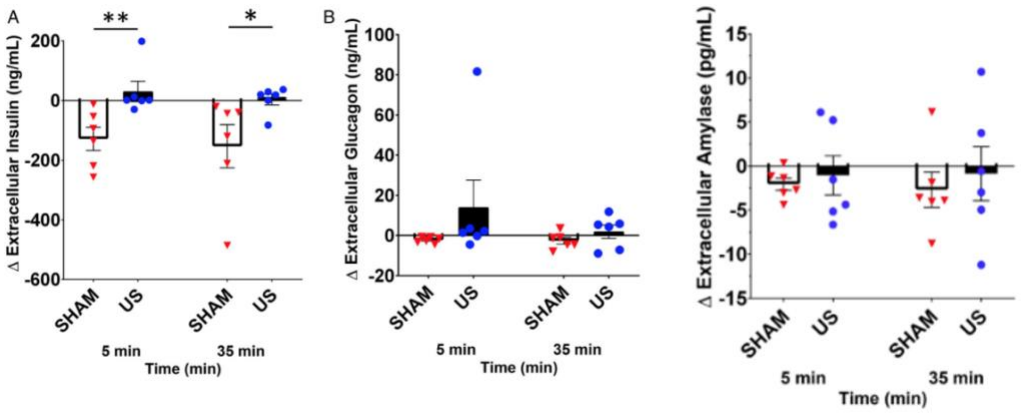

Figure 11: Results of Hormone Secretion Measured with an ELISA Kit after TUS Treatment; It was shown that with the ultrasound parameters used in this study, a significant increase in insulin content was observed, whereas no significant changes were shown with glucagon or amylase [75].

1.6 Significance of Work

The potential of therapeutic ultrasound to elicit hormone secretion in both an animal and human model is relatively unexplored, with much of the research focusing more on neural pathways and how ultrasound application can induce responses in the brain [77]. For example, it has been shown that pFUS can be used to stimulate targeted neurons, and the utilization of specific pulse parameters has the possibility of triggering the activation and propagation of neural signals to stimulate specific areas of the brain [79]. Considering this, the method described aims to harness the power of unfocused ultrasound energy to enhance insulin release from pancreatic β-cells. More than just a novel therapy, this strategy holds the promise of unveiling the intricate mechanism underlying the impact of ultrasound stimulation on diverse cells and tissues. We believe that low-intensity, unfocused ultrasound could elicit a desired response, as the outcomes of this type of therapy on sensory and motor areas in the brain are well-established [78]. More specifically, the

effects of low-intensity transcranial stimulation were shown to have an excitatory effect in a rat model [79].

This dissertation strives to identify the workings behind the therapeutic effects of ultrasound on gene regulation and hormone secretion within mammalian pancreatic cells, as well as an *ex vivo* minced pancreas slice rodent model. By focusing on the manipulation of hormone encoding gene promoters, we aim to optimize secretory functions, thus paving the way for a more comprehensive understanding of ultrasound's therapeutic potential. Utilizing the human pancreatic islet model, we seek to thoroughly explore the clinical application of TUS, and its broader implications for other endocrine and exocrine tissues. From this, we hope to highlight a crucial opportunity to investigate the applicability of ultrasound in other metabolic disorders beyond diabetes. This research is important due to its innovative use of ultrasound control in the investigation of potential therapies for endocrine disease, particularly type 2 diabetes mellitus. Successful outcomes hold the capability to open up an entirely new domain in TUS research—for instance, the exploration of low-intensity TUS for the enhancement of other hormone secretions, such as thyroid or adrenal hormones, could have far-reaching implications for addressing various metabolic disorders.

It is believed that this research may lead to the first non-pharmacological approach for treatment of type 2 diabetes through augmentation of insulin release and provide new mechanistic insights on how ultrasound stimulation may affect different tissues in the body. In turn, this could pave the way for elimination of invasive treatments, as well as non-optimized therapeutic plans for patients who suffer from type 2 diabetes mellitus leading to negative outcomes.

The research presented in this study marks a significant milestone in understanding the mechanisms governing hormonal regulation within the pancreas. Conventionally, investigations into the effects of ultrasound have predominantly focused on targeted approaches, particularly within neurological contexts. However, our work breaks new ground by demonstrating the potential of unfocused, continuous ultrasound application in modulating protein release dynamics within the pancreas. This departure from traditional methodologies underscores the novelty of our approach. Through meticulous experimentation employing both a rat insulinoma β-cell line and a minced rat pancreas model, we have unveiled compelling evidence of ultrasound's impact on protein expression, particularly in relation to insulin and glucagon secretion. Notably, our findings elucidate the ability of low-intensity therapeutic ultrasound to evoke a significant increase in insulin release from both cellular and organotypic pancreatic models, while concurrently suppressing glucagon secretion. This dual effect on key pancreatic hormones underscores the versatility and promise of ultrasound as a potential noninvasive therapeutic modality for diabetes management. The implications of our discoveries are profound, offering novel insights into the development of targeted treatment strategies for patients with diabetes, thereby addressing a critical unmet need in clinical practice.

Chapter 2: Optimizing Methods for Ultrasound Administration and Gene Expression Analysis

2.1 Rationale

Before completing the gene expression studies using the donor human pancreatic islet cells, it was necessary to optimize the protocol and further learn both how to effectively culture primary cell lines and execute the RT-qPCR. This was done using INS 832/13 rat insulinoma cells. These cells were chosen for the following studies, as they have been shown to harbor insulin secretion over extended passages and have enhanced secretory responsiveness to glucose, pointing to its usefulness to examine insulin secretion regulation and pancreatic islet β-cell function. It is important to note that the data shown in Chapter 2 was not done in duplicate, so accurate quantification cycle (Cq) averages and fold change (FC) values are unable to be shown; however, practice calculations are summarized. Through trial and error, it was determined that, once we moved to experimentation with donor human pancreatic islet cells, samples would be plated for RT-qPCR in duplicate, thus allowing for accurate averages to be taken, which was ultimately necessary to discern an accurate FC value for each gene after ultrasound administration.

2.2 Methods

2.2.1 Cell Culture

INS 832/13 rat insulinoma cells were thawed using a common protocol from our lab. This involves placing a frozen vial of cells previously stored in a -80 C freezer in a water bath at 37 °C and swirling the tube around for 1-2 minutes until the cell suspension is completely thawed. The suspension is then transferred to a 15 mL centrifuge tube and

INS media is added to the suspension to match the balance for the countertop centrifuge. Cells are then centrifuged at 22 °C, 800 rpm for 10 min, followed by gentle aspiration of media as to not disturb the pellet. 4 mL of new INS media is then added to the tube and the solution is resuspended to break the pellet up. All cell suspension is then transferred to a sterile 50 mL cell culture flask and placed in a CO_2 incubator at 37 °C.

Once INS cells have reach ~70% confluency, they will be passaged and plated on to the 24-well culture plate used for RT-qPCR. The old media will be taken out of the cell culture flask and the cells will be washed with 1 mL of 1x phosphate buffered saline (PBS) at pH = 7.2. 1 mL of trypsin-EDTA is then added to the flask and it is placed into the CO_2 incubator for 2 min to ensure that cells are broken up. 5 mL of fresh media is then added to the flask containing the cells and trypsin and the flask is rinsed a few times before the contents are placed in a 15 mL centrifuge tube. After centrifugation, the media is aspirated out and replaced with 4 mL of new media and the cells are then ready for plating.

2.2.2 INS Cell Plating

For the INS cell plating, a 1:6 dilution of cell suspension to media was used. After the 4 mL of new INS media was placed into the 15 mL centrifuge tube containing the cell pellet, 1 mL of cell suspension was transferred to a new 15 mL centrifuge tube containing 6 mL of INS cell media. This tube was then sealed and inverted a few times to ensure a homogenous mixture. 500 µL of the dilution of cells was then dispensed into 5 wells of the 24-well culture plate (Control, Thapsigargin (Tg), Tunica-Mycin (Tn), High Glucose (Hg), Ultrasound (US) and placed into the CO_2 incubator, allowing for at least a 24 h incubation time before treatments.

2.2.3 Cell Treatments

After at least 24 h of incubation, the INS cells were treated with 100 μM Tg, 100 μM Tn, and 1 mM of Hg. The volume of each compound added to the INS cells was determined using the equation below, where C_1 is the concentration of the stock solution, V_1 is the volume of the cell suspension, C_2 is the desired concentration after dilution, and V_2 is the final volume needed of the stock solution to meet the necessary dilution requirements.

$$C_1V_1 = C_2V_2$$

2.5 μL of Tg was added to one well containing 500 μL of cell suspension, 2.5 μL of Tn was added to one well containing 500 μL of cell suspension and 7.5 μL of Hg was added to the third treatment well.

2.2.4 Ultrasound Administration

Ultrasound treatments were applied to the pre-defined wells 2 hours before the end point for the Tg treated, Tn treated, and Hg treated wells. A Research amplifier (Souderton, PA), connected to an Agilent waveform generator (Santa Clara, CA) was used to administer the input voltage. To channel the input voltage, an impedance matching network was attached to the power supply and the corresponding ultrasound transducer. The ultrasound transducer was oriented beneath the 24-well plate in a water bath held at 37ºC, 2.5 cm below the surface. The 2.5 cm distance below the refers to the distance from the far field (dff), as mentioned in Chapter 1. The ultrasound setup can be seen in *Figure 12*. Ultrasound was applied to the INS samples continuously for 5 minutes, with a frequency of 800 kHz at an intensity of 0.5 W/cm^2.

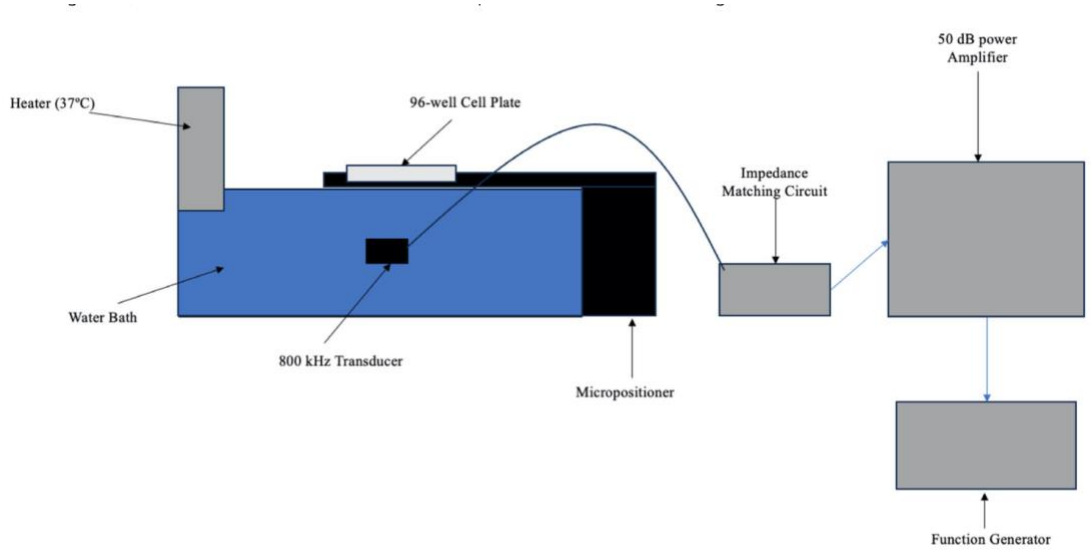

Figure 12: Experimental Set-Up for Ultrasound Administration; 24-well culture plate was positioned above a water bath at 37°C, with the ultrasound transducer oriented in the water bath 2.5 cm below the surface of the plate. Ultrasound was applied for 5 min continuously, at a frequency of 800 kHz and intensity of 0.5 W/cm^2.

2.2.5 RNA Extraction and Quantification

To accomplish RNA extraction and purification, a Direct-zol RNA Miniprep kit (Zymo Research, Irvine, CA) was used [80]. Initially, the cell suspension was aspirated from each well and substituted with 350 µL of TRI Reagent, subsequently transferred to a centrifuge tube, and centrifuged at > 10,000 RPM for 30 s using a Microfuge 18 Centrifuge (Beckman Coulter, Brea, CA). Post-centrifugation, 350 µL of 95-100% ethanol was added to the TRI reagent-containing tube and thoroughly mixed. The resulting mixture was then transferred to a Zymo-Spin IICR Column Collection Tube and centrifuged under the same conditions. The flow-through was discarded, and the column was subjected to 400 µL of Direct-zol RNA PreWash buffer followed by centrifugation, with this process being repeated. Following this, 700 µL of RNA Wash Buffer was added, and the sample was centrifuged for 1 min to ensure complete removal of the wash buffer. The column was then moved to an RNase-free tube, and 50 µL of DNase/RNase-Free Water was added directly to the column matrix, with a final centrifugation of 30 s.

To quantify RNA, a NanoDrop One machine (ThermoFisher Scientific, Waltham, MA) was used. The machine was first blanked using 2µL of RNase free water dispensed onto the reader. After blanking, the surface was cleaned with distilled water. 2µL of each sample was dispensed onto the reader and concentration (ng/µL) and purity (260/280) were measured. The working concentration used was $\geq$ 15 µL and an acceptable purity was deemed as 1.9-2.1.

2.2.6 cDNA Synthesis

cDNA was synthesized using a pre-defined protocol that corresponded with the applied biosystems high capacity cDNA reverse transcription kit from ThermoFisher Scientific (Waltham, MA) [81]. The cDNA reaction required 10 µL of RNA + water and 10 µL of a prepared master mix. To determine the amount of RNA to be added, the lowest concentration of RNA yielded from the extraction process was used. A sample calculation can be seen below:

$$\frac{10\ \mu L | 21.9\ ng}{1\ \mu L} = 219\ ng$$

The concentration of 219 ng was then used to calculate the corresponding µL of RNA to be added with water for each treatment group. The 10 µL of RNA was then added to a cDNA-sized vial and placed on ice, while the cDNA master mix was prepared.

The cDNA master mix contained a mixture of Buffer 10X, random primers, dNTP mix, reverse transcriptase and H_2O. The specific amounts of each component of this mixture are 2 µL of buffer 10X, 2 µL of random primers 10X, 0.8 µL of deoxynucleoside triphosphate (dNTP), 1 µL of reverse transcriptase (RT), and 4.2 µL of H_2O, for a total volume of 10 µL. A negative control sample was created by removing the reverse

transcriptase from the mixture and replacing it with an equal volume of water. This was done to ensure that all genomic DNA was washed out from the RNA extraction.

Once the master mix was finished, 10 µL was added into the cDNA-sized vials containing the RNA. The vials were then centrifuged using a StripSpin 12 centrifuge (Benchmark, Tempe, AZ). Immediately after centrifugation, the vials were placed in a C1000 Touch Thermal Cycler (Bio-Rad, Hercules, CA), using the cDNA-mRNA protocol. This protocol included four steps; the first step involved increasing the temperature to 25ºC for 10 min, followed by the next step of heating to 37ºC for 1 hr. The third step then increased the temperature to 85ºC for 10 min, with a final step infinitely holding the reaction at 4ºC. Once the protocol was finished, the samples were placed into a freezer at -20 ºC overnight or until qPCR could be completed.

2.2.7 RT-qPCR

The tested genes were insulin, amylin, BiP and glucagon. Actin was used as a housekeeping gene to normalize the quantification cycle (Cq) values output by the PCR reaction.

Before qPCR, it was required to dilute the cDNA samples. This was done in a 1:3 dilution; 10 µL of cDNA was added to 30 µL of RNase/DNase Free Water for each of the treatment groups. Following the dilution, these samples were placed on ice, while the primer dilutions and master mix was prepared. Specific information regarding each primer sequence can be found in *Table 1*.

Table 1: Primer Sequences for Tested Genes; Primer sequences were derived from rat primers for the housekeeping gene, actin, and the tested genes, insulin, glucagon, amylin, and BiP.

Gene	Forward Sequence	Reverse Sequence
Actin	GCTACAGCTTCACCACCACA	ATCGTACTCCTGCTTGCTGA
Insulin	TGGCTTCTTCTAACACACCCAAG	ACAATGCCACGCTTCTGCC
Glucagon	CCATTCACAGCCCACATTCA	TTTCACCAGCCAAGCAATGA
Amylin	CCACTTGAGAGCTACACCTG	GAAGTTTGCCAGACGTTGTG
BiP	TGGACACTTGGCCTTTTGCG	CTGTGGACCAGTCAGTCGC

The master mix was prepared using SYBR Green supermix (Bio-Rad, Hercules, CA), the primer dilutions, and RNase/DNase Free Water. The necessary components and volumes for this mix can be found in *Table 2*. On the PCR plate, 18 µL of master mix was added to each well and 2 µL of cDNA was added to the wells. A set-up of the PCR plate can be found in *Figure 13*.

Table 2: PCR Master Mix; Components of the PCR master mix were combined based on calculations of the number of samples + 2 to create enough mix to dispense into each well for the PCR reaction.

Component	Volume (µL)	Final Concentration
iTaq SYBR Green Supermix	10 µL	1X
Forward and Reverse Primers	1 µL from each 5 µM stock	300-500 nM for each primer
H_2O	6 µL	100 ng-100 fg
Total	18 µL	

CtA rINS	CtB rINS	TgA rINS	TgB rINS	TnA rINS	TnB rINS	HgA rINS	HgB rINS	UsA rINS	UsB rINS
CtA rAMY	CtB rAMY	TgA rAMY	TgB rAMY	TnA rAMY	TnB rAMY	HgA rAMY	HgB rAMY	UsA rAMY	UsB rAMY
CtA rACT	CtB rACT	TgA rACT	TgB rACT	TnA rACT	TnB rACT	HgA rACT	HgB rACT	UsA rACT	UsB rACT
CtA rGLU	CtB rGLU	TgA rGLU	TgB rGLU	TnA rGLU	TnB rGLU	HgA rGLU	HgB rGLU	UsA rGLU	UsB rGLU

Figure 13: PCR Plate for INS Cell Gene Expression Analysis; Samples were plated in each well for each treatment and corresponding gene. “A” corresponds to suspension from 1 dish, whereas “B” are samples that came from a different dish.

After each master mix and cDNA sample was added to their corresponding well, the plate was centrifuged for 2 minutes at 22 ºC and 200 rcf. After centrifugation, the plate was placed in C1000 Touch Thermal Cycler with a pre-defined protocol. The PCR protocol includes six steps; the first step involves heating to 95ºC for 2 min and the second step comprises an additional 5 min at 95 ºC. Following these two steps, the thermal cycler decreases temperature to 60ºC for 30 min, followed by a plate read. Step four returns the reaction to step two and repeats this action 40 times. At step five, a melt curve is created from 65ºC -95ºC, with increasing temperature in increments of 5ºC for 5 min, followed by another plate read. Finally, the last step holds the reaction at 95ºC for 30 min.

Upon completion of the PCR reaction, Cq values were output for each gene. The gene expression analysis data from RT-qPCR is expressed as fold change, where the ratio of a change in fold after treatment is compared to a control. A fold change of greater than 1 signifies an upregulation in gene expression, while a fold change of less than 1

corresponds to a downregulation of genetic expression. To calculate the fold change, the delta-delta Cq method was utilized. The equation for this method is seen below:

$$\Delta Cq = 2\text{^}(Actin_{Cq} - Gene_{Cq})$$

From the equation, ΔCq was calculated for each of the tested genes. From this value, fold change was determined by dividing the ΔCq of each gene treatment group by the control ΔCq. Fold change values were reported as the perceived change in gene expression.

2.3 Results

For the thapsigargin-treated INS cells, the fold change values were all shown to less than 1, except for BiP, with a reported fold change of 1.16. Likewise, the tunica-mycin, high-glucose, and ultrasound-treated INS cell fold change values were all found to be less than 1, except for the tunica-mycin-treated BiP cells. A summary of the data can be found in *Table 3*.

Table 3: Summary of Fold Change Values for Optimization with INS cells; A fold change of greater than 1 indicates an upregulation in expression and a fold change of less than 1 reflects a downregulation.

	Insulin	**Amylin**	**Glucagon**	**BiP**
Control	1.00	1.00	1.00	1.00
Thapsigargin	0.53	0.57	0.93	1.62
Tunica-Mycin	0.35	0.39	0.20	2.15
High-Glucose	0.16	0.16	0.12	0.24
Ultrasound	0.40	0.32	0.29	0.49

Due to samples not being plated in duplicate and being taken from separate wells on the plate, statistical analysis was unable to be done to draw any conclusions of the relationships between the fold change of treated groups and control groups. Therefore, no

conclusions were drawn from these experiments; however, important lessons were learned and information gained that informed our protocol for the following studies described.

Chapter 3: Analysis of Gene Expression of Donor Human Pancreatic Islet Cells

3.1 Methods

3.1.1 Donor Pancreatic Islet Cell Acquisition

Nine different donor samples of human pancreatic islet cells were received from Prodo Laboratories, Inc. (Aliso Viejo, CA) to analyze the effects of ultrasound on gene expression of insulin and glucagon. No diabetic human islets were available for purchase. Each sample was obtained from a non-diabetic pancreas with normal lab results and a purity ranging from 90-95%, with a viability of 95%. Six male donor samples and three female donor samples were used for the study. The average age of the donors was 51.0 years old (range: 33-67 y/o) while the average BMI was 29.0 (range 21.6-34.7) and Hb1AC was 5.28%. Of the nine samples, six came from Caucasian donors, one came from a Hispanic donor, one came from an Asian donor, and one came from an African American donor.

For amylin and BiP, the same donors were used as in insulin/glucagon donors 1-4, but a different donor sample was used for group 5. This was done as data could not be to be obtained when testing amylin and BiP with donor 5 of insulin and glucagon. Donor groups 6-8 were the same as the insulin and glucagon group 7-9. Each sample was obtained from a non-diabetic pancreas with normal lab results and a purity ranging from 90-95%, with a viability of 95%. The samples comprised of 5 males, 4 of which were Caucasian and

1 Hispanic. The average age of the donors was 55.0 years old while the average BMI was 28.5 and Hb1AC was 5.24%.

3.1.2 Islet Cell Preparation

One hour prior to islet preparation, five wells in a 96-well culture plate were coated with 200 µL of 0.1% gelatin solution to aid in islet adherence. The following four experimental groups were: control, thapsigargin, high glucose (Hg), and ultrasound-treated (US). High-glucose and thapsigargin were chosen as positive controls as it is well known what their effects are in cell biology. Immediately after arrival, islets were seeded at ~1,000 IEQ per well to ensure optimal viability. The container the islets arrived in was gently agitated and emptied into a 50 mL flask, followed by centrifugation for 10 min in an Eppendorf Centrifuge 5430 R (Enfield, CT) at 22 ºC and 800 rcf. Once the 10 min ended, 6 mL extracellular supernatant and islet pellet were pipetted and dispensed into a 15 mL flask. The sample was then centrifuged again following the same parameters. The supernatant was then aspirated out and the islets were resuspended in 3 mL of islet media.

350 µL of free islet cell suspension was dispensed into each of the five wells and the plates were placed in an CO_2 incubator at 37ºC. Cell culturing media was replaced every 24 h to ensure a healthy cell culture and after at least 48 hours in culture, the islets were ready for treating and experimentation.

3.1.3 Cell Treatments

After at least 48 h of incubation, the islets were treated with 100 µM thapsigargin and 1mM high glucose. Based on the equation described previously, we were able to calculate the volume of compound necessary to yield the desired concentration. For

thapsigargin, a concentration of 0.5 μM was required, whereas a concentration of 15 μM was necessary for the high-glucose group.

1.75 μL of thapsigargin was added to 1 well containing 350 μL of cell suspension and 5.25 μL of high-glucose was added to another well. The plate was then placed in the incubator at 37ºC for 24 hours.

3.1.4 Ultrasound Administration

Ultrasound treatments were applied to the pre-defined wells 2 hours before the end point for the thapsigargin and high-glucose treated wells. Ultrasound was applied to the islet samples continuously for 5 minutes, one well after the other, with a frequency of 800 kHz at an intensity of 0.5 W/cm^2, utilizing the same setup as seen in Chapter 2.

3.1.5 RNA Extraction and Quantification

RNA extraction and quantification was executed following a protocol from an RNeasy Plus Mini Kit, obtained from Qiagen (Hilden, Germany) [82]. This kit contained 10 mL RNase free water, 10 mL of Buffer RW1Wash Buffer, 45 mL of Buffer RLT Plus Lysis Buffer, and 11 mL Buffer RPE Wash Buffer. Upon arrival of the kit, 44 mL of 95-100% ethanol was added to the Buffer RPE to create a working solution.

To begin the RNA extraction process, 350 μL of cell media was removed from each well in the 96-well plate. In each well 350 μL of Buffer RLT plus was dispensed to lyse the cells. The samples were then transferred into a gDNA eliminator spin column situated in a 2 mL collection tube. The gDNA eliminator spin columns containing the 350 μL of Buffer RLT plus and cell samples were centrifuged for 30 s using a Microfuge 18 Centrifuge at $\geq$ 10,000 RPM. After centrifugation, the column was disposed of in a waste container and the flow-through was saved. 350 μL of 70% ethanol was added directly to the tube

containing the flow-through and homogenized by pipetting. 700 µL of the sample and ethanol were then transferred to a RNeasy spin column in a 2 mL collection tube and centrifuged in the same microfuge for 15 s at 10,000 RPM. Once centrifuging was completed, the flow-through was discarded and the column was placed in a new 2 mL collection tube. Next, 700 µL of Buffer RW1 was added to the column and centrifuged for 15 s at 10,000 RPM. The flow-through was discarded and the column was placed in a new 2 mL collection tube. 500 µL of Buffer RPE was then dispensed into the column and the sample was centrifuged for 15 s at 10,000 RPM. The flow-through was then discarded and 500 µL of RPE was added to the column in a new 2 mL collection tube; this was centrifuged for 2 min at 10,000 RPM. The flow through was then discarded and the column was placed in a 1.5 mL collection tube. 40 µL of RNase free water was added directly to the column and the sample was centrifuged for 1 min at 10,000 RPM, to elute the RNA. The flow-through was then put on ice and the column discarded.

To quantify RNA, a NanoDrop One machine was used, following the same protocol described in Chapter 2.

3.1.6 cDNA Synthesis

cDNA was synthesized using a pre-defined protocol that corresponded with the applied biosystems high capacity cDNA reverse transcription kit from ThermoFisher Scientific (Waltham, MA), as previously described in Chapter 2 [81].

3.1.7 RT-qPCR

The tested genes were insulin, amylin, BiP and glucagon. Actin was used as a housekeeping gene to normalize the quantification cycle (Cq) values output by the PCR reaction.

The same protocol for cDNA dilution was followed as described in Chapter 2. The primers used for the gene expression analysis of pancreatic human islets were human insulin, human amylin, human BiP, human glucagon, and human actin. Specific information regarding each primer sequence can be found in *Table 4*. The primers were then diluted.

Table 4: Primer Sequences for Tested Genes; Primer sequences were derived from human samples for each of the tested genes.

Gene	**Forward Sequence**	**Reverse Sequence**
Actin	AGGCACCAGGGCGTGAT	GCCCACATGGAATCCTTCTGAC
Insulin	TGTCCTTCTGCCATGGCCCT	TTCACAAAGGCTGCGGCTGG
Glucagon	CAGGCAGACCCACTCAGTGA	CTGGTGAATGTGCCCTGTGA
Amylin	GCAAGTATTTCTCATTGTGCTCTC	GATGAGAGAATGGCACCAAAGT
BiP	GAACGTCTGATTGGCGATGC	ACCACCTTGAACGGCAAGAA

The master mix was prepared using SYBR Green supermix, the primer dilutions, and RNase/DNase Free Water. A set-up of the PCR plate can be found in *Figure 14*. The same PCR protocol used for Chapter 2 was followed to determine the fold change values for the samples described here.

CtA hINS 1	CtA hINS 2	TgA hINS 1	TgA hINS 2	HgA hINS 1	HgA hINS 2	UsA hINS 1	UsA hINS 2	UsB hINS 1	UsB hINS 2
CtA hAMY 1	CtA hAMY 2	TgA hAMY 1	TgA hAMY 2	HgA hAMY 1	HgA hAMY 2	UsA hAMY 1	UsA hAMY 2	UsB hAMY 1	UsB hAMY 2
CtA hACT 1	CtA hACT 2	TgA hACT 1	TgA hACT 2	HgA hACT 1	HgA hACT 2	UsA hACT 1	UsA hACT 2	UsB hACT 1	UsB hACT 2
CtA hGLU 1	CtA hGLU 2	TgA hGLU 1	TgA hGLU 2	HgA hGLU 1	HgA hGLU 2	UsA hGLU 1	UsA hGLU 2	UsB hGLU 1	UsB hGLU 2
CtA hBiP 1	CtA hBiP 2	TgA hBiP 1	TgA hBiP 2	HgA hBiP 1	HgA hBiP 2	UsA hBiP 1	UsA hBiP 2	UsB hBiP 1	UsB hBiP 2

Figure 14: PCR Plate for Human Pancreatic Islet Cell Gene Expression Analysis; Samples were plated in duplicate for each treatment with the corresponding gene to analyze the different effects.

Upon completion of the PCR reaction, Cq values were output for each gene. To calculate the fold change, the delta-delta Cq method was utilized.

3.1.8 Cell Viability

Cell viability of the donor human islet cells was assessed using a 0.4% Trypan Blue Dye Test. Immediately after the 5 min ultrasound application, the media was completely removed from each well in the 96-well plate and replaced with 30 µL of Trypsin EDTA, to detach the islets. The plate was then placed in an incubator at 37ºC for 2 min to allow for the effects of the trypsin to take place. After the 2 min, the bottom of each well was gently tapped to ensure complete detachment of the islets. 10 µL of the cells and trypsin were then transferred to a microvial containing 10 µL of 0.4% trypan blue.

10 µL of the trypan blue and cells was then pipetted onto a chamber and inserted into a Countess 3 automated cell counter (Invitrogen, Waltham, MA) to assess their viability. Once a percentage of live vs. dead cells was output by the machine, the slide was

moved to get a new field of view and the counting process was started again. An average percentage of live cells was then taken to assess the viability.

3.2 Results

Here, we analyze fold change in mRNA levels of the two main human islet β-cell hormones, insulin and amylin, across the different treated groups—thapsigargin, high-glucose, and ultrasound relative to non-treated (control) samples. A fold change of greater than 1 signifies an upregulation in gene expression, while a fold change of less than 1 corresponds to a downregulation of genetic expression.

For the insulin groups (*Figure 15*), the average fold change for the thapsigargin-treated and ultrasound-treated groups was found to be greater than 1. The high-glucose treated insulin groups yielded an average fold change of less than one. However, these findings were determined to be insignificant. Individual data points for each donor pancreatic islet sample are summarized in *Table 5*. Further visualization of the fold change after each treatment for insulin expression analysis are shown in *Figure 15*.

Table 5: Summary of Fold Change Values for each Treatment on Insulin Expression; A fold change of greater than 1 signifies an upregulation in expression, whereas a fold change of less than 1 indicates a downregulation.

	Control INS	**INS Tg**	**INS Hg**	**INS US**
N_1	1.00	3.32	1.00	0.82
N_2	1.00	1.88	0.92	1.63
N_3	1.00	0.95	1.16	1.08
N_4	1.00	1.06	1.57	2.10
N_5	1.00	1.33	1.11	1.24
N_6	1.00	0.84	0.57	0.13
N_7	1.00	1.01	1.06	1.22
N_8	1.00	0.93	0.60	1.29
N_9	1.00	0.84	0.90	0.79

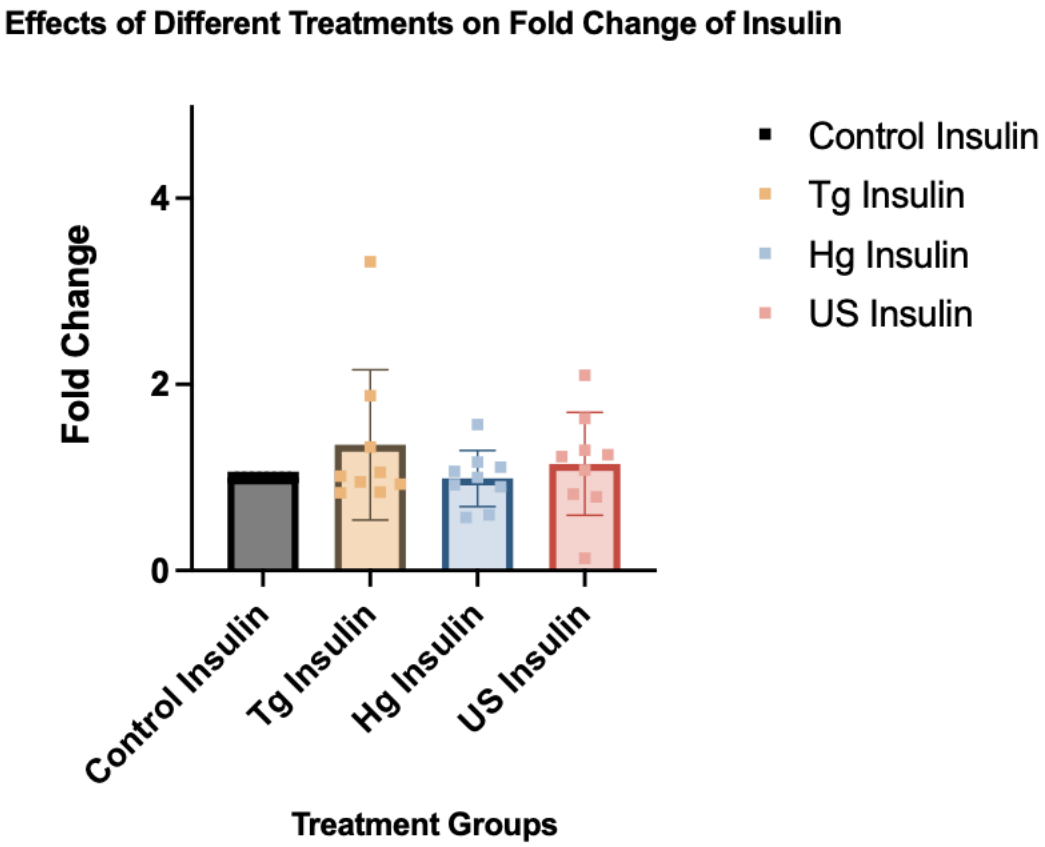

Figure 15: Effects of Different Treatments on Fold Change of Insulin; average fold change values appear as dots on the graph. The x-axis pertains to treatment groups, while the y-axis shows the different fold change values. The figure is color-coded to differentiate each of the treatment groups compared to the control. The data is shown as mean +/- standard deviation with individual fold change values shown as dots on the graph.

The glucagon groups (*Figure 16*) for thapsigargin, high-glucose and ultrasound-treatments all yielded an average fold change of greater than 1, indicating that this modality may have an effect of upregulation on this hormone, although statistical significance was not reported. Individual data points for each donor pancreatic islet sample are summarized in *Table 6*. Further visualization of the fold change after high-glucose treatment for the genes tested are shown in *Figure 16*.

Table 6: Summary of Fold Change Values for each Treatment on Glucagon Expression; A fold change of greater than 1 signifies an upregulation in expression, whereas a fold change of less than 1 indicates a downregulation.

	Glu Control	**Glu Tg**	**Glu Hg**	**Glu US**
N_1	1.00	2.84	0.68	0.94
N_2	1.00	0.57	1.22	0.61
N_3	1.00	1.25	1.64	1.12
N_4	1.00	3.03	0.02	4.41
N_5	1.00	1.55	1.21	2.31
N_6	1.00	16.9	5.46	1.64
N_7	1.00	1.48	1.53	1.25
N_8	1.00	0.74	0.78	0.99
N_9	1.00	0.91	0.67	1.15

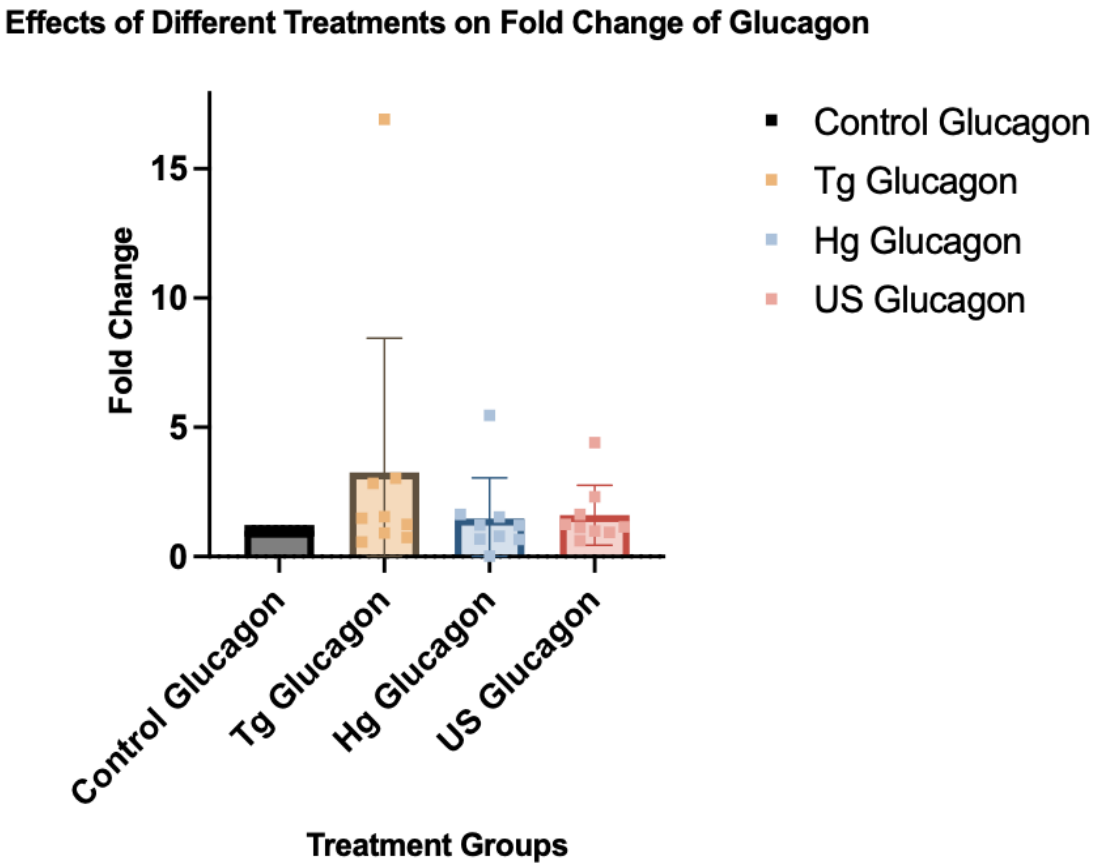

Figure 16: Effects of Different Treatments on Fold Change of Glucagon; average fold change values appear as dots on the graph. The x-axis pertains to treatment groups, while the y-axis shows the different fold change values. The figure is color-coded to differentiate each of the treatment groups compared to the control. The data is shown as mean +/- standard deviation with individual fold change values shown as dots on the graph.

The average fold change for the amylin groups (*Figure 17*) for thapsigargin, high-glucose, and ultrasound were found to be greater than 1. Likewise, BiP average fold change values were all found to be greater than one for each condition (*Figure 18*). No statistically significant differences were observed between experimental groups; however, amylin and BiP genes were more expressed by the ultrasound treatment as compared to insulin and glucagon genes (+88.3% insulin to amylin; +79.9% insulin to BiP; +59.9% glucagon to amylin; +50.5% glucagon to BiP). Individual data points for each donor pancreatic islet sample for amylin (*Table 7*) and BiP (*Table 8*) are summarized.

Table 7: Summary of Fold Change Values for each Treatment on Amylin Expression; A fold change of greater than 1 signifies an upregulation in expression, whereas a fold change of less than 1 indicates a downregulation.

	Amy Control	**Amy Tg**	**Amy Hg**	**Amy US**
N_1	1.00	6.28	9.25	1.74
N_2	1.00	2.03	2.77	2.01
N_3	1.00	3.14	5.78	8.28
N_4	1.00	1.21	0.74	8.31
N_5	1.00	1.09	1.93	0.41
N_6	1.00	2.14	2.83	1.07
N_7	1.00	0.05	2.93	1.29
N_8	1.00	0.37	1.59	0.65

Table 8: Summary of Fold Change Values for each Treatment on BiP Expression; A fold change of greater than 1 signifies an upregulation in expression, whereas a fold change of less than 1 indicates a downregulation.

	BiP Control	**BiP Tg**	**BiP Hg**	**BiP US**
N_1	1.00	8.57	0.83	1.59
N_2	1.00	2.16	1.04	0.53
N_3	1.00	0.21	0.13	1.53
N_4	1.00	1.05	0.97	0.81
N_5	1.00	11.7	11.5	11.0
N_6	1.00	1.13	1.35	1.67
N_7	1.00	0.04	0.95	3.43
N_8	1.00	1.00	0.66	0.87

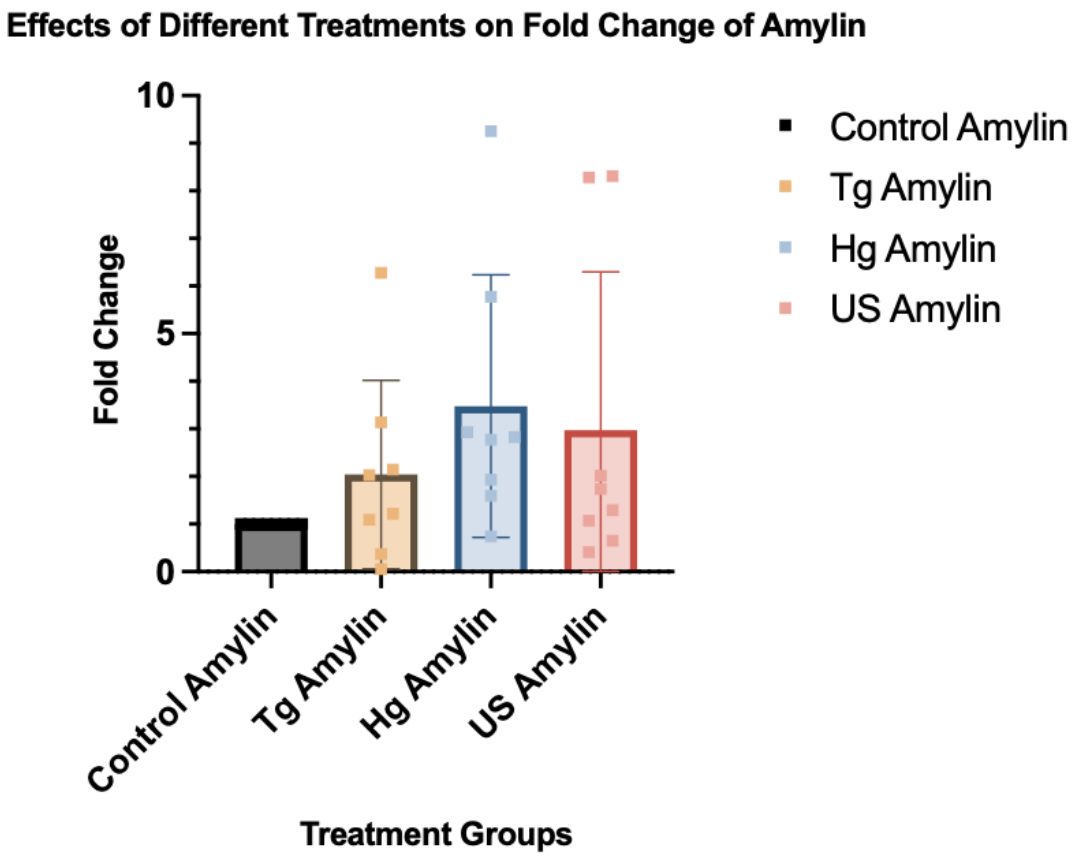

Figure 17: Effects of Different Treatments on Fold Change of Amylin; average fold change values appear as dots on the graph. The x-axis pertains to treatment groups, while the y-axis shows the different fold change values. The figure is color-coded to differentiate each of the treatment groups compared to the control. The data is shown as mean +/- standard deviation with individual fold change values shown as dots on the graph.

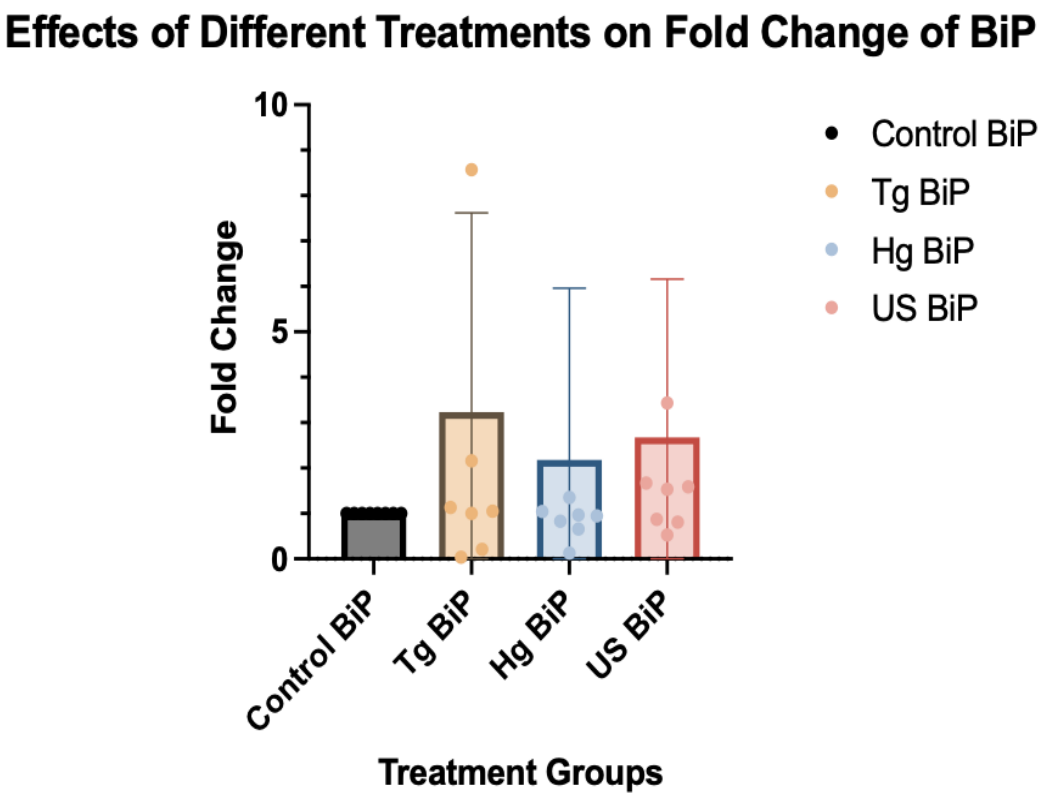

Figure 18: Effects of Different Treatments on Fold Change of BiP; average fold change values appear as dots on the graph. The x-axis pertains to treatment groups, while the y-axis shows the different fold change values. The figure is color-coded to differentiate each of the treatment groups compared to the control. The data is shown as mean +/- standard deviation with individual fold change values shown as dots on the graph.

The islet cells remained viable after ultrasound administration when compared with the control, showing an average of viability of 72.5% after treatment. On the other hand, the control wells showed an average viability of 68%, but this could be attributed to loss of cells during travel and/or culturing.

Statistical analysis was done using a one-way ANOVA statistical test, utilizing GraphPad Prism 10.1.1 (GraphPad Software, Inc., La Jolla, CA). The multiple comparisons function in GraphPad was used to compare each treatment for each hormone to the control value, to assess significance. Standard deviation and mean values were calculated using

the descriptive statistics function available in the column analyses in GraphPad. All figures related to the data were generated by GraphPad. Analysis of the control groups vs. ultrasound conditions for the data obtained from the insulin and glucagon revealed no significance (INS p = 0.5692; Glu p = 0.2231). Further a one-way ANOVA test analyzing the control groups vs. ultrasound conditions for the amylin and BiP groups showed no significant data (Amy p = 0.2863; BiP p = 0.3907). A summary of the relevant statistics for all conditions are shown relative to fold change (*Table 9*).

Table 9: Descriptive Statistics for Fold Change Data of Insulin, Glucagon, Amylin and BiP; Mean, standard deviation (STD), standard error of mean (SEM) and p-value are shown for each condition.

	INS Tg	INS Hg	INS US	Glu Tg	Glu Hg	Glu US	Amy Tg	Amy Hg	Amy US	BiP Tg	BiP Hg	BiP US
Mean	1.35	0.99	1.15	3.25	1.47	1.60	2.04	3.48	2.97	3.23	2.17	2.68
STD	0.81	0.30	0.55	5.20	1.58	1.16	1.98	2.76	3.33	4.39	3.77	3.48
SEM	0.27	0.10	0.18	1.73	0.53	0.39	0.70	0.98	1.18	1.55	1.33	1.23
p-value	0.35	0.99	0.88	0.22	0.97	0.94	0.77	0.13	0.29	0.42	0.83	0.63

3.3 Discussion and Conclusions

We investigated the effects of targeted therapeutic ultrasound therapy on the transcriptional modulation of key islet hormones involved in the regulation of glucose metabolism, namely insulin, glucagon, and amylin. Our experimental setup was designed with the goal of analyzing hormone's gene expression and regulation after administration of low-intensity ultrasound to determine the mechanisms of the previously observed ultrasound-stimulation of insulin secretion as a potential strategy that could address the

secretory defects associated with type 2 diabetes mellitus. Conclusions were drawn from analysis of fold change data between control and treatment groups.

We expected that an observed increase in the rate of insulin release by ultrasound would be evoked by the calcium dependent stimulation of secretory processes previously described. Additionally, we hypothesized that ultrasound application would stimulate transcription of other genes, such as amylin and glucagon—indicating that ultrasound could indeed regulate gene transcription and protein production. While therapeutic ultrasound has shown the ability to influence gene expression in certain contexts, here we report that that no significant changes in insulin or glucagon mRNA levels were detected. The lack of observable changes in gene regulation following low-intensity ultrasound treatment can be attributed to several factors. Firstly, modulation of gene expression is highly dependent on specific treatment parameters, including intensity, frequency, duration, and spatial distribution [83]. With an intensity of 0.5 W/cm^2 at 800 kHz and an incubation time of 1 hr, changes in gene expression might not occur due to the lower intensity and potentially insufficient amount of time to allow for transcription and translation to occur. Moreover, it is possible that the observation period following ultrasound administration was not optimal for capturing any potential alterations in the expression of the target genes. Another potential cause for this finding could be that the epigenetic and genetic differences existed between specific donor samples, as well as variations in the health and function of the pancreatic islet cells, which could influence their responsiveness to ultrasound [84]. Although no significant gene expression changes were observed in our sonogenetic studies, an interesting finding was that the ultrasound administration appeared to be more stimulatory to amylin and BiP as compared to the other

two islet hormones, indicating a selective effect of ultrasound on islet gene expression. In agreement with this finding, our previous studies demonstrate concurrent increases in amylin and BiP mRNA levels in HG-challenged pancreatic β-cells [85]. Based on our findings, further experimentation with a different set of ultrasound parameters with a goal of maximizing insulin secretion while minimizing secretion of glucagon, should be assessed. The selected ultrasound treatment parameters do not appear to significantly affect the gene expression of insulin, glucagon, amylin, or BiP. Further, no significant loss in cell viability was observed after ultrasound treatment. Additionally, a relatively low sample size was used to determine the effects of ultrasound administration on the genetic modulation of human donor pancreatic cells, which could have affected the significance of these results. For example, a power-analysis test using G*Power taking into account a one tailed t-test with power size 0.8, effect size 0.39, and $\alpha \leq 0.05$ indicated that 82 samples would be required to observe significant data related to fold change of insulin in control vs. ultrasound-treated groups. However, based on our previous ultrasound experiments performed on insulinoma cells [72], [73], [75], we expect that ultrasound does have a biologically-relevant effect on the islet cells although not necessarily on their gene expression.

3.4 Alternative Approaches

While work is still being completed to explain the reasons behind why this approach did not yield significant data, more thorough analysis into the mechanisms behind ultrasound modulation of gene expression can be still be done. For example, computational modeling can be done in programs such as k-wave to generate simulation data on ultrasound values achieved in a micro-well plate compared to a Petri-dish. This strategy

has the potential to explain the lack of stimulatory action of ultrasound that we saw in the gene expression studies previously described. Further, experimental data of ultrasound application both below and above the micro-well plate can be done to determine whether a greater effect of ultrasound is seen with a different experimental set-up.

Chapter 4: Ultrasound Stimulation of Insulinoma β-cells in a Perfusion Chamber

4.1 Computational Modeling

4.1.1 K-Wave

To address this aim, the k-wave toolbox in MATLAB was utilized to perform ultrasound simulations in tissue-realistic media. This toolbox is commonly used to aide in optimization of *in vitro* systems due to its capability in simulating the behavior of ultrasound through heterogenous media and further model thermal and mechanical forces of therapeutic ultrasound transducers acting on tissue [86]. Although k-wave has uses ranging from 1-dimenional (1D) to 3-dimensional simulations (3D), we made use of a 2-dimensional (2D) simulation to allow for the local PCs in our lab to run the simulation.

k-wave works through using a serious of first-order partial differential equations to calculate spatial gradients and temporal gradients. An important concept to understand for the purposes of our model is the split-field perfectly matched layer (PML); this is used to absorb waves at the edges of the computational domain–the main advantage of the numerical model used in k-Wave compared to models based on finite-difference time domain (FDTD) schemes is that fewer spatial and temporal grid points are needed for accurate simulations [86].

A simple 2D representation of the forces exerted on tissue by ultrasound therapy treatment of INS cells in a 96-well plate was created, as well as representation of ultrasound treatment of INS cells in a constructed perfusion chamber available in our lab. This has the

purpose of showing that ultrasound therapy does not contribute to thermal or mechanical stress affecting cell viability. The simulation created is based on many different components, such as definition of PML size, establishment of properties of the propagation medium, creation of the transducer and signal, running of thermal section of MATLAB script after pressure simulation is completed, and finally visualizing the thermal and mechanical effects of ultrasound stimulation on the perfusion system. The entirety of the simulation can be found in *Appendix A*.

4.1.2 Perfectly Matched Layer (PML)

This script initializes a perfectly matched layer (PML) to effectively absorb acoustic signals upon their arrival at the outer boundaries of the simulation. Subsequently, it establishes a matrix of dimensions 300x300, with each point being precisely spaced by intervals dx or dy. These intervals are deliberately chosen and not arbitrary. For example, k-Wave implements a PML_size of 20 for a 2D simulation such as this. Considering PML, we were able to determine the number of grid points necessary in both the x and y directions to create the most optimized simulation with the tools we had access too. Specifically, the choice of 300x300 (Nx, Ny) dimensions is carefully calibrated to match the computational capacity of a standard laptop, taking into account the micro-scale of dx/dy and the nano-scale of dt. For determining dx, a comprehensive understanding of the total number of points (300) and the overall distance in that specific direction (7.01 mm) was needed. 7.01 mm was determined through measuring the layers of the different components of the sandwich (i.e., gel layer = 0.5 mm, glass layer = 0.5 mm, INS cell layer = 0.01 mm, media layer = 3 mm, plexiglass layer = 3 mm) and adding them together. Consequently, the calculation of dx involves the equation dx * 300 = 7.01, leading to the derivation of dx as

0.02337 m, which is then incorporated into the script. A parallel methodology is employed to compute dy, where y * 300 = 25 mm (length of plexiglass chamber), and y is calculated. A representation of the perfusion chamber with the specific layers and their measurements is shown in *Figure 19*.

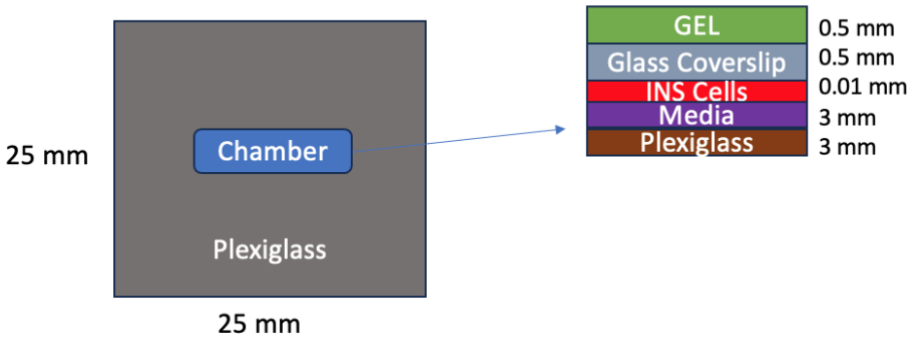

Figure 19: Illustration of Perfusion Chamber with Dimensions of Material Layers; From top to bottom in the system, we applied gel to couple the transducer to the chamber, followed by the coverslip with the INS cells adhered to the surface, with the media perfusing through the system and the bottom of the plexiglass layer.

4.1.3 Establishment of Properties of Propagation Medium

The next section of the script requires the user to define specific parameters of different properties of the propagation medium to create the experimental space and allow for extraction of both pressure and thermal data. For the purposes of our simulation, we have defined properties for the gel used to couple the transducer to the perfusion chamber, the 22x22 glass coverslip that the INS cells are plated on, the INS cells, the INS cell media used to perfuse the system, and the plexiglass perfusion chamber. The properties necessary to define to create this space are the medium sound speed, the medium density, and the medium alpha-coefficient. These values were discovered through an extensive literature review and the individual data can be seen in *Table 10*.

Table 10: Defining Properties of Propagation Medium for Perfusion System; Values were obtained from a literature surface to identify the different data necessary for each parameter that k-wave called for.

	Medium Sound Speed (m/s)	Medium Density (kg/m^3)	Medium Alpha-Coefficient
Gel	1500 [87]	1000 [87]	0.0022 [88]
Glass Coverslip	1700 [89]	1190 [90]	0.6 [91]
INS cells	1591 [92]	1087 [92]	0.7904 [92]
Media	1525 [93]	1000 [94]	0.0022 [88]
Plexiglass Chamber	1700 [89]	1190 [90]	0.51 [95]

From the above data, we were able to create a computational grid to model the experimental space of the perfusion system. This was done by using the function, kgrid = kWaveGrid (Nx, dx, Ny, dy) to create a sandwich representation of each layer in the simulation, to help visualize the simulation space by material. A visualization of the experimental space based on material is shown in *Figure 19*, where the ultrasound transducer is oriented above the perfusion chamber. In both the x and y directions, the axes correspond to Nx and Ny, where Nx = 320 – PML and Ny = 320 – PML, indicating a 300x300 experimental space.

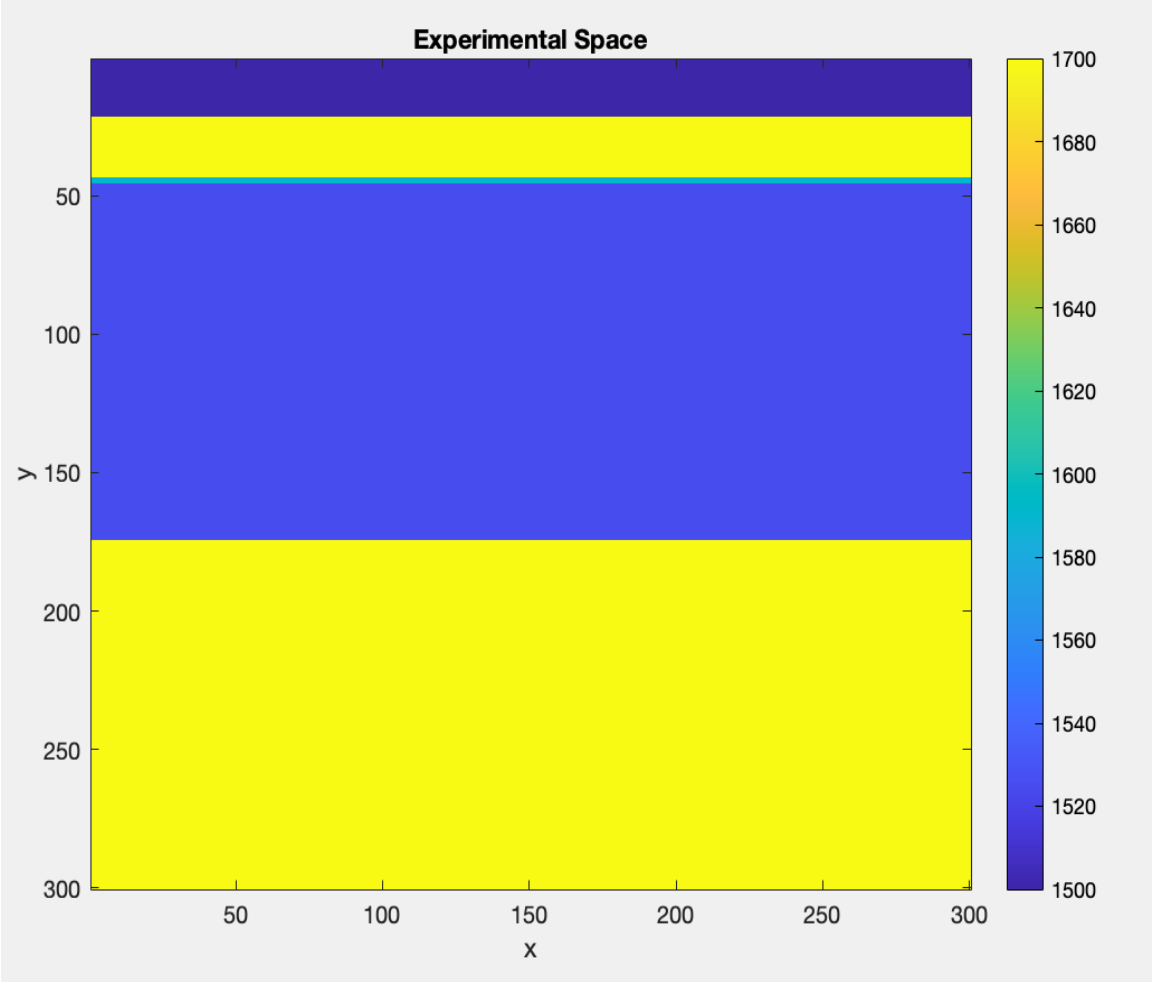

Figure 20: Experimental Space for Simulation; In this simulation, the ultrasound transducer is oriented at the top of the figure, followed by the gel, glass coverslip, INS cell layer, media, and the plexiglass layer—these are separated based on points in the y-direction. The units for the x- and y-axis correspond to each point within the space, while the legend on the right of the figure is in units of m/s, relating to medium sound speed.

Based on the experimental space seen in *Figure 19*, points 0-22 correspond to the gel, 22-43 the glass coverslip, 44-45 the INS cell layer, 46-174 the media, and 175-300 the plexiglass layer.

4.1.4 Creation of Transducer Signal

This section predominantly involves the preloading of specific parameters from the k-wave toolbox into the MATLAB workspace. Notably, it entails the retrieval of pertinent attributes of the transducer we will use in the actual *in vitro* experiments, including the aperture's diameter (0 m), the aperture's radius (7.51e-2 m), the operating frequency

(800,000 Hz), and the amplitude (0.182e6 Pa). Furthermore, a distinct segment dedicated to pulse-wave (PW) administration is integrated within the code mirroring the continuous-wave script (CW) except for implementation of a precisely defined dosing regimen. The dosing regimen includes a 0.5 Hz pulse repetition frequency with 5% duty cycle and 5 min treatment length. From this data, we created a tone burst signal that functions through t_on – 0.125 s, t_off – 0.025 s, and this signal repeats for 100 cycles. Thus, the t_total is equal to 15 s of pulsing ultrasound and 45 s of no treatment, which reflects past studies from our lab that utilized pulsed ultrasound [96]. Sample calculations for t_off, and t_total are shown below, where pulse width is equal to 0.05, time period of cycle is equal to 0.5:

$$t_{off} = \frac{pulse\ width}{time\ period\ of\ cycle}$$

$$t_{total} = \#\ of\ cycles * (t_{on} + t_{off})$$

However, since we will make use of continuous, unfocused ultrasound in the actual experimentation with the perfusion chamber, the pulsed section of this script is not necessary for our purposes. This section as included in the code in the case that a future study from our lab would employ pulsed ultrasound to investigate its effects with perfusion.

4.1.5 Pressure Simulation

Based on the outcomes derived from the pressure simulation, conducted in units of megapascals (MPa), it is evident that the majority of pressure is concentrated at the position of the transducer within the experimental domain. Furthermore, an observed trend indicates a gradual attenuation of pressure values as the energy wave propagates through the medium under investigation. This observation is consistent with the principles of wave propagation and the dissipative behavior of energy in a medium, as described in study done by

Dukkipati and Rao, where the mechanical vibrations of waves was defined [97]. This is shown in *Figure 21*.

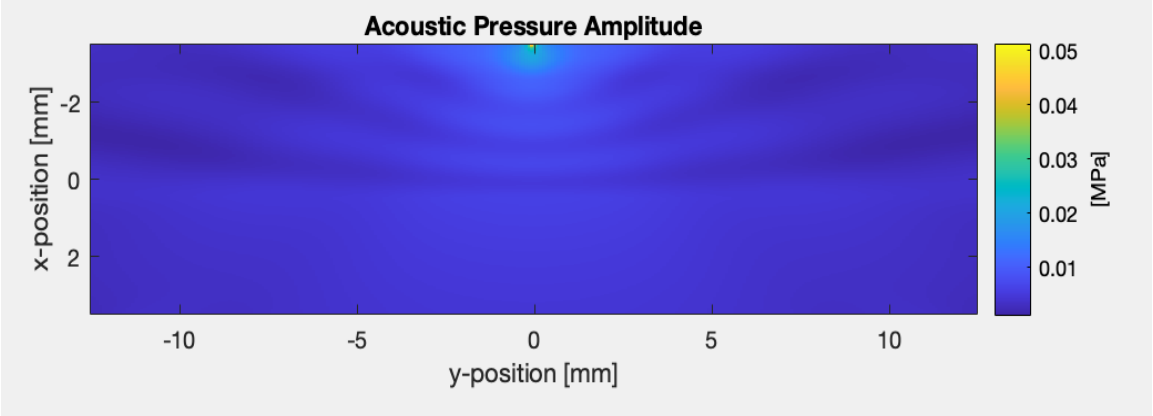

Figure 21: Results of Acoustic Pressure Simulation; Most of the pressure exerted by the transducer is emitting from the actual location of the transducer, with an observed gradual attenuation throughout the experimental space.

4.1.6 Thermal Simulation

From the thermal analysis of the simulation, it was observed that there were no significant fluctuations in temperature, with minute increments on the scale of 0.001 °C recorded in close proximity to both the ultrasound transducer and the plexiglass layer. The anticipated elevation in temperature within these designated areas is in accordance with energy conversion, where a considerable portion of the mechanical energy conveyed by the transducer is transformed into heat [98]. This thermal energy is presumed to have been absorbed by the plexiglass enclosure. Notably, the simulation's estimated temperature alterations are expected to be conservative, considering the likely inefficiency of the transducer converting some of the input energy into thermal radiation as opposed to acoustic output [99]. These results are shown in *Figure 22*.

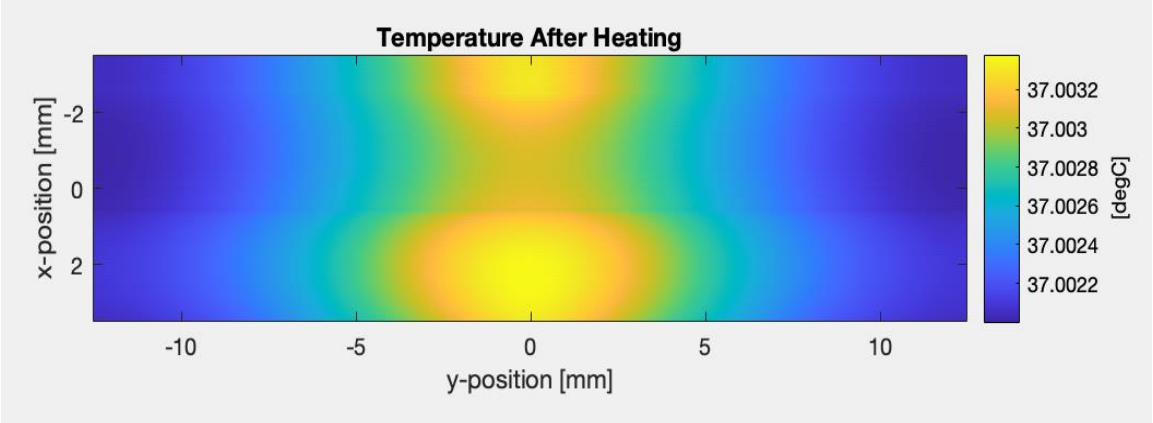

Figure 22: Temperature After Heating from Ultrasound Administration; Temperature increases are shown in yellow near the ultrasound transducer and the plexiglass layer of the experimental space.

Similarly, discernible changes in the volume rate of heat deposition are not observed during the administration of ultrasound within the simulation. This phenomenon denotes the dynamic process of energy conversion into thermal energy within the medium due to the absorption of ultrasound waves [100]. The potential repercussions of excessive heat deposition, including tissue damage and undesirable outcomes, underscore the importance of regulating the heat deposition rate [101]. The absence of significant heat deposition noted in this simulation serves as an indicator of the safe administration of ultrasound, affirming the viability of our approach for ultrasound delivery within the experimental setup. This data is shown in *Figure 23*.

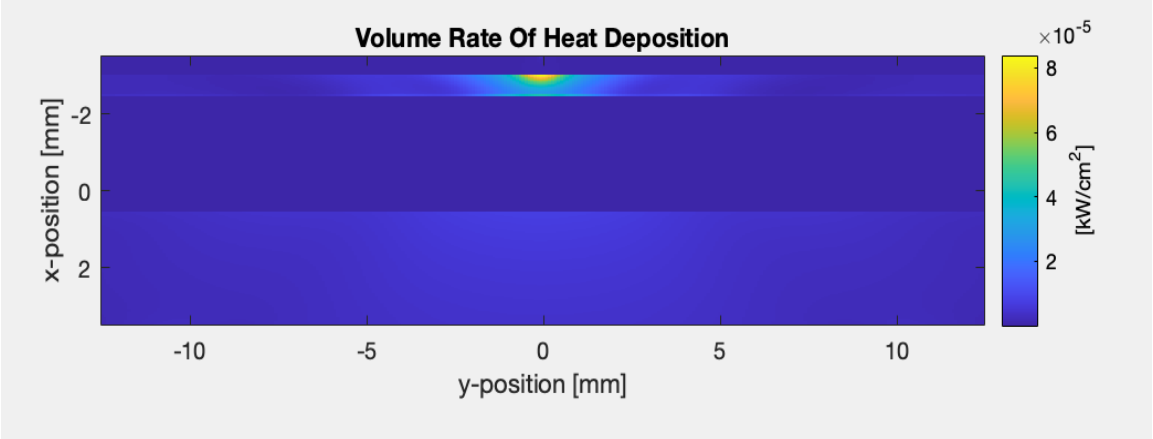

Figure 23: Volume Rate of Heat Deposition; No significant heat deposition was shown throughout the system, with any responses shown near the ultrasound transducer.

4.2 Conclusions

Based on the k-wave model's pressure and thermal simulations, our findings affirm the safe and efficient application of ultrasound to insulinoma cells in the perfusion chamber, mitigating potential adverse impacts related to thermal and mechanical effects. While we have concluded the initial simulation, ongoing adjustments are being made to optimize the ongoing second part of these studies.

4.3 Protein secretion of insulin in INS β-cell lines

4.3.1 Quantification of Protein Secretion (ELISA)

4.3.1.1 Sandwich ELISA

The experimental procedures involved the measurement of insulin following ultrasound administration, which was conducted using a sandwich Enzyme-Linked Immunosorbent Assay (ELISA) kit. The insulin ELISA operates through a systematic four-step process [102]. Initially, insulin molecules are captured from the sample suspension in each well of a pre-coated microtiter plate using a monoclonal mouse anti-rat antibody. Subsequently, a biotinylated

polyclonal antibody binds to the captured protein. Following this, the unbound materials are washed away, and horseradish peroxidase (HRP) is affixed to the immobilized biotinylated antibodies. The sample is then cleansed of any free enzyme conjugates, and the quantification of the immobilized antibody-enzyme conjugates is achieved by monitoring the activity of horseradish peroxidase in the presence of the substrate 3,3',5,5'-tetramethylbenzidine (TMB). Enzyme activity is measured at an absorbance of 450 nm, with correction from an absorbency of 590 nm post acidification of the formed products. The relationship between absorbency and the quantity of the captured protein in the sample enables the creation of a reference curve based on reference standards. An example of the principle behind the sandwich ELISA can be seen in *Figure 24*.

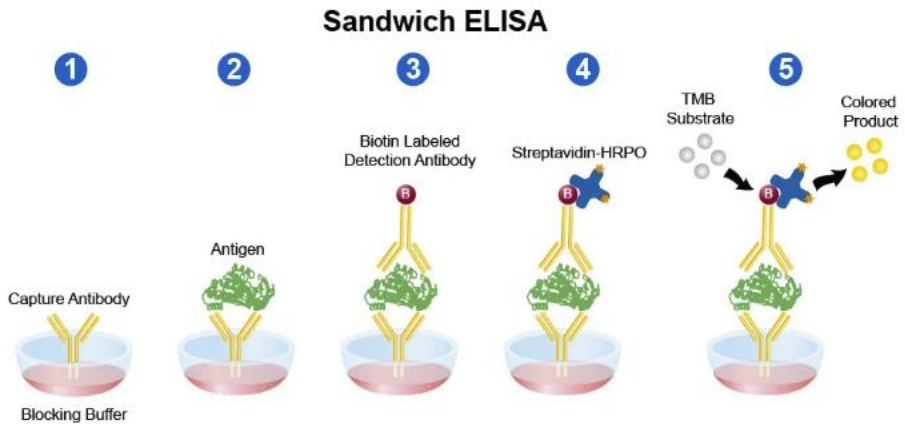

Figure 24: Sandwich ELISA Principle; Specific steps in the mechanism of how this kit works to analyze protein secretion [102].

Relevant definitions of different components utilized in the ELISA procedure can be seen in *Table 11*.

Table 11: Relevant Definitions of Components in an ELISA; Streptavidin-HRP serves as the detection antibody, with TMB substrate as the substrate solution to continue the reaction.

Component	Definition
Streptavidin-HRP (Detection Antibody)	A detection reagent used to detect biotin conjugated primary antibodies [103]
TMB Substrate (Substrate Solution)	A chromogenic substrate; HRP will oxidize TMB once added, turning solution in wells to a blue color [104]
Stop Solution	A solution added to stop the peroxidase/TMB reaction at which point solution in wells will turn yellow [105]

4.4 Methods

4.4.1 INS Cell Preparation

Thawing and culturing of INS 832/13 rat insulinoma cells were carried out according to established protocols outlined in Chapter 2.

4.4.2 Preparation of Coverslips

For coverslip preparation, 22x22 mm coverslips were utilized. A rigorous cleaning procedure was conducted to establish a sterile environment conducive for INS cell adherence and perfusion. Coverslips were suspended in a rack within a container placed in the fume hood. Subsequently, 400 mL of xylene was introduced into the container and allowed to stand for a minimum of 8-10 hours. After this period, the xylene was replaced with 400 mL of chloroform, and the container was left undisturbed for another 8-10 hours. Following the chloroform step, the solution was replaced with 400 mL of undiluted ethanol and left for 8-10 hours. Once the cleaning process was completed, coverslips were transferred to a biosafety cabinet for drying for at least 1 hour. Once dry, coverslips were individually placed in 35 mm Petri dishes in preparation for coating with poly-D-lysine (PDL).

4.4.3 Coverslip Coating

Prior to plating, coverslips underwent a PDL coating procedure to facilitate adherence. 80 µL of PDL solution was applied to the center of each coverslip in the Petri dish, followed by a 3-hour incubation at room temperature. Subsequently, the PDL was replaced with 100 µL of nanopure water, incubated for 1 hour, and then replaced with fresh nanopure water for another hour. After drying, INS cells were plated onto the coverslips.

4.4.4 Plating Coverslips

For cell plating, INS cells, following passage as per Chapter 2, were diluted at a ratio of 1:4 in low-glucose INS media. 80 µL of cell suspension was then added to the center of each PDL-coated coverslip. Petri dishes were then placed in a CO_2 incubator at 37°C for at least 1 hour. Following confirmation of cell adhesion under a microscope, 100 µL of media was added to the Petri dishes followed by 1 hr incubation. Finally, 3 mL of media was added to the dish covering both the bottom and the coverslip. The dishes were then incubated for a minimum of 24 hours to ensure proper cell attachment.

4.4.5 Preparation of Treatments

Treatment preparation involved the calculation of volumes of 1 mM Hg and 500 nM Tg needed according to the formula outlined in Chapter 2. The required concentrations were achieved by diluting stock solutions in 10 mL of 5 mM glucose-Krebs Ringer Buffer (KBS). Perfusions were then prepared with the designated solutions, including 20 mM high glucose and 50 µM thapsigargin, after thorough system cleaning. A sample calculation is shown below, where 0.0005 mM Tg corresponds to 500 nM Tg and 0.05 mM serves as the concentration needed (50 µM).

$$(10\ mL\ glucose - KBS)(0.0005\ mM\ Tg) = (0.05\ mM\ Tg)(V_2)$$

4.4.6 Perfusion

Before starting the perfusion experiments, the system underwent a comprehensive cleaning process involving two flushes with deionized water. An image of the perfusion chamber used for these experiments is shown in *Figure 25*. Perfusate syringes were then filled with the designated solutions and connected to the manifold via tubing. To prepare the perfusion chamber, the surfaces of the chamber components were coated with Molykote High Vacuum Grease (DuPont, Wilmington, DE). This involved a precise application of a thin layer of the grease to the inner rims of the top and bottom metal components, as well as an even distribution across the plexiglass component. Prior to fixing the coverslip containing the INS cells, a comprehensive microscopic inspection of the chamber was conducted to verify uniform grease coating, as any irregularities may lead to leakage during the perfusion process. Upon successful coating, the coverslip was removed from the Petri dish, excess media was eliminated using a kim-wipe through tapping the edge of the slip, and the coverslip was carefully placed cell-side down onto the chamber. This positioning ensured unimpeded access for the KBS and treatment solutions during perfusion. Following this, the plexiglass and coverslip assembly were enclosed within the metal chamber components and securely sealed using the provided screws. The entire setup was then connected to the tubing within the perfusion system, with checks for any signs of leakage. A 30 min equilibration period was done, during which 5 mM glucose KBS will flow through the system. Subsequently, data collection was started.

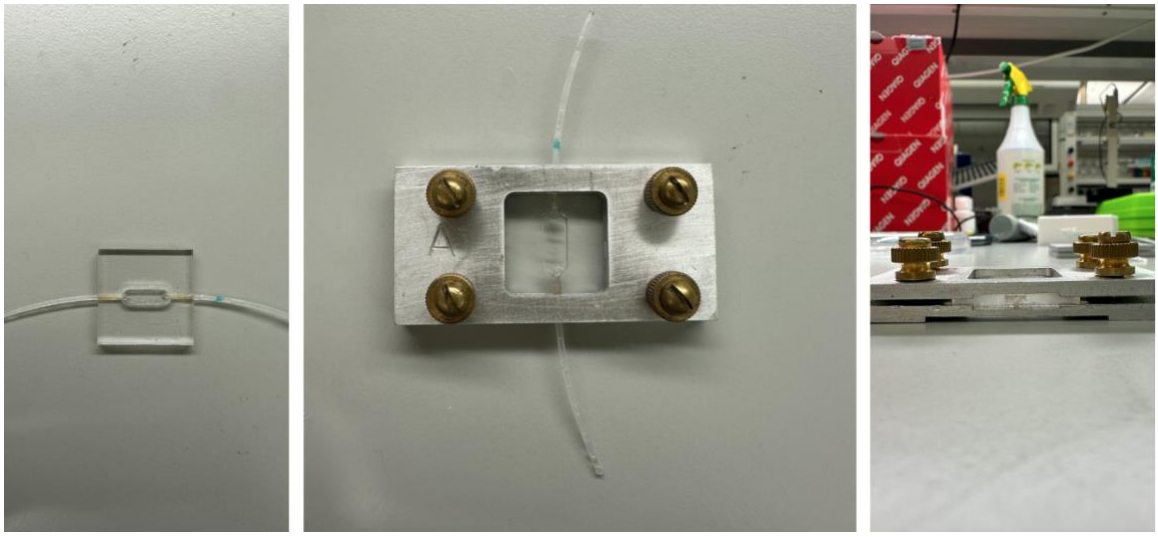

Figure 25: Perfusion Chamber and Plexiglass Layer; The coverslip is adhered to the plexiglass layer via high-vacuum grease and the whole component is sealed within the chamber and screwed shut as shown. Tubing is fed through the inlet and outlet of the plexiglass layer to allow the perfusate to travel through to reach the cells.

4.4.7 Treatment Protocol and Sample Collection

Treatment groups consisted of 20 mM high glucose and 50 μM thapsigargin, with 5 mM glucose-KBS serving as the control. Additionally, an ultrasound treatment group at 800 kHz and intensity of 0.5 W/cm^2 was administered for 5 minutes. Sample collection occurred every 2 minutes over a total period of 94 minutes, with system flushing between treatments using 5 mM glucose-KBS. Overall we completed 3 experiments (n = 3). Details of individual treatment durations are provided in *Table 12*. It is important to note that challenges were faced related to system leaking, likely due to the relatively high pressure experienced by our system compared to the system components ability to withstand such forces, causing the coverslip to detach from the plexiglass, resulting in leakage. Optimization of the system was done with multiple iterations comprising different plexiglass components and PDMS lining to attempt to improve upon this leakage problem, with data able to be obtained from the perfusion components shown in *Figure 25*, excluding the PDMS lining.

Table 12: Treatment Protocol and Sample Collection for Perfusion; A 30 min equilibration with 5 mM glucose KBS was done, followed by 5 min ultrasound, 30 min 20 mM high glucose, 5 min 50 μM thapsigargin and a 10 min period with 5 mM glucose KBS. In between each treatment, system was flushed with 5 mM glucose KBS to wash out previous treatment.

Time (min)	Treatment
t = - 30 min → t = - 25 min	5 mM Glucose KBS
t = - 25 min → t = -20 min	5 mM Glucose KBS
t = - 20 min → t = - 15 min	5 mM Glucose KBS
t = -15 min → t = - 10 min	5 mM Glucose KBS
t = -10 min → t = - 5 min	5 mM Glucose KBS
t = - 5 min → t = 0 min	5 mM Glucose KBS
t = 0 min → t = 6 min	800 kHz Ultrasound, 0.5 W/cm^2, 5 min continuous
t = 6 min → t = 12 min	5 mM Glucose KBS
t = 12 min → t = 42 min	20 mM High Glucose
t = 42 min → t = 48 min	5 mM Glucose KBS
t = 48 min → t = 54 min	50 μM Thapsigargin
t = 54 min → t = 64 min	5 mM Glucose KBS

4.4.8 Rat/Mouse Insulin ELISA

Before starting the insulin ELISA, it was necessary to pre-warm all required reagents to room temperature (20-22°C). The 10X wash buffer concentrate was diluted ten-fold by mixing it with 450 mL of deionized water. The provided strips were assembled into the plate holder, and each well in the microtiter plate underwent three washes with 300 μL of the diluted Wash Buffer. After each wash, the wash buffer was removed from the

microtiter plate by tapping it onto the supplied absorbent towels. This process ensured the complete removal of the wash buffer; however, it was essential not to allow the wells to dry out completely, as dried wells could cause non-specific binding of analytes or loss of reagent activity.

Once the washing steps were completed, 10 µL of assay buffer was added to each blank and sample well, following a specific plate orientation. Blank and standard wells were plated in duplicate in the first two rows of the microtiter plate, followed by duplicate plating of each time point collection from the perfusion setup in the remaining wells. Additionally, 10 µL of assay buffer was added to the standard wells, and 10 µL of the provided rat insulin standards was added to the corresponding wells, in ascending concentration. Following this, 10 µL of the quality controls was added to the QC 1 and QC 2 wells. In the remaining wells, 10 µL of samples was added in duplicates. Once all the wells contained their respective solutions, 80 µL of detection antibody was added to all wells. The plate was covered and allowed to incubate at room temperature for 2 hours on an orbital microtiter plate shaker set to 400-500 RPM.

After the 2 hours, the contents of the plate were removed by tapping onto an absorbent towel, and three washes with diluted Wash Buffer were completed using 300 µL per wash. 100 µL of enzyme solution was added to all wells, and the plate was covered and placed on the shaker for an additional 30 minutes of incubation at room temperature. The plate was then tapped again on the absorbent towel to remove the contents and washed an additional six times using the previously described method. 100 µL of substrate solution was then added to each well, and the plate was placed on the orbital shaker for an additional 5-20 minutes. The incubation time was determined by observing when all wells turned

blue, indicating the presence of insulin. Subsequently, 100 μL of stop solution was added to each well, causing the solution to turn yellow, and the plate was then placed in the plate reader to read absorbance values at 450 nm and 590 nm. The difference between absorbance units was recorded, and an optical density reference curve was generated to calculate insulin concentration.

4.5 Results

In this study, we conducted an analysis of insulin concentration dynamics over time in a perfused system. Initial data collection spanned a 30-minute period to establish baseline measurements for subsequent treatments. Baseline measurements, denoted as -30 min, -25 min, -20 min, -15 min, -10 min, and -5 min, were recorded for comparative analysis. Upon application of unfocused, continuous ultrasound for 5 minutes at a frequency of 800 kHz and an intensity of 0.5 W/cm², a significant increase in insulin concentrations was observed at t = 2 min and t = 4 min, relative to baseline levels. At the onset of high-glucose treatment (t = 14 min), no immediate rise in insulin concentration was noted, potentially attributable to the dead volume effect, accounting for approximately 3 minutes for the treatment to reach cellular targets. Notably, between t = 20 min and t = 26 min, a significant increase in insulin concentration was observed, characteristic of the first phase of insulin release in response to heightened glucose levels, displaying a distinct spike in insulin secretion. Subsequent values plateaued with a minor decline at t = 28 min, followed by another plateau and gradual increase starting at t = 32 min, indicative of the second phase of insulin release. Data acquired between t = 28 min and t = 40 min yielded significant findings. Although a decline in insulin concentration was evident at t = 42 min, statistical significance was not achieved.

Introduction of thapsigargin into the system at t = 50 min and continuous perfusion until t = 54 min did not elicit any discernible change in insulin concentration. It is noteworthy that the concentration of thapsigargin (50 μM) used in this study approached levels considered potentially cytotoxic [106], which could have led to cell rupture and a subsequent increase in insulin levels. Thapsigargin is a known inhibitor of the sarco/endoplasmic reticulum (ER) Ca2+-ATPase (SERCA) pump, and has been shown to inhibit calcium homeostasis through increase of intracellular levels, and higher levels can lead to cell death [107]. However, our findings suggest that this concentration of thapsigargin did not induce cell death, underscoring the resilience of cells to ER stress at this dosage. This observation provides evidence that higher concentrations of thapsigargin may not necessarily pose a threat to cellular viability.

Furthermore, we investigated whether disparities in peak insulin values between ultrasound treatment and high-glucose treatment yielded significant differences. Peak insulin concentration during ultrasound administration was recorded at 4.43 ng/mL at t = 4 min, whereas during the first phase of insulin release under high glucose conditions, the peak insulin concentration was 11.10 ng/mL at t = 22 min, and during the second phase, it was 8.80 ng/mL at t = 34 min. The variance in peak values between ultrasound administration and high-glucose treatment for both first and second phases of insulin release was deemed statistically significant (t = 4 min vs. t = 22 min, p = 0.0007; t = 4 min vs. t = 34 min, p = 0.0006). Notably, the insulin response to ultrasound closely resembled that of the first phase of insulin release, suggesting that the mechanism underlying ultrasound-induced insulin secretion mirrors that of initial phase responses. Detailed insulin concentration data at different time points for ultrasound treatment are shown in

Table 13, while *Table 14* illustrates the concentration during the high glucose condition, and *Table 15* shows the thapsigargin result. *Figure 26* depicts the temporal changes in insulin concentration via a line graph.

Table 13: Changes in Insulin Concentration (ng/mL) Over Time After Administration of 800 kHz Ultrasound at intensity of 0.5 W/cm^2 for 5 min, continuously; Concentration for each data set is shown in the table with mean and standard error of mean. "**" denotes significant data ($p < 0.01$).

	Insulin Concentration (ng/mL)		
	t = 2 min	t = 4 min	t = 6 min
N_1	3.24	4.26	0.35
N_2	3.19	5.30	0.45
N_3	3.96	4.24	0.35
Average	3.46**	4.43**	0.36
SEM	0.25	0.29	0.01

Table 14: Changes in Insulin Concentration (ng/mL) Over Time After Administration of 20 mM High Glucose for 30 min; Concentration for each data set is shown in the table with mean and standard error of mean. "*" = ($p< 0.05$), "**" = ($p < 0.01$), "***" = ($p <0.001$).

	Insulin Concentration (ng/mL)														
	t = 14 min	t = 16 min	t = 18 min	t = 20 min	t = 22 min	t = 24 min	t = 26 min	t = 28 min	t = 30 min	t = 32 min	t = 34 min	t = 36 min	t = 38 min	t = 40 min	t = 42 min
N_1	0.36	0.32	0.33	6.57	10.9	10.3	10.2	7.09	7.52	7.63	8.64	8.62	8.12	7.87	2.95
N_2	0.46	0.43	0.47	8.88	12.3	11.9	11.2	8.76	8.83	8.93	9.31	9.76	9.95	9.58	3.94
N_3	0.36	0.31	0.36	8.77	11.6	12.5	12.4	7.55	7.99	7.90	8.44	8.99	8.23	7.22	4.10
Mean	0.39	0.36	0.34	8.41 **	11.1 **	10.9 **	10.6 **	7.67 **	7.78 **	7.82 **	8.80 ***	8.74 **	8.16 **	7.89 **	3.34*
SEM	0.03	0.04	0.01	0.42	0.23	0.35	0.39	0.37	0.14	0.01	0.26	0.13	0.04	0.39	0.38

Table 15: Changes in Insulin Concentration (ng/mL) Over Time After Administration of 50 μM Thapsigargin for 5 min; Concentration for each data set is shown in the table with mean and standard error of mean.

	Insulin Concentration (ng/mL)		
	t = 50 min	t = 52 min	t = 54 min
N_1	0.27	0.24	0.48
N_2	0.17	0.14	0.06
N_3	0.37	0.33	0.35
Average	0.27	0.24	0.44
SEM	0.06	0.06	0.04

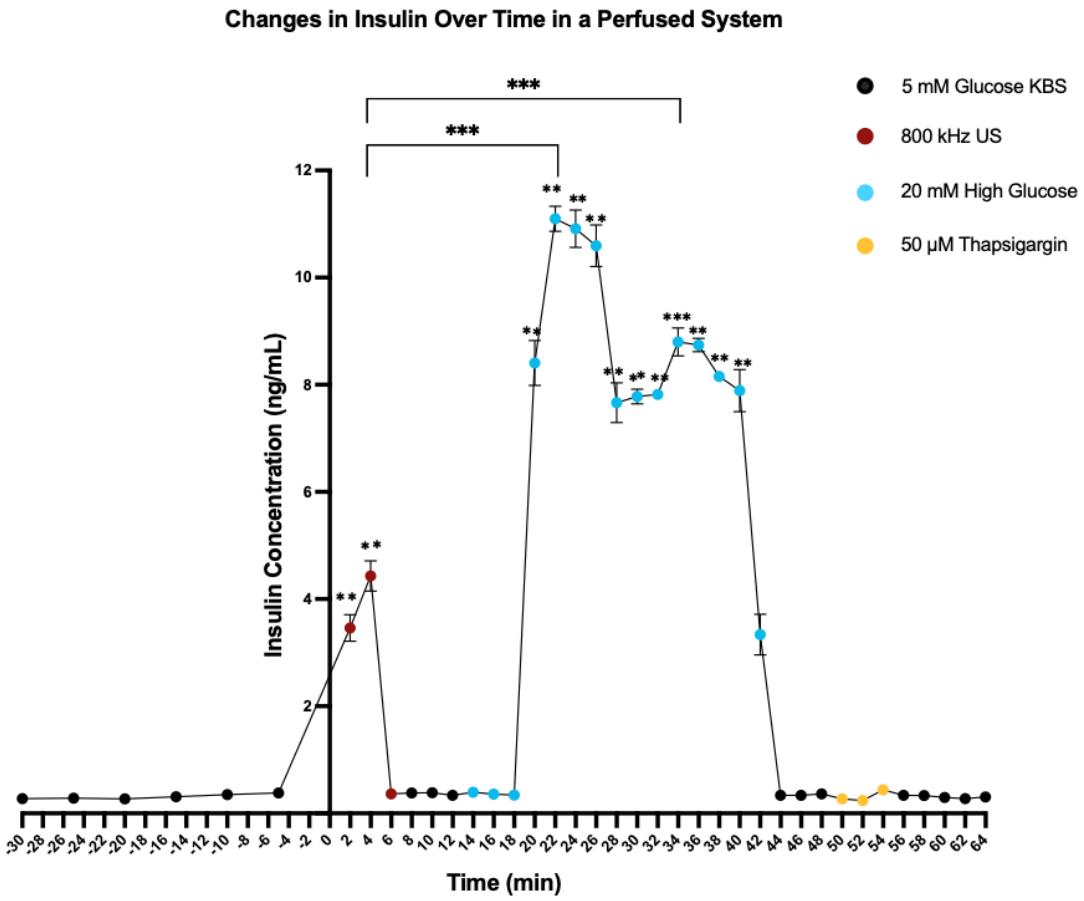

Figure 26: Changes in Insulin Concentration (ng/mL) Over Time in a Perfused System; Baseline measurements were taken 30 min prior to treatment administration, through collection of 5 mM glucose KBS. Treatments began at t = 0 min with 800 kHz ultrasound for 5 min continuously, followed by a 30 min treatment of 20 mM high glucose and a 5 min treatment of 50 µM thapsigargin. Specific treatments are differentiated by color, shown in the legend on the right. Between each treatment, system was perfused with 5 mM glucose KBS to wash out previous treatment. "**" denotes significant data with a $p < 0.01$ and "***" denotes significant data with a $p < 0.001$ ($n = 3$).

4.6 Discussion

In this study, we analyze the effects of various treatment types, low-intensity ultrasound, high glucose and thapsigargin, on the secretion of insulin from an insulinoma β-cell line in a perfused system. Perfusate was collected over time to observe the different effects in real time, with ELISA experimentation.

Our findings of insulin secretion in response to administration of low-intensity ultrasound align with previous research demonstrating the ability of this modality to

activate mechanically sensitive channels, i.e., calcium channels, across various cellular environments [108], [109]. The pivotal role of calcium influx inducing insulin release from cells is well-established [110]. Further, reports from our lab have shown that, in the context of ultrasound-mediated cellular events, it is possible to stimulate insulin release and this release requires the presence of calcium ions [73]; based on this past data from our lab, we did not specifically study the impact of calcium as it was done previously. From the data presented here, the mechanical stimulation induced by ultrasound is likely initiating the opening of calcium channels, leading to an influx of calcium ions in the β-cells within the perfusion chamber. This influx serves as a critical trigger for the exocytosis of insulin-containing vesicles, thereby facilitating the release of insulin into the extracellular fluid. Moreover, the observed co-secretion of insulin with calcium underscores the tightly regulated relationship between calcium signaling and insulin release [111]. Such coordinated secretion mechanisms ensure the efficiency and precision of insulin release, optimizing glucose homeostasis. Additionally, the potential modulation of ATP-sensitive potassium channels by ultrasound-induced mechanical stimuli warrants consideration [112]. Closure of these channels in response to elevated intracellular ATP levels, possibly induced by mechanical stimulation, further contributes to membrane depolarization and subsequent calcium influx, which could be a potential reason for this observed increase in insulin secretion we see at both 2 and 4 min.

In the context of the high glucose condition, it is important to understand the biphasic pattern of insulin release in response to increased glucose. This pattern comprises an initial rapid phase of insulin secretion, followed by a sustained second phase [113]. Several factors contribute to this biphasic response. During the first phase, which occurs

rapidly within minutes of exposure to elevated glucose levels, glucose enters pancreatic beta cells through glucose transporters [114]. This leads to an increase in intracellular ATP levels due to glucose metabolism. The rise in ATP levels triggers the closure of ATP-sensitive potassium channels, leading to membrane depolarization. Consequently, voltage-gated calcium channels open, allowing an influx of calcium ions into the beta cells. This influx of calcium ions prompts the exocytosis of insulin-containing vesicles, resulting in the rapid release of insulin. The second phase of insulin release follows the initial phase and is characterized by a sustained secretion of insulin over a more extended period, lasting from several minutes to hours [115]. This sustained release phase involves the replenishment of insulin-containing vesicles and the recruitment of additional secretory granules to maintain insulin release and regulate glucose uptake by peripheral tissues [116]. It is apparent from our data that, once the cells were exposed to a high concentration of glucose, an observed significant increase in insulin occurred rapidly, peaking at 22 minutes, followed by a decrease and sustained increase until the treatment was stopped, aligning with this biphasic pattern previously described. It is likely that the mechanism of insulin release shown under the high glucose condition follows that of which is described. However, in the context of the protocol shown here, the second phase of insulin release was not expected to be shown after ultrasound application, as the high glucose treatment was administered directly after ultrasound administration.

Interestingly, the spike in insulin release in response to ultrasound emulated that of the first phase of insulin release in the high glucose condition, suggesting that the mechanism by which ultrasound effects pancreatic β-cells is potentially similar. This fact is supported by past evidence both from our lab and other outlets, that show that low-

intensity ultrasound can induce membrane depolarization and opening of calcium-sensitive channels, leading to an influx of insulin [72], [117].

We employed thapsigargin as a positive control to investigate its impact on insulin release. Thapsigargin is recognized as an inhibitor of the sarco/endoplasmic reticulum SERCA pump, thereby disturbing calcium homeostasis and potentially leading to cell death [107]. Through its targeted inhibition, thapsigargin elevates intracellular free calcium levels by sequestering calcium from the cytosol, consequently resulting in an increase in insulin concentration [118]. Typically, researchers use relatively low concentrations of thapsigargin, such as 1 μM, to evaluate its potential to stimulate insulin release. Higher concentrations are often avoided due to the risk of inducing extreme ER stress and cytotoxicity, including cell rupture and apoptosis [119]. However, in our investigation, we observed that a notably higher concentration of 50 μM thapsigargin failed to induce such severe ER stress or cell rupture, as evidenced by the absence of any change in insulin levels. This finding is interesting, particularly considering our anticipation of a surge in insulin concentration following thapsigargin introduction into the perfusion system. This observation underscores the robustness of the cellular response to thapsigargin, suggesting that even at elevated concentrations, the cells were resilient to the extreme ER stress and cytotoxic events typically associated with thapsigargin exposure. However, based on these observations, it is evident that thapsigargin did not act as a positive control, i.e. induce insulin release. This could have potentially been due to the sensitivity of the cell line used, where the cells could have an inherent resistance to this compound, or require even higher concentrations to cause effective inhibition of the SERCA pump [120]. Further, it is possible that off-target effects could have occurred as a result of the introduction of

thapsigargin to the system, modulating other signaling pathways unrelated to ER stress [121].

4.7 Conclusion

Here, we have demonstrated that ultrasound, when applied at parameters of 800 kHz with an intensity of 0.5 W/cm^2 for 5 minutes continuously, is capable of significantly increasing insulin secretion from an insulinoma β-cell line. This finding not only corroborates previous research but also underscores the potential of ultrasound as a modality for stimulating secretory events relevant to addressing key pathophysiologies associated with diabetes. Importantly, our observation of a substantial increase in insulin levels in response to high glucose conditions, exhibiting a biphasic pattern of insulin release, adds depth to our understanding of pancreatic β-cell function. Remarkably, the insulin release pattern induced by ultrasound closely mirrors the initial phase of insulin release seen under high glucose conditions, suggesting a similarity in the mechanisms involved. This observation highlights the potential of ultrasound to mimic physiological responses associated with glucose metabolism and insulin secretion, offering promise as a novel approach for managing diabetes. Moving forward, further exploration of the mechanistic underpinnings of ultrasound-induced insulin release is warranted to elucidate its therapeutic potential in the treatment of diabetes mellitus.

4.7.1 Follow Up Studies

Optimization of this perfusion system is continually being completed, to improve on some of the shortcomings associated, such as lowering the frequency of leakage of perfusate out of the chamber. Potential alterations to this system would include varying the amount of grease used to seal the chamber, as well as experimenting with different types

of chambers available in our lab. Future studies will continue to analyze how insulin responds to these different treatments, but additional analysis will be done on the hormone, amylin, to observe whether ultrasound, high glucose and thapsigargin can induce an increase in the secretion of this pancreatic hormone. Such exploration will provide more evidence regarding the efficacy of this modality in inducing hormonal regulation.

Chapter 5: Analysis of Ultrasound-Mediated Effects on Protein Secretion in a Sliced Rat Pancreas Model

5.1 Methods

5.1.1 Rat Pancreas Acquisition

Female rat pancreases were harvested from available animals provided by Professor Matt Kay's Laboratory at The George Washington University. The pancreases were obtained immediately after sacrifice done for their ongoing cardiac studies. These animals were derived from the Sprague Dawley strain from Hilltop Lab Animals, Inc. (Scottdale, PA). The first seven animals came from 3 separate groups, the first of which received no chronic intermittent hypoxia (CIH) and received a high fat diet (HFD), the second receiving a regular diet with no CIH, and a third that received a HFD and CIH. The various manipulations prior to sacrifice relevant to our studies of these animals are shown in *Table 16*. It is important to note that at 5 weeks, the rats received an injection of oxytocin-cre promoter to the paraventricular nucleus (PVN), which was done in conjunction with DREADDS to target a specific area of the brain to induce production of oxytocin—this is expected to have no effect on the pancreas samples that we harvested. Baseline measurements of cardiac ultrasound (i.e., 2% isoflurane exposure for 20 min), glucose tolerance test (6 hr fasting prior to the procedure), and whole-body plethysmography recording were taken, followed by final *in vivo* measurements of the same parameters taken before sacrifice. Whole body plethysmography tests are related to respiratory parameters, such as tidal volume, minute ventilation, and respiratory rate, used to evaluate respiratory

mechanics, providing valuable insight into therapeutic evaluations; as such, this test has no effect on pancreas functionality [122]. The final three pancreases we used for experimentation received a transverse aortic constriction surgery as neonates to induce chronic pressure overload in studying left ventricular hypertrophy and cardiac failure [123]. There is evidence that supports that chronic heart failure can lead to pancreatic exocrine insufficiency; however, these findings are currently inconclusive [124]. For example, a study done by Riehle et al. examined whether heart failure could contribute to pancreatic β-cell insufficiency and found that, in conjunction with induced heart failure, a mutation in the insulin encoding gene *Insulin2* exasperated these effects, indicating that other factors may be more explanatory of contributing to pancreatic dysfunction [125]. Pancreas samples were excised directly from the animal and minced into 2 sections (approximately 1 mm wide) before being placed in Kreb's ringer buffer solution (KBS). Following sample acquisition, we collected 200 μL of extracellular medium in a 0.6 mL graduated tube to serve as our internal control (t = 0 min), to assess the impact of ultrasound on the different hormones.

Table 16: Manipulations of Rats Before Pancreas Acquisition; Manipulations were done at different periods of life for the rat donors. All rats were from the Sprague Dawley Strain and were female, with an age of 55 weeks at sacrifice.

Age at Manipulation	Manipulation	Drugs Received OR Diet Changes
5 weeks	Injection of oxytocin-cre promoter into paraventricular nucleus (PVN) or hypothalamus	
13 Weeks	Ovariectomy	Buprenorphine, meloxicam
14 Weeks-46 Weeks	High Fat Diet	26% Fructose, 1.5% NaCl Adjusted Calories (42/fat) + Sugar Water (20% Fructose Water)
45 Weeks-55 Weeks	Chronic Intermittent Hypoxia	6 min cycles of 21% O_2, 79% N_2 to 6% O_2, 94% N_2 for 8 hr/day during sleep

5.1.2 Ultrasound Administration

Ultrasound treatments were applied to the wells containing the minced pancreas samples immediately after sample acquisition and collection of the internal control. Samples were placed in 3 mL of KBS solution. The parameters used were 800 kHz frequency with an intensity of 1 W/cm^2 for a duration of 5 min continuously. These parameters were chosen as past studies have shown that they are sufficient in stimulating insulin release from *ex vivo* rat pancreases [75]. An amplifier (AR, Souderton, PA), connected to an Agilent waveform generator (Santa Clara, CA), was used to administer the input voltage. To channel the input voltage, an impedance matching network was attached to the power supply and the corresponding ultrasound transducer. The ultrasound transducer was oriented beneath the 6-well plate in a water bath held at 37ºC, 2.5 cm below the surface. Following ultrasound administration, 200 μL of extracellular medium was

collected in a 0.6 mL graduated tube, denoted as time point t = 5 min, and an additional 200 μL of extracellular medium was collected 30 min after administration, serving as t = 35 min. These time points were utilized to investigate the immediate (fast, at t = 5 min) and delayed (slow, t = 35 min) effects of ultrasound exposure on insulin, glucagon, and alpha-amylase secretion.

5.1.3 Sandwich ELISA

All ELISA protocols are based on the sandwich ELISA method previously described Chapter 4.

5.1.4 Rat/Mouse Insulin ELISA

A rat/mouse insulin ELISA kit (MilliporeSigma, Burlington, MA) was used to assess whether ultrasound administration was capable of inducing insulin release in the rat pancreas model. All provided reagents were brought to room temperature before starting the assay, and he 10X Wash Buffer concentrate was diluted 10 fold through mixing the 45 mL Wash Buffer with 450 mL of deionized water. The 96-well microtiter plate was then washed three times with 350 μL of the diluted Wash Buffer, followed by tapping of the plate on an absorbent pad between each wash to ensure the residual solution was removed. This process ensures the complete removal of the wash buffer; however, it will be important to not allow the wells to dry out completely, as dried wells can cause non-specific binding of analytes or loss of reagent activity [126]. All blank, standard, and samples were plated in duplicate on the plate. 10 μL of Assay Buffer was added into the pre-determined bank and sample wells and 10 μL of the provided Rat Insulin Standards were added to the appropriate wells in ascending concentration. Following this, 10 μL of the quality control 1 and 2 (QC 1, QC2) were added, and the samples were plated in duplicate sequentially

across the plate. Standard solutions were pipetted in duplicate within the initial two rows and subsequent samples in duplicate starting from the third row. A systematic pipetting protocol was employed, where each 0-minute sample was pipetted in duplicate, followed by samples taken at 5-minute and 35-minute intervals for each pancreas slice. Sequential pipetting was conducted for slices originating from the same pancreas, with the final slice allocated to the remaining six wells of the plate.

80 μL of Detection Antibody was then dispensed into all wells on the microtiter plate. Once this was completed, the plate was covered with a plate sealer and allowed to incubate at room temperature for two hours on an orbital microtiter plate shaker set to 450 rpm. After the 2 hours, the contents of the plate were removed through tapping onto the absorbent towel and 3 washes with diluted Wash Buffer were completed using 300 μL per wash. 100 μL of enzyme solution was then added to all wells and the plate was covered and placed on the shaker for an additional 30 min incubation time at room temperature. The plate was tapped again on the absorbent towel to remove the contents and washed an additional 6 times using the method previously described. We then added 100 μL of substrate solution to each well, and the plate was placed on the orbital shaker for an additional 5-20 min. The specific incubation time is determined by observing when all wells turn a blue color, indicating the presence of insulin. Once the wells turned blue, 100 μL of stop solution was added to each well, causing the solution to turn yellow, and the plate was then placed in the SpectraMax iD5 (Molecular Devices, San Jose, CA) plate reader to read absorbance values at 450 nm and 590 nm. Once this data was obtained, the absorbance values for each sample at 590 nm was subtracted from the absorbance values

for 450 nm, then these values were averaged to determine the mean absorbance for each condition.

The insulin concentration was determined by creating a standard calibration curve in Microsoft Excel. The mean absorbance value for each insulin standard was plotted on the y-axis and the corresponding concentration was plotted on the x-axis. The standard curve generated from the data for the first six pancreases can be seen in *Figure 27*. A line of best fit was added to interpolate the insulin concentrations in the samples using the mean absorbance values for each sample. The average mean absorbance for each sample was input as the x variable, and we solved for y to determine the concentration, using the equation generated from the line of best fit.

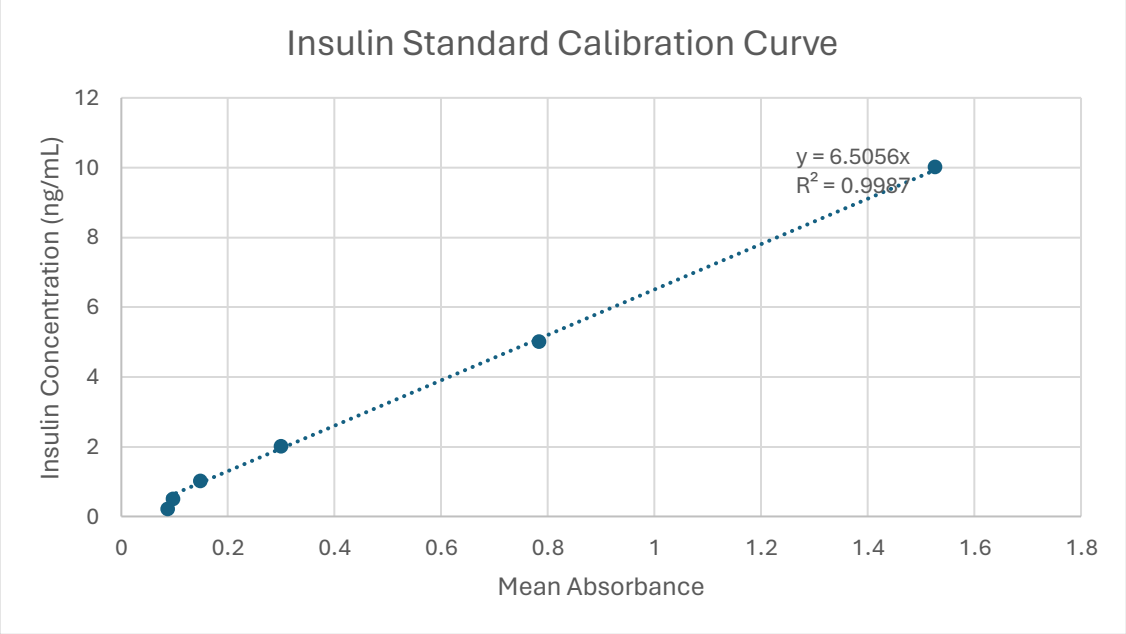

Figure 27: Insulin Standard Calibration Curve; mean absorbance for each standard was plotted on the x-axis, with the corresponding insulin concentration for the standards was plotted on the y-axis in ng/mL. A line of best fit to interpolate the insulin concentration for each sample and R^2 value to assess the goodness of fit for the line was added to the curve.

Fold change for each time point was then calculated by dividing each insulin concentration by the concentration output for t = 0 min, and these values were averaged

for each slice to determine the fold change for each pancreas sample. A fold change of greater than 1 indicated an upregulation in insulin, whereas a fold change of less than 1 corresponded to a downregulation of this hormone.

5.1.5 Rat/Mouse Glucagon ELISA

A rat/mouse Glucagon ELISA kit (Crystal Chem, Elk Grove Village, IL) was used to determine the effects of ultrasound administration on glucagon secretions in the rat pancreases. This kit works through the use of two monoclonal antibodies to glucagon with <1% cross-reactivity to GLP-1, GLP-2, mini-glucagon, and pro-glucagon peptides glicentin and oxyntomodulin. After arrival, the kit was stored in a fridge at 4°C until rat pancreas samples were ready to use. The contents of the kit can be found in *Table 17*.

Table 17: Contents of Rat/Mouse Glucagon ELISA kit; Standards and wash buffer required preparation before starting the experiment, following the protocol provided.

Label	Description	Amount
MIC	Antibody-coated Microplate (96 wells)	1 pack
STD	Standard	1 vial
HRP	HRP-labeled Antibody	1 x 12 mL
SUB	Substrate Solution	1 x 12 mL
STOP	Stop Solution	1 x 12 mL
BUF	Buffer Solution	1 x 12 mL
WASH	Washing Solution (20X concentrated)	1 x 50 mL
SEAL	Adhesive Seal	2 sheets

All reagents (i.e. HRP-labeled antibody, substrate solution, stop solution, buffer solution) were provided as ready to use, except the standards and wash buffer, which required preparation before the assay procedure. To prepare the wash buffer, 50 mL of wash

buffer was diluted with 950 mL of deionized water, to achieve a 1:20 working dilution. The standards were prepared by reconstituting standard (1 ng/vial) with 1 mL of Buffer Solution to create a 1,000 pg/mL working standard. 200 µL of Buffer Solution was then pipetted into seven microtubes, with labels 500, 250, 125, 62.5, 31.25, 15.63, and 7.81 pg/mL. 200 µL of the 1,000 pg/mL working standard was then dispensed into the 500 pg/mL microtube. We then pipetted 200 µL of the 500 pg/mL standard into the 250 pg/mL tube and repeated this process for the remaining standards, to create the working standards necessary to run the ELISA.

To start the assay procedure, 350 µL of Wash Buffer was added to each well on the 96-well microplate and aspirated out, with this washing step repeated two more times. 10 µL of sample or standard was added in duplicate to the predetermined wells, followed by addition of 100 µL of HRP-labeled antibody and the plate was sealed and allowed to incubate at 18-20 hours in a fridge at 4°C. The same plate set-up was used as previously described in the insulin ELISA protocol. After the incubation time was completed, the seal was removed and the plate was washed six times with 350 µL of Wash Buffer. After washing, 100 µL of Substrate Solution was added to each well and the plate was allowed to incubate for 30 min at room temperature in the dark without shaking. To ensure complete darkness, we wrapped the microplate with aluminum foil. After the 30 min, 100 µL of Stop Solution was added to all the wells and the absorbance was measured at 450 nm and 630 nm, using a SpectraMax iD5 (Molecular Devices, San Jose, CA). Once this data was obtained, the absorbance values for each sample at 630 nm was subtracted from the absorbance values for 450 nm, then these values were averaged to determine the mean absorbance for each condition.

The glucagon concentration for each sample was determined by creating a standard calibration curve in Microsoft Excel. This was done by plotting the mean absorbance values for each standard on the y-axis vs. the corresponding glucagon concentration. The standard curve generated from the data for the first six pancreases can be seen in *Figure 28*. Once the standard curve was generated, a line of best fit was added to interpolate the glucagon concentrations in the samples using the mean absorbance values for each sample. This was done using the same method as previously described for determining insulin concentration.

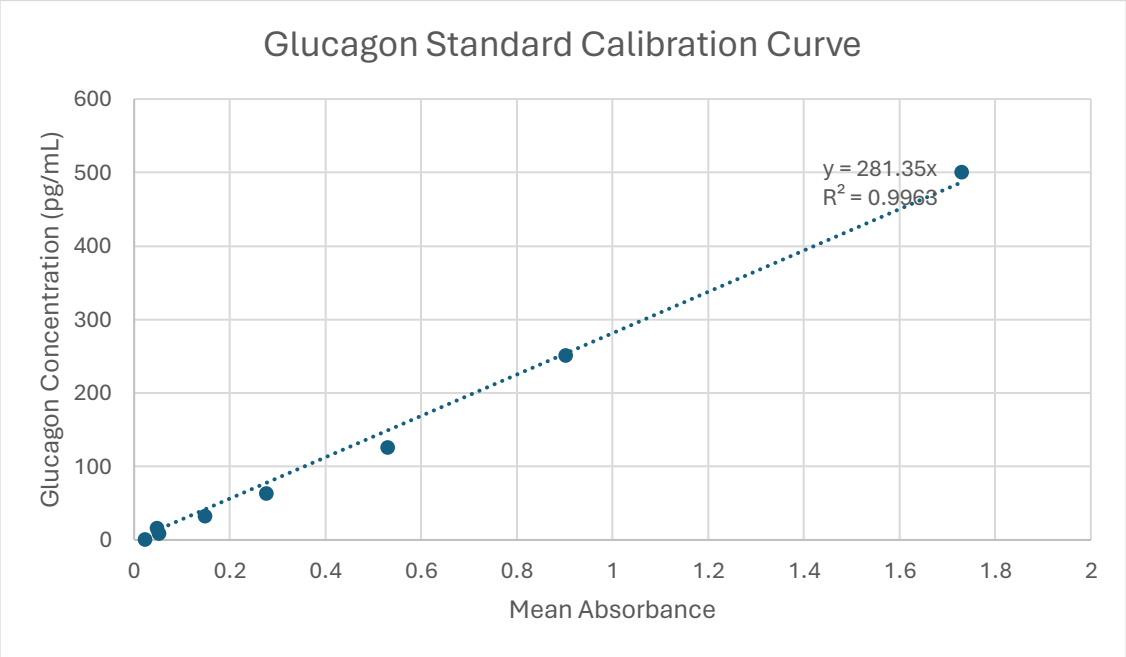

Figure 28: Glucagon Standard Calibration Curve; mean absorbance for each standard was plotted on the x-axis, with the corresponding glucagon concentration for the standards was plotted on the y-axis in pg/mL. A line of best fit to interpolate the glucagon concentration for each sample and R^2 value to assess the goodness of fit for the line was added to the curve.

Fold change for each time point was then calculated by dividing each glucagon concentration by the concentration output for t = 0 min, and these values were averaged for each slice to determine the fold change for each pancreas sample. A fold change of greater than 1 indicated an upregulation in glucagon, whereas a fold change of less than 1 corresponded to a downregulation of this hormone.

5.1.6 Rat/Mouse Alpha-Amylase ELISA

A rat/mouse alpha-amylase ELISA kit (LSBio, Shirley MA) was used to quantify the concentration of this hormone after ultrasound administration. Prior to beginning the assay, the wash buffer was prepared by diluting the provided 10 mL of 100x Wash Buffer Concentrate with 990 mL of deionized water. Following this, 50 µL of standard or sample was added to the corresponding wells. Standard solutions were pipetted in duplicate within the initial two rows and subsequent samples in duplicate starting from the bottom of the second row. A systematic pipetting protocol was employed, where each 0-minute sample was pipetted in duplicate, followed by samples taken at 5-minute and 35-minute intervals for each pancreas slice. Sequential pipetting was conducted for slices originating from the same pancreas, until all samples were plated.

100 µL of HRP-conjugate was then added to each well, excluding the blank well, and the plate was covered with the provided sealer and incubated for 1 hour in at 37 °C. After the hour, the liquid in each well was aspirated out and the plate was washed five times by adding 350 µL of 1x Wash Buffer to each well. 50 µL of Substrate A and 50 µL of Substrate B was then be added to each well, including the blank, and gently agitated to ensure a homogenous mixture. Once the substrate solutions were added, the plate was incubated in the dark for 15-20 min at 37 °C. After this time, 50 µL of Stop Solution was added to each well following the same pattern and timing as each substrate solution was added, to stop the reaction. The plate was then placed in a SpectraMax iD5 (Molecular Devices, San Jose, CA) microplate reader set to 450 nm to read the absorbance values for each well immediately following the addition of the Stop Solution.

To determine the results, the duplicate readings were averaged for each standard, control and sample, then subtracted from the average zero standard optical density (i.e. Standard A). An alpha-amylase standard calibration curve was generated using Microsoft Excel, plotting the mean absorbance values after the subtraction for each standard on the x-axis, and the concentration on the y-axis. The standard curve generated from the data for the first six pancreases can be seen in *Figure 29*. Once the standard curve was generated, a line of best fit was added to interpolate the alpha-amylase concentrations in the samples using the mean absorbance values for each sample. This was done using the same method as previously described for determining insulin concentration.

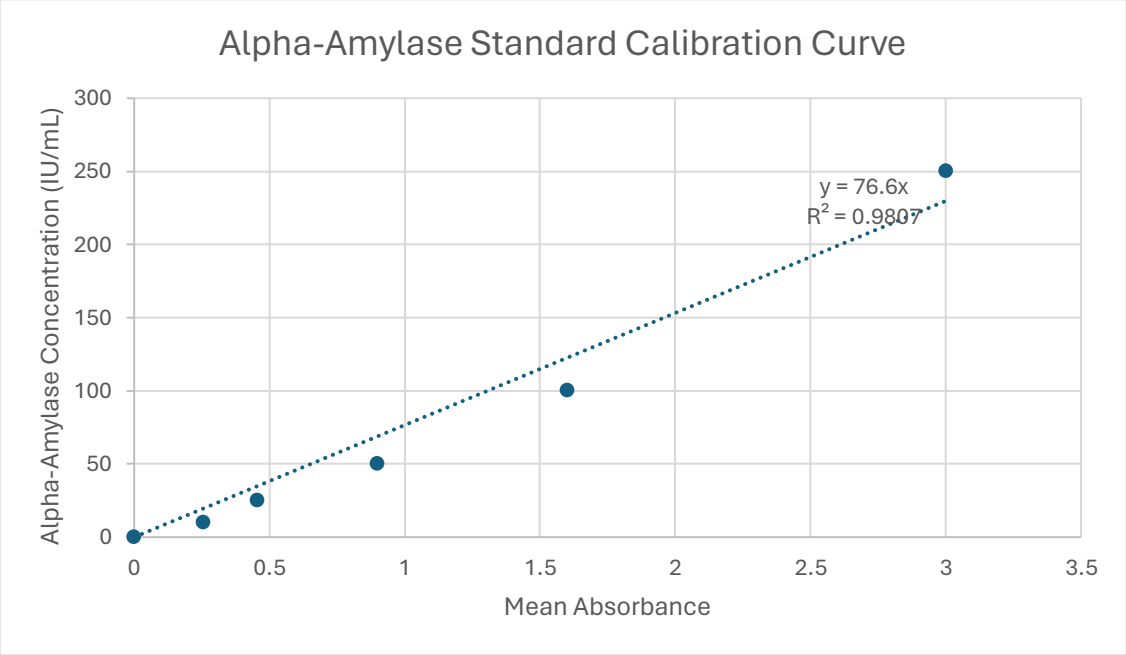

Figure 29: Alpha-Amylase Standard Calibration Curve; mean absorbance for each standard was plotted on the x-axis, with the corresponding alpha-amylase concentration for the standards was plotted on the y-axis in IU/mL. A line of best fit to interpolate the alpha-amylase concentration for each sample and R^2 value to assess the goodness of fit for the line was added to the curve.

Fold change for each time point was then calculated by dividing each alpha-amylase concentration by the concentration output for t = 0 min, and these values were

averaged for each slice to determine the fold change for each pancreas sample. A fold change of greater than 1 indicated an upregulation in alpha-amylase, whereas a fold change of less than 1 corresponded to a downregulation of this hormone.

5.1.7 Statistical Analysis

Statistical analysis was done using a two-tailed, unpaired Welch's t test, utilizing GraphPad Prism 10.1.1 (GraphPad Software, Inc., La Jolla, CA). This test was chosen as we were interested in determining whether a significant difference existed between the average of 5 min or 35 min compared to the internal control in either direction, without assuming an equal variance. Standard deviation and mean values were calculated using the descriptive statistics function available in the column analyses available in GraphPad. All figures related to the data were generated by GraphPad.

5.2 Results

Analysis of ELISA data was done by determining the fold change of insulin, glucagon, and alpha-amylase and comparing it to the internal control as previously described. A fold change exceeding 1 suggested a potential upregulation of these hormones post-ultrasound intervention, whereas a fold change below 1 indicated downregulation. Average fold change values from individual pancreatic slices were computed to determine the collective impact across each experimental condition.

5.2.1 Rat/Mouse Insulin ELISA

Following the application of continuous ultrasound for a duration of 5 min at a frequency of 800 kHz and an intensity of 1 W/cm^2, observations indicated a slight upregulation in the average fold change (FC) of insulin levels at both t = 5 min and t = 35 min. Specifically, at t = 5 min, the fold change was measured at 1.19, while at t = 35 min,

it was observed to be 1.05. It is noteworthy that the response at t = 35 min appeared diminished compared to the earlier time point. However, statistical analysis revealed that these results did not achieve significance. Relevant data for each individual pancreas sample, as well as standard deviation and p-value are shown in *Table 18*. A graphical representation depicting these changes is shown in *Figure 30*.

Table 18: Insulin Fold Change Data Post-Ultrasound Treatment; t = 0 min served as an internal control with collection prior to ultrasound treatment. Data for t = 5 min and t = 35 min was compared to t = 0 min to assess the impact of ultrasound treatment on the rat pancreases. Average fold change, standard deviation, and p-value is shown at bottom of the table to determine conclusions.

	t = 0 min	t = 5 min	t = 35 min
N_1	1.00	0.80	0.78
N_2	1.00	1.12	0.97
N_3	1.00	0.85	0.76
N_4	1.00	1.47	1.54
N_5	1.00	0.67	0.94
N_6	1.00	1.69	0.88
N_7	1.00	2.17	1.55
N_8	1.00	1.06	0.98
N_9	1.00	1.16	1.12
N_{10}	1.00	0.97	1.03
Average Fold Change		1.19	1.05
Standard Deviation		0.46	0.28
p-value		0.21	0.56

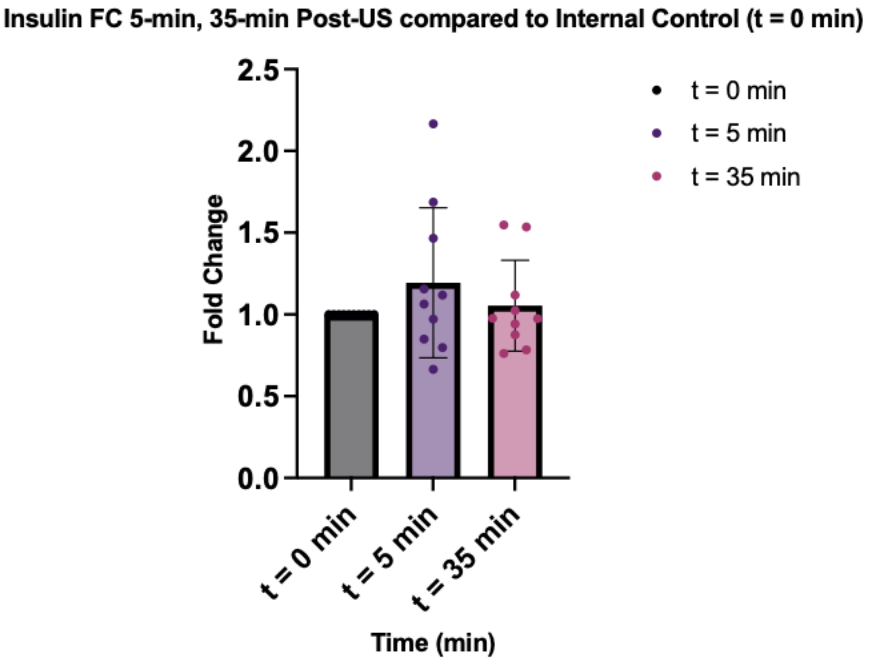

Figure 30: Insulin Fold Change 5 min, 35 min Post-Ultrasound Treatment Compared to t = 0 min; Fold Change is plotted on the y-axis compared to each time point, plotted on the x-axis. Individual data points for each rat pancreas are shown as dots.

5.2.2 Rat/Mouse Glucagon ELISA

The glucagon ELISA analysis yielded an average fold change of 0.91 at t = 5 min and 0.76 at t = 35 min, indicating a notable reduction in hormone levels following ultrasound exposure under these conditions. Further, the finding of a fold change of 0.76 at t = 35 min was deemed significant, indicating that ultrasound significantly downregulated glucagon at this time point. Comprehensive data for each pancreatic sample, with standard deviation and p-values, are shown in *Table 19*, with corresponding graphical depiction provided in *Figure 31* to elucidate these changes.

Table 19: Glucagon Fold Change Data Post-Ultrasound Treatment; t = 0 min served as an internal control with collection prior to ultrasound treatment. Data for t = 5 min and t = 35 min was compared to t = 0 min to assess the impact of ultrasound treatment on the rat pancreases. Average fold change, standard deviation, and p-value is shown at bottom of the table to determine conclusions. "*" denotes significant data ($p < 0.05$).

	t = 0 min	t = 5 min	t = 35 min
N_1	1.00	0.90	0.54
N_2	1.00	0.93	0.53
N_3	1.00	1.10	0.51
N_4	1.00	0.63	0.43
N_5	1.00	1.08	0.86
N_6	1.00	0.66	0.44
N_7	1.00	0.92	1.09
N_8	1.00	0.73	1.04
N_9	1.00	0.62	0.76
N_{10}	1.00	1.49	1.35
Average Fold Change		0.91	0.76
Standard Deviation		0.27	0.32
p-value		0.30	0.04*

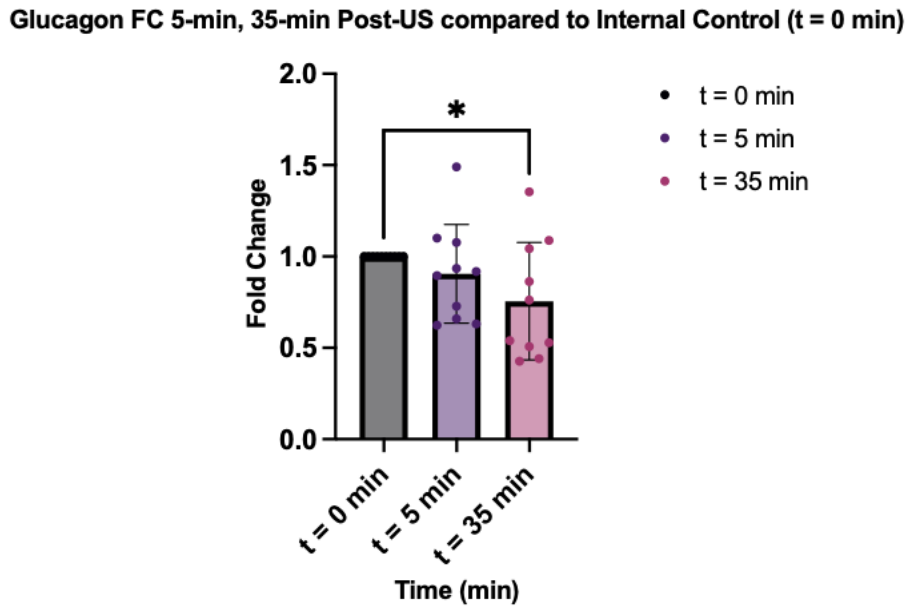

Figure 31: Glucagon Fold Change 5 min, 35 min Post-Ultrasound Treatment Compared to t = 0 min; Fold Change is plotted on the y-axis compared to each time point, plotted on the x-axis. Individual data points for each rat pancreas are shown as dots. "*" corresponds to significant findings ($p < 0.05$).

5.2.3 Rat/Mouse Alpha-Amylase ELISA

It was found that with ultrasound administration, the alpha-amylase concentration of the rat pancreases was upregulated at both t = 5 min and t = 35 min, with an average fold change of 1.20 and 1.13, respectively, when compared to the internal control. It is worth noting that the alpha-amylase level seemingly was less upregulated at 35 min compared to 5 min. However, these findings did not achieve significance. Comprehensive information regarding each individual pancreas sample, including fold change data, mean and standard deviation, are shown in *Table 20*. Refer to *Figure 32* for graphical representation to visualize this data.

Table 20: Alpha-Amylase Fold Change Data Post-Ultrasound Treatment; t = 0 min served as an internal control with collection prior to ultrasound treatment. Data for t = 5 min and t = 35 min was compared to t = 0 min to assess the impact of ultrasound treatment on the rat pancreases. Average fold change, standard deviation, and p-value is shown at bottom of the table to determine conclusions.

	t = 0 min	t = 5 min	t = 35 min
N_1	1.00	1.08	1.31
N_2	1.00	1.00	0.72
N_3	1.00	1.23	1.36
N_4	1.00	1.06	0.61
N_5	1.00	1.27	1.20
N_6	1.00	0.91	0.88
N_7	1.00	1.09	1.12
N_8	1.00	2.37	2.05
N_9	1.00	1.04	1.04
N_{10}	1.00	0.98	1.00
Average Fold Change		1.20	1.13
Standard Deviation		0.42	0.40
p-value		0.16	0.34

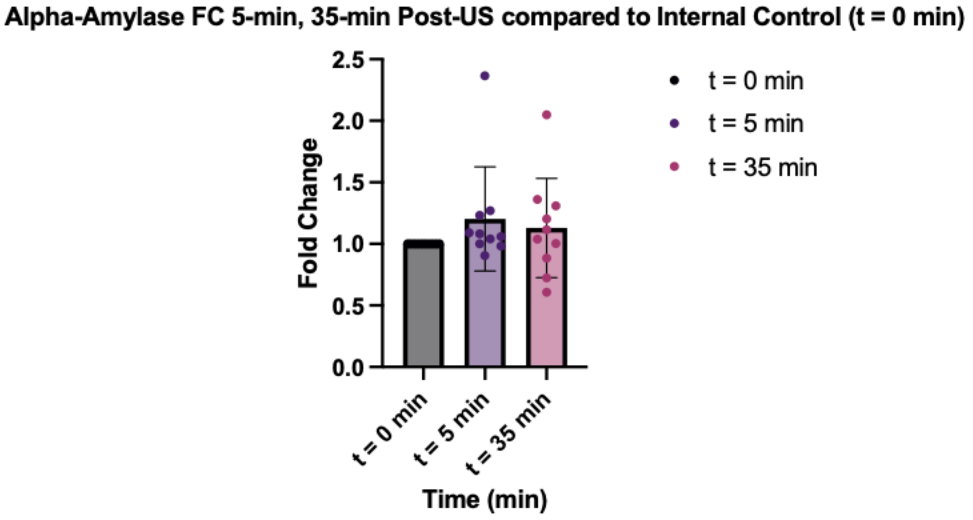

Figure 32: Alpha-Amylase Fold Change 5 min, 35 min Post-Ultrasound Treatment Compared to t = 0 min; Fold Change is plotted on the y-axis compared to each time point, plotted on the x-axis. Individual data points for each rat pancreas are shown as dots.

5.3 Discussion

We investigated the effects of low-intensity, therapeutic ultrasound on protein concentration in a sliced pancreas model, focusing on key pancreatic proteins: insulin, glucagon, and alpha-amylase. Our findings provide insights into the potential impact of ultrasound on pancreatic hormone and enzyme levels, which could have implications for therapeutic interventions targeting pancreatic disorders.

The observed slight upregulation in insulin levels at both t = 5 min and t = 35 min following ultrasound exposure is consistent with findings from previous studies [127]. Ultrasound has been shown to enhance cellular uptake of insulin *in vitro* through various mechanisms, including increased membrane permeability and activation of insulin signaling pathways [127], [128]. At t = 35 min, a slightly diminished response in insulin secretion was detected, which could be attributed to the transient nature of ultrasound-mediated effects or potential desensitization of the pancreatic β-cells over time [129].

Additionally, the lack of statistical significance could have been due to the relatively small sample size or inherent biological variability (i.e. age at sacrifice, diet, sample-handling, sample preparation) [130].

The reduction in glucagon levels post-ultrasound exposure aligns with reports suggesting that ultrasound can modulate hormone secretion in pancreatic alpha cells [131]. Ultrasound may affect glucagon secretion through alterations in intracellular calcium signaling or disruption of cellular membrane integrity [131]. The finding of significance at t = 35 min underscores the importance of exploring the temporal dynamics of hormone responses to ultrasound and highlights the need for further investigation into the precise mechanisms underlying glucagon regulation by ultrasound. For example, ultrasound-mediated increases in intracellular calcium levels that in turn increase β-cell secretion of insulin has been shown to inhibit glucagon release from alpha cells through modulation of ion channel activity [132]. Increased insulin concentrations will activate the PI3K signaling pathway, which modifies ATP-sensitive potassium channels, thus depolarizing alpha cells to membrane potential, inhibiting glucagon secretion. Interestingly, the perceived upregulation of alpha-amylase levels in response to ultrasound administration is inconsistent with studies demonstrating the suppressive effects of ultrasound on pancreatic enzyme secretion [133], [134]. Ultrasound-induced changes in enzyme activity may result from alterations in pancreatic blood flow, intracellular calcium levels, or direct effects on enzyme synthesis and release [135]. Further, this unexpected upregulation could have been caused by the heart failure induced samples, as this could have contributed to exocrine pancreatic insufficiency [124]. Yet, the observed temporal variation in alpha-amylase upregulation between t = 5 min and t = 35 min suggests complex kinetics of ultrasound-

mediated enzyme modulation, which warrant further investigation, especially as these values approach significance.

Our experiment aimed to replicate the outcomes of a study by Suarez-Castellanos et al., which utilized *ex vivo* human pancreatic islets and rabbit pancreases [75]. In their investigation, ultrasound of 800 kHz frequency and 0.5-1 W/cm^2 intensity was administered for 5 minutes, followed by the collection of extracellular fluid samples at different time points. Initially, insulin release showed a significant increase at t = 5 min, but this effect attenuated after 30 minutes. Although glucagon release exhibited a transient rise post-treatment, it did not significantly differ from the control group. Alpha-amylase release remained unaffected by ultrasound treatment. Comparatively, our findings align with the insulin trend observed in Suarez-Castellanos et al.'s study, demonstrating an immediate elevation followed by a less pronounced effect at t = 35 min, albeit without achieving statistical significance. Interestingly, our results diverged from the glucagon response seen in the prior study; ultrasound induced a decrease in glucagon levels immediately after treatment, with a further reduction at t = 35 min. Notably, this decline at t = 35 min trended achieved significance. Differentially, Suarez-Castellanos et al. noted a decrease in alpha-amylase concentration, possibly attributed to hormonal reuptake mechanisms, whereas we observed an increase in this hormone [136], [137], [138]. One major difference between the aforementioned study and the data shown here is that Suarez-Castellanos et al. utilized a sham-treated group as a comparison for hormonal changes post-ultrasound, whereas we made use of an internal control. With a sham-treated group for comparison, one is able to distinguish between genuine physiological responses to a given stimulus, instead of confounding factors that could be the root cause.

Several factors could contribute to the lack of significant effects of ultrasound on the rat pancreas model described here. Firstly, the ultrasound parameters utilized in the study may not have been optimized for targeting pancreatic physiology. Research suggests that variations in parameters such as frequency and intensity can significantly influence tissue response to ultrasound [139]. Although the chosen parameters have shown significant results in the past [40], [72], [73], they still may not be tailored to the specific characteristics of rat pancreatic tissue, such as its size and vascularization, which could result in insufficient stimulation to induce detectable changes in insulin, glucagon, or alpha-amylase release at the given time points. Additionally, the temporal dynamics of ultrasound exposure may not have aligned with the peak activity or duration of action of these pancreatic hormones. Studies have shown that biological responses to ultrasound can be transient and time-dependent, with the timing of exposure critical for eliciting desired effects [140]. The duration and timing of ultrasound application utilized here may not have coincided with the physiological processes governing hormone secretion in a rat pancreas, which could potentially mask any significant alterations. Furthermore, inter-species variability in ultrasound sensitivity and response could play a significant role. Rats and humans differ in terms of tissue composition, metabolic regulation, and receptor expression, which can influence their responses to ultrasound [141]. Differences in the anatomy and physiology of the rat pancreas compared to humans may result in unique responses to ultrasound stimulation. Moreover, inadequate sample size and statistical power might have hindered the ability to detect subtle changes in pancreatic hormone release. Studies with small sample sizes are more susceptible to Type II errors, where true effects go undetected due to insufficient power [142]. If the study lacked a sufficiently large

sample size to detect subtle changes in insulin, glucagon, or alpha-amylase release, it could result in non-significant findings despite biologically meaningful effects. Addressing these factors in future research, with careful consideration of ultrasound parameters, temporal dynamics, inter-species differences, and sample size, could provide deeper insights into the effects of ultrasound on pancreatic tissue and hormone secretion.

5.4 Conclusions

Based on the results of these studies, the proposed ultrasound parameters do not appear to significantly affect the protein secretion of insulin, or alpha-amylase. While we observed trends suggestive of upregulation in insulin levels and downregulation in alpha-amylase levels following ultrasound exposure, statistical significance was not achieved. However, it was found that ultrasound exposure did have a significant impact on glucagon secretion at t = 35 min, suggesting that this modality can downregulate this hormone over time. These findings underscore the complexity of ultrasound-mediated modulation of pancreatic physiology and highlight the need for further investigation into optimal ultrasound parameters, temporal dynamics, and inter-species differences. Additionally, our comparison with a previous study emphasizes the importance of experimental design, including the use of sham-treated groups, to distinguish genuine physiological responses from confounding factors. Addressing these considerations could pave the way for more targeted and effective therapeutic interventions for pancreatic disorders.

5.4.1 Follow-Up Studies

As additional rat pancreases become available, our research will incorporate sham-treated groups, wherein we measure the hormone levels in excised rat pancreases without ultrasound exposure, following the same time points outlined previously. By analyzing the

sham data, we can establish statistical comparisons with the findings presented in this study and those of subsequent investigations. Moreover, we will continue to gather additional sample data to determine if the observed trend of glucagon downregulation at t = 35 minutes attains statistical significance. With more data points, we hope to be able to draw more concrete conclusions as to whether ultrasound administration can indeed induce hormonal secretion.

Chapter 6: Histological Analysis and Safety Testing of Ultrasound Frequencies on Rat Pancreas Tissue

6.1 Methods

6.1.1 H&E Staining

Harvested rat pancreas samples were excised from the donor animal and minced in to 2 sections. One section served as a sham-treated group, and was immediately placed in paraformaldehyde (PFA). The other section was placed in 3 mL of KBS and underwent ultrasound treatment for 5 min continuously, at a frequency of 800 kHz with an intensity of 0.5 W/cm^2. After the ultrasound was applied, these samples were placed in PFA. In total, we used 3 sham-treated and 3 ultrasound-treated pancreas samples for histological analysis. Once placed in PFA, the samples were labeled and packed to be sent to Histoserv Inc. (Germantown, MD) for histological analysis. While there, the samples underwent hematoxylin and eosin staining (H&E staining), to assess any morphological changes that may have occurred after ultrasound application. This involved staining the nucleus of the cell with hematoxylin and the cytoplasm with eosin, allowing for perception of any abnormalities or irregularities that may be present [143]. Once the staining was complete, the samples were sent back to our lab and read under a microscope at 10x, and 40x, with images being taken to view these morphological changes.

6.2 Results

Based on the H&E staining results, there appear to be no discernible changes in the US-treated pancreases vs. the sham-treated pancreas. This is evidenced by the tissue in the

US-treated pancreases showing no loss of nuclei or damage to different structures in comparison to the sham images, with observed similarities in the structure and composition of the matrix between each group. These results are shown further in *Figure 33*, where each sham-treated sample is shown on the left at both 10x and 40x, compared to the ultrasound-treated section on the right at 10x and 40x.

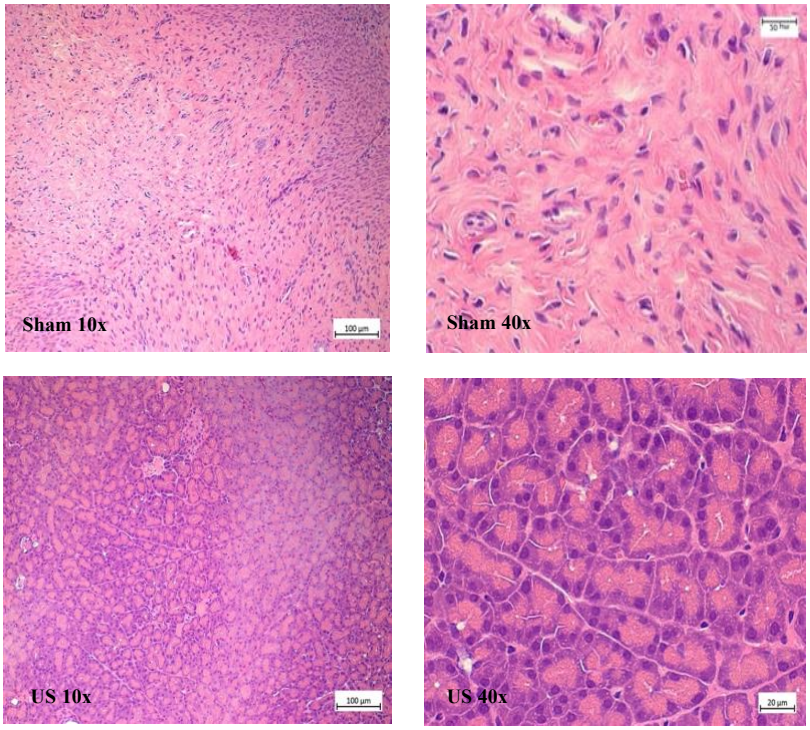

Figure 33: Histological Analysis of Sham vs. Ultrasound-Treated Rat Pancreases; Pancreases were minced in to 2 sections, 1 serving as a sham and the other exposed to ultrasound at 800 kHz at intensity of 0.5 W/cm^2 for 5 min continuously. Sections of 10x and 40x of both sham-treated and ultrasound-treated pancreases appear next to each other in the figure.

6.3 Discussion

The lack of observed change in the US-treated pancreases compared to the sham-treated pancreas, as indicated by the H&E staining results, suggests that ultrasound (US) treatment did not elicit significant alterations in pancreatic tissue morphology. This finding is crucial for understanding the potential impact of US therapy on pancreatic health.

Several factors could have contributed to the absence of deleterious effects on the pancreas samples. Firstly, the parameters of the ultrasound treatment, such as frequency, intensity, and duration, might not have been sufficient to induce noticeable alterations in pancreatic tissue. Studies have shown that different ultrasound parameters can lead to varying biological responses, and optimization of these parameters is crucial for achieving desired effects [37], [144]. For example, a study done by Pascoal et al., strived to identify the optimal ultrasound parameters to stimulate viability, proliferation and protein expression of osteoblasts. It was found that parameters of 1 MHz with varying intensities of 0.3-0.6 W/cm^2 for 5 min continuously significantly and consistently improved metabolic activity, while maintaining expression an synthesis of the tested osteoblasts [144]. Furthermore, the inherent resilience of pancreatic tissue to external stimuli could also explain the lack of observed changes. The pancreas is composed of various cell types organized into complex structures, and its inherent regenerative capacity might mitigate the effects of external interventions such as ultrasound therapy [145]. Additionally, the timing of tissue analysis post-treatment could influence the observed outcomes [146]. It's possible that significant changes in tissue morphology might occur at later time points beyond the scope of this study. Longitudinal studies assessing the effects of US therapy over extended periods could provide valuable insights into the temporal dynamics of tissue response.

6.4 Conclusions

The absence of discernible changes in the US-treated pancreases compared to the sham-treated pancreas suggests that ultrasound therapy did not induce significant morphological alterations in pancreatic tissue under the conditions tested. However, further

investigations incorporating comprehensive histological analyses, along with experimentation with varying ultrasound parameters and longitudinal studies, are warranted to fully elucidate the effects of ultrasound therapy on pancreatic health. Considering this, the selected ultrasound parameters do not indeed cause any harmful effects, supporting ultrasound's safe application to tissue.

References

[1] Centers for Disease Control and Prevention, "What is Diabetes?," Centers for Disease Control and Prevention website. [Online]. Available: https://www.cdc.gov/diabetes/basics/diabetes.html#:~:text=More%20than%2037%20million%20US,limb%20amputations%2C%20and%20adult%20blindness.

[2] R. Z. Alicic, M. T. Rooney, and K. R. Tuttle, "Diabetic kidney disease," *Clin J Am Soc Nephrol*, vol. 12, pp. 2032-2045.

[3] Centers for Disease Control and Prevention, "Type 2 Diabetes," Centers for Disease Control and Prevention website. [Online]. Available: https://cdc.gov/diabetes/basics/type2.html#:~:text=More%20than%2037%20million%20Americans,adults%20are%20also%20developing%20it.

[4] M. S. Islam, "The islets of Langerhans," *Adv Exp Med Biol*, 2010.

[5] S. E. Kahn, M. E. Cooper, and S. Del Prato, "Pathophysiology and treatment of type 2 diabetes: Perspectives on the past, present, and future," *Lancet*, 2014.

[6] "The pancreas and its functions," Pancreas Functions, Location & Disease | Columbia Surgery. [Online]. Available: https://columbiasurgery.org/pancreas/pancreas-and-its-functions.

[7] Talathi SS, Zimmerman R, Young M, “Anatomy, abdomen and pelvis, pancreas,” *StatPearls*, 2024.

[8] G. Wilcox, "Insulin and insulin resistance," *Clin Biochem Rev*, vol. 26, no. 2, pp. 19-39, 2005.

[9] "Hyperglycemia in diabetes," Mayo Clinic. [Online]. Available: https://www.mayoclinic.org/diseases-conditions/hyperglycemia/symptoms-causes/syc-20373631.

[10] A. M. Y. Zhang et al., "Hyperinsulinemia in obesity, inflammation, and cancer," *Diabetes Metab J,* vol. 45, no. 3, pp. 285-311, 2021.

[11] "Diabetes Type 2: Nothing Sweet About It," ATrain Education. [Online]. Available: https://www.atrainceu.com/content/4-regulation-blood-glucose.

[12] "Once-weekly Ozempic® (SEMAGLUTIDE) injection mechanism of action," novoMEDLINK. [Online]. Available: https://www.novomedlink.com/diabetes/products/treatments/ozempic/about/mechanism-ofaction.html#:~:text=Ozempic%C2%AE%20acts%20as%20a,target%20for%20native%

20GLP%2D1.&text=Ozempic%C2%AE%20lowers%20fasting%20and,in%20a%20glucose%2Ddependent%20manner.

[13] D. Miller et al., "Overview of therapeutic ultrasound applications and safety considerations," *J Ultrasound Med*, vol. 31, pp. 623-634, 2012.

[14] R. Akter et al., "Islet amyloid polypeptide: structure, function, and pathophysiology," *J Diabetes Res,* vol. 2016, p. 2798269.

[15] C. E. Higham et al., "Processing of synthetic pro-islet amyloid polypeptide (proIAPP) 'amylin' by recombinant prohormone convertase enzymes, PC2 and PC3, in vitro," *Eur J Biochem*, vol. 267, no. 16, pp. 4998-5004, 2000.

[16] X. X. Zhang et al., "Neuroendocrine hormone amylin in diabetes," *World J Diabetes*, vol. 7, no. 9, pp. 189-197, 2016.

[17] E. G. Mietlicki-Baase, "Amylin-mediated control of glycemia, energy balance, and cognition," *Physiol Behav*, vol. 162, pp. 130-140, 2016.

[18] S. C. Woods et al., "Pancreatic signals controlling food intake; insulin, glucagon and amylin," *Philos Trans R Soc Lond Biol Sci*, vol. 361, no. 1471, pp. 1219-1235, 2006.

[19] M. Press et al., "Protein aggregates and proteostasis in aging: amylin and β-cell function," *Mech Ageing Dev*, vol. 177, pp. 91-30, 2018.

[20] L. Hieronymus and S. Griffin, "Role of amylin in type 1 and type 2 diabetes," *Diabetes Edu*, vol. 41, pp. 47-56, 2015.

[21] A. Serbis et al., "Beta cell dysfunction in youth- and adult-onset type 2 diabetes: an extensive narrative review with a special focus on the role of nutrients," *Nutrients*, vol. 15, no. 9, pp. 2217, 2023.

[22] C. N. Boyle, Y. Zheng, and T. A. Lutz, "Mediators of amylin action in metabolic control," *J Clin Med,* vol. 11, no. 8, pp. 2207, 2022.

[23] M. Wang et al., "Role of the unfolded protein response regulator GRP78/BiP in development, cancer, and neurological disorders," *Antioxid Redox Signal*, vol. 11, no. 9, pp. 2307-2316, 2009.

[24] S. Trzos, L. Link-Lenczowski, and E. Pochec, "The role of N-glycosylation in B-cell biology and IgB activity. The aspects of auto-immunity and anti-inflammatory therapy," *Front Immunol*, vol. 14, pp. 1188838, 2023.

[25] G. E. Karagoz, D. Acosta-Alvear, and P. Walter, "The unfolded protein response: detecting and responding to fluctuations in the protein-folding capacity of the

endoplasmic reticulum," *Cold Spring Harb Perspect Biol*, vol. 11, no. 9, pp. a033886, 2019.

[26] L. Daverkausen-Fischer and F. Prols, "Regulation of calcium homeostasis and flux between the endoplasmic reticulum and the cytosol," *J Biol Chem*, vol. 298, no. 7, pp. 102061, 2022.

[27] "The History of Ultrasound," BMUS, [Online]. Available: https://www.bmus.org/for-patients/history-of-ultrasound/.

[28] A. Carovac et al., "Application of ultrasound in medicine," *Acta Inform Med*, vol. 19, no. 3, pp. 168-171, 2011.

[29] W. D. O'Brien, "Ultrasound—biophysics mechanisms," *Prog Biophys Mol Biol*, vol. 93, no. 1-3, pp. 212-255, 2006.

[30] OpenStax College, "Ultrasound," Ultrasound | Physics, [Online]. Available: https://courses.lumenlearning.com/suny-physics/chapter/17-7-ultrasound/.

[31] Shin SJ, Jeong BJ, "Principle and comprehension of ultrasound imaging," *The Journal of the Korean Orthopaedic Association*, vol. 48, no. 5, pp. 325.

[32] J. T. Bushberg et al., "The essential physics of medical imaging: Ultrasound, Second Edition," Philadelphia, PA, Lippincott Williams & Wilkins, 2002, pp. 469-483.

[33] A. Pasquarello, "Near Field and Far Field," RP Photonics Encyclopedia of Laser Physics and Technology, 2008. [Online]. Available: https://www.rp-photonics.com/near_field_and_far_field.html. [Accessed: March 24, 2024].

[34] M. U. College, "Lecture Notes on Ultrasound Beam Shape," University of Mosul, 2022. [Online]. Available: https://uomus.edu.iq/img/lectures21/MUCLecture_2022_8174368.pdf. [Accessed: March 24, 2024].

[35] Pitt WG, Husseini GA, Staples BJ, "Ultrasonic drug deliver—a general review," *Expert Opin Drug Deliv*, vol. 1, no. 1, pp. 37-56, 2004.

[36] Gao W, et al., "Study of ultrasonic near-field region in ultrasonic liquid-level monitoring system," *Micromachines*, vol. 11, no. 8, pp. 763, 2020.

[37] T. J. Mason, "Therapeutic ultrasound: an overview," *Ultrasonics Sonochemistry*, vol. 18, no. 4, pp. 847-852, 2011.

[38] A. Shanei and A. Sazgarnia, "An overview of therapeutic applications of ultrasound based on synergetic effects with gold nanoparticles and laser excitation," *Iran J Basic Med Sci*, vol. 22, no. 8, pp. 848-855, 2019.

[39] C. M. I. Quarato, D. Lacedonia, and M. Salvemini, "A review on biological effects of ultrasounds: key messages for clinicians," *Diagnostics (Basel)* vol. 13, pp. 855, 2023.

[40] I. M. Suarez Castellanos, B. Balteanu, T. Singh, and V. Zderic, "Therapeutic modulation of calcium dynamics using ultrasound and other energy-based techniques," *IEEE Rev Biomed Eng*, 2016.

[41] W. J. Elias et al., "A Randomized Trial of Focused Ultrasound Thalamotomy for Essential Tremor," *N Engl J Med*, 2016.

[42] T. Nishida et al., "Low-intensity pulsed ultrasound (LIPUS) treatment of cultured chondrocytes stimulates production of CCN family protein 2 (CCN2), a protein involved in the regeneration of articular cartilage: mechanism underlying this stimulation," *Osteoarthr Cartil*, 2017.

[43] M. J. Page, D. O'Connor, V. Pitt, and N. Massy-Westropp, "Therapeutic ultrasound for carpal tunnel syndrome," *Cochrane Database Syst Rev*, 2013.

[44] R. Alkins and K. Hynynen, "Physical medicine and rehabilitation," in *Comprehensive Biomedical Physics*, 2014.

[45] H. G. Flynn, "Physics of acoustic cavitation in liquids," *Physical Acoustics*, W. P. Mason, Ed., vol. 1B, New York: Academic, 1964, ch. 9.

[46] H. G. Flynn, "Generation of transient cavities in liquids by microsecond pulses of ultrasound," *J Acoust Soc Am*, vol. 72, pp. 1926–1932, 1982.

[47] Seol SH, Lindner JR, “A primer on the methods and applications for contrast echocardiography in clinical imaging,” *Journal of Cardiovascular Ultrasound*, vol. 22, no. 3, pp. 101-110, 2014.

[48] National Council on Radiation Protection and Measurements (NCRP), "Exposure Criteria for Medical Diagnostic Ultrasound: II. Criteria Based on All Known Mechanisms," Bethesda, MD: Natl. Counc. Radiat. Prot., 2002.

[49] American Institute of Ultrasound in Medicine, "Mechanical bioeffects from diagnostic ultrasound: AIUM consensus statements," *J Ultrasound Med*, vol. 19, pp. 68–153, 2000.

[50] D. Maresca et al., "Biomolecular Ultrasound and Sonogenetics," *Annu Rev Chem Biomol Eng*, 2018.

[51] D. I. Piraner et al., "Tunable thermal bioswitches for in vivo control of microbial therapeutics," *Food, Pharmaceutical and Bioengineering Division 2017 - Core Programming Area at the 2017 AIChE Annual Meeting*, 2017.

[52] W. Hundt et al., "In Vitro Effect of Focused Ultrasound or Thermal Stress on HSP70 Expression and Cell Viability in Three Tumor Cell Lines," *Acad Radiol*, 2007.

[53] R. Ogawa et al., "Enhancement of artificial promoter activity by ultrasound-induced oxidative stress," *Ultrason Sonochem,* 2009.

[54] R. Ogawa et al., "Regulation of gene expression in human prostate cancer cells with artificially constructed promoters that are activated in response to ultrasound stimulation," *Ultrason Sonochem*, 2013.

[55] C. H. Hou, T. W. Tan, and C. H. Tang, "AMP-activated protein kinase is involved in COX-2 expression in response to ultrasound in cultured osteoblasts," *Cell Signal*, 2008.

[56] SpecialtyCare, "The History of Perfusion," [Online]. Available: https://specialtycareus.com/the-history-of-perfusion/#:~:text=The%20History%20of%20Perfusion,perfusion%20process%20we%20know%20today.

[57] "An Intense Focus on Perfusion," *The Medicine Maker*. [Online]. Available: https://themedicinemaker.com/manufacture/an-intense-focus-on-perfusion#:~:text=One%20of%20the%20key%20advantages,fed%2Dbatch%20and%20perfusion%20processing.

[58] D. A. Gaspar et al., "The role of perfusion bioreactors in bone tissue engineering," *Biomatter*, vol. 2, no. 4, pp. 1-9, 2012.

[59] Thorn-Cole H, Marison IW, Demont A, “The application of dielectric spectroscopy and biocalorimetry for the monitoring of biomass in immobilized mammalian cell cultures,” *Processes*, vol. 3, no. 2, pp. 384-405, 2015.

[60] C. Alcaraz et al., "Microenvironmental control of malignancy by a complex network of tissue interactions," *Evid Based Complement Alternat Med*, 2011.

[61] PreciGenome, "Perfusion System Guide Review." [Online]. Available: https://www.precigenome.com/perfusion-system-guide-review

[62] A. Cacciamali et al., “3D cell cultures: evolution of an ancient tool for new applications,” *Front Physiol*, vol. 13, 2022.

[63] D. L. Hughes, “Dynamic physiological culture of human tissue: a systematic review,” *Cancers (Basel)*, vol. 13, no. 12, pp. 2870, 2021.

[64] C. W. Yoon et al., “Investigation of ultrasound-mediated intracellular Ca2+ oscillations in HIT-T15 pancreatic β-cell line,” *Cells*, vol. 9, no. 5, pp. 1129, 2020.

[65] A. Assmann et al., “Growth factor control of pancreatic islet regeneration and function,” *Pediatr Diabetes*, vol. 10, no. 1, pp. 14-32, 2008.

[66] D. Dalecki, “Mechanical bioeffects of ultrasound,” *Annu Rev Biomed Eng*, vol. 6, pp. 229-248, 2004.

[67] G. Basta et al., “In vitro modulation of intracellular oxidative stress of endothelial cells by diagnostic cardiac ultrasound,” *Cardiovasc Res*, vol. 58, pp. 156–161, 2003.

[68] A. F. Tarantal et al., “Hematologic and growth-related effects of frequent prenatal ultrasound exposure in the long-tailed macaque (Macaca fascicularis)’, *Ultrasound Med Biol*, vol. 21, pp. 1073–1081, 1995.

[69] J. O. Szablowski et al., “Acoustically targeted chemogenetics for the non-invasive control of neural circuits,” *Nature*, vol. 2, pp. 475-484, 2018.

[70] M. Razavi et al., “Effect of pulsed focused ultrasound on the native pancreas,” *Ultrasound in Med & Biol*, vol. 46, no. 3, pp. 630-638, 2020.

[71] M. Razavi et al., "Improving the function and engraftment of transplanted pancreatic islets using pulsed focused ultrasound therapy," *Sci Rep*, 2019.

[72] I. Suarez Castellanos et al., "Ultrasound Stimulation of Insulin Release from Pancreatic Beta Cells as a Potential Novel Treatment for Type 2 Diabetes," *Ultrasound Med Biol*, 2017.

[73] I. S. Castellanos et al., "Calcium-dependent ultrasound stimulation of secretory events from pancreatic beta cells," *J Ther Ultrasound*, 2017.

[74] B. Svendsen et al., "Insulin secretion depends on intra-islet glucagon signaling," *Cell Reports*, vol. 25, pp. 1127-1134, 2018.

[75] I. Suarez-Castellanos et al., "Effect of therapeutic ultrasound on the release of insulin, glucagon, and alpha-amylase from ex vivo pancreatic models," *J Ultrasound Med*, vol. 40, no. 12, pp. 2709-2719, 2021.

[76] M. Kaprinska and M. Czauderna, "Pancreas—its functions, disorders, and physiological impact on the mammals’ organism," *Front Physiol*, vol. 13, 2022.

[77] "Neuromodulation," Focused Ultrasound Foundation, [Online]. Available: https://www.fusfoundation.org/the-technology/mechanisms-of-action/neuromodulation/#:~:text=Such%20techniques%20hold%20promise%20in,precise%20areas%20of%20the%20brain.

[78] A. Guerra and M. Bologna, "Low-intensity transcranial ultrasound stimulation: mechanisms of action and rationale for future applications in movement disorders," *Brain Sci*, vol. 15, no. 5, pp. 611, 2022.

[79] W. Lee et al., "Transcranial Focused Ultrasound Stimulation of Motor Cortical Areas in Freely-Moving Awake Rats," *BMC Neurosci*, 2018.

[80] ZYMO Research, "Direct-zol RNA miniprep," [Online]. Available: https://files.zymoresearch.com/protocols/_r2050_r2051_r2052_r2053_direct-zol_rna_miniprep.pdf.

[81] ThermoFisher Scientific, "High-Capacity cDNA Reverse Transcription Kit," [Online]. Available: https://www.thermofisher.com/order/catalog/product/4368814.

[82] Qiagen, "RNeasy Plus Mini Kit Quick-Start Protocol," [Online]. Available: https://www.qiagen.com/us/products/discovery-and-translational-research/dna-rna-purification/rna-purification/total-rna/rneasy-plus-kits.

[83] R. Deckers et al., "Image-guided, noninvasive, spatiotemporal control of gene expression," *Proc Natl Acad Sci U S A*, 2009; 106: 1175-1180.

[84] A.H. Olsson et al., "Genome-wide associations between genetic and epigenetic variation influence mRNA expression and insulin secretion in human pancreatic islets," *PLoS Genet*, 2014.

[85] D.C. Bhowmick et al., "Molecular mechanisms of amylin turnover, misfolding and toxicity in the pancreas," *Molecules*, 2022; 27: 1021.

[86] B. Treeby, "k-Wave: A MATLAB Toolbox," [Online]. Available: http://www.k-wave.org/.

[87] S. Afzal et al., "Ultrasound hydrogel: a review on materials and method," *J Mod Polym Chem Matter*, vol. 1, no. 1, pp. 2, 2022.

[88] Kinsler's Fundamentals of Acoustics, 4th ed, p. 218.

[89] "Calculla - Online Calculators and Tools," [Online]. Available: https://calculla.com/sound_velocity_table.

[90] "Aqua-Calc - The Professional's Choice for Online Conversion Calculators," [Online]. Available: https://www.aqua-calc.com/page/density-table/substance/polymethyl-blank-methacralate-blank--op-plexiglass-cp-.

[91] "Study.com," [Online]. Available: https://study.com/academy/lesson/the-absorption-coefficient-definition-

calculation.htmlspectrum/index.html#:~:text=Composition,absorbs%20between%205%2D10%25.

[92] M. D. Gray et al., "Sound speed and attenuation of human pancreas and pancreatic tumors and their influence on focused ultrasound thermal and mechanical therapies," *Med Phys*, 2023.

[93] S. A. Lopez-Haro et al., "Ultrasonic characterization of cell culture medium in the temperature range from 25 C to 50 C," *IEEE*, 2012.

[94] C. Poon, "Measuring the density and viscosity of culture media for optimized computational fluid dynamics analysis of in vitro devices," *J Mech Behav Biomed Mater*, vol. 126, 2022.

[95] J. C. Zwinkels, W. F. Davidson, and C. X. Dodd, "Optical properties of UV transmitting acrylics for use in a heavy water Cerenkov detector," *Appl Opt*, vol. 29, pp. 3240-3248, 1990.

[96] A. Chen et al., "Ex vivo imaging of ultrasound-stimulated metabolic activity in rat pancreatic slices," *Ultrasound Med Biol*, vol. 47, no. 3, pp. 666-678, 2020.

[97] R. V. Dukkipati, "Mechanical Vibrations," 2nd ed., 2010.

[98] University of North Georgia, "Chapter 5 thermochemistry - University of North Georgia," 2015. [Online]. Available: https://web.ung.edu/media/chemistry/Chapter5/Chapter5-Thermochemistry.pdf.

[99] J. Kim et al., "Acoustic and thermal characterization of therapeutic ultrasonic langevin transducers under continuous-and pulse wave excitations," *Sensors*, vol. 22, no. 22, pp. 9006, 2022.

[100] B. J. Levenback and C. M. Sehgal, "Modeling of thermal effects in antivascular ultrasound therapy," *J Acoust Soc Am*, vol. 131, no. 1, pp. 540-549, 2012.

[101] V. E. Brunt and C. T. Minson, "Heat therapy: mechanistic underpinnings and applications to cardiovascular health," *J Appl Physiol*, vol. 130, no. 6, pp. 1684-1704, 1985.

[102] Leinco Technologies, "Sandwich Elisa protocol," 2021. [Online]. Available: https://www.leinco.com/sandwich-elisa-protocol/.

[103] The Native Antigen Company, "Streptavidin-HRP Conjugate," 2022. [Online]. Available: https://thenativeantigencompany.com/products/streptavidin-hrp-conjugate/#:~:text=Streptavidin%2DHRP%20conjugate%20is%20a,primary%20antibodies%20in%20immunoassay%20applications.

[104] AAT Bioquest, "Home," [Online]. Available: https://www.aatbio.com/resources/faq-frequently-asked-questions/Why-is-TMB-used-in-conjunction-with-HRP-in-ELISA.

[105] Cell Signaling Technology, "Stop solution," 2019. [Online]. Available: https://www.cellsignal.com/products/buffers-dyes/stop-solution/7002#:~:text=STOP%20Solution%20is%20a%20proprietary,to%20produce%20a%20blue%20solution.

[106] P. Lindner, et al., “Cell death induced by the ER stressor thapsigargin involves death receptor 5, a non-autophagic function of MAP1LC3B, and distinct contributions from unfolded protein response components,” *Cell Commun and Signaling*, vol. 18, no. 12, 2020.

[107] P. Sehgal et al., "Inhibition of the sarco/endoplasmic reticulum (ER) Ca2+-ATPase by thapsigargin analogs induces cell death via ER Ca2+ depletion and the unfolded protein response," *J Biol Chem*, vol. 292, no. 48, pp. 19656-19673, 2017.

[108] M. Song, "Ultrasonic neuromodulation mediated by mechanosensitive ion channels: current and future," *Front Neurosci*, 2023, vol. 17.

[109] Y. C. Chu et al., "Activation of mechanosensitive ion channels by ultrasound," *Ultrasound In Med & Biol*, vol. 0, no. 0, pp. 1-14, 2022.

[110] C. Klec et al., "Calcium signaling in β-cell physiology and pathology: a revisit," *Int J Mol Sci*, vol. 20, no. 24, pp. 6110, 2019.

[111] R. Wang et al., "Insulin secretion of Ca2+ dynamics in β-cells are regulated by PERK (EIF2AK3) in concert with calcineurin," *J Biol Chem*, vol. 288, no. 47, pp. 33824-33836, 2013.

[112] F. M. Ashcroft and P. Rosman, "KATP channels and islet hormone secretion: new insights and controversies," *Nat Rev Endocrinol*, vol. 9, no. 11, pp. 660-669, 2013.

[113] P. Rosman et al., "The cell physiology of Biphasic insulin secretion," *News Physiol Sci*, vol. 15, pp. 0886-1714, 2000.

[114] L. E. Fridyland and L. H. Philipson, "Glucose sensing in the pancreatic beta cell: a computational systems analysis," *Theor Biol Med Model*, vol. 7, p. 15, 2010.

[115] S. T. Lewis et al., "A receptor story: insulin resistance pathophysiology and physiologic insulin resensitization’s role as a treatment modality," *Int J Mol Sci*, vol. 24, no. 13, p. 10927, 2023.

[116] J. C. Hou, L. Min, J. E. Pessin et al., "Insulin granule biogenesis, trafficking and exocytosis," *Vitam Horm*, vol. 80, pp. 473-506, 2009.

[117] S. Yoo et al., "Focused ultrasound excites cortical neurons via mechanosensitive calcium accumulation and ion channel amplification," *Nat Commun*, vol. 13, no. 493, 2022.

[118] K. T. Jones and G. R. Sharpe, "Thapsigargin raises intracellular free calcium levels in human keratinocytes and inhibits the coordinated expression of differentiation markers," *Exp Cell Res*, vol. 210, no. 1, pp. 71-76, 1994.

[119] P. Lindner et al., "Cell death induced by the ER stressor thapsigargin involves death receptor 5, a non-autophagic function of MAP1LC3B, and distinct contributions from unfolded protein response components," *Cell Commun Signal*, vol. 18, p. 12, 2020.

[120] Molina J, et al., "Control of insulin secretion by cholinergic signaling in the human pancreatic islet," *Diabetes*, vol. 63, no. 8, pp. 2174-2726, 2014.

[121] Mendez J. M., et al., "Activation of the endoplasmic reticulum stress response impacts the NOD1 signaling pathway," *Infect Immun*, vol. 87, no. 8, pp. e00826-18, 2019.

[122] Hülsmann S., et al., "Evaluation of a mechanical lung model to test small animal whole body plethysmography," *Sci Rep*, vol. 11, pp. 17099, 2021.

[123] M. Huang et al., "Evaluation of the transverse aortic constriction model in ICR and C57BL/6J mice," *Front Physiol*, vol. 13, p. 1026884, 2022.

[124] O. C. Dams et al., "Heart failure and pancreas exocrine insufficiency: pathophysiological mechanisms and clinical point of view," *J Clin Med*, vol. 11, no. 14, p. 4128, 2022.

[125] C. Riehle and E. D. Abel, "Insulin signaling and heart failure," *Circ Res*, vol. 118, pp. 1151-1169, 2016.

[126] Chondrex, "Frequently asked questions about Elisas," 2022. [Online]. Available: https://www.chondrex.com/documents/ELISA-FAQ.pdf.

[127] R. D. Yudhani et al., "In vitro insulin resistance model: a recent update," *J Obes*, vol. 2023, p. 1964732, 2023.

[128] L. Chang, S. H. Chiang, and A. R. Saltiel, "Insulin signaling and the regulation of glucose transport," *Mol Med*, vol. 10, pp. 65-71, 2004.

[129] S. Y. Park, J. F. Gautier, and S. Chon, "Assessment of insulin secretion and insulin resistance in human," *Diabetes Metab J*, vol. 45, no. 5, pp. 641-654, 2021.

[130] R. D. Mattes et al., "Valuing the diversity of research methods to advance nutrition science," *Adv Nutr*, vol. 13, no. 4, pp. 1324-1393, 2022.

[131] S. J. L. Marchand and D. W. Piston, "Glucose decouples intracellular Ca2+ activity from glucagon secretion in mouse pancreatic islet alpha-cells," *PLoS One*, vol. 7, no. 10, pp. e47084, 2012.

[132] S. Shi and E. Liu, "Anatomy, histology and function of the pancreas," *Pathobiology of Human Disease*, 2014, pp. 2229-2242.

[133] S. G. Pierzynowski, C. Stier, and Pierzynowska, "Hypothesis that alpha-amylase evokes regulatory mechanisms originating in the pancreas, gut and circulation, which govern glucose/insulin homeostasis," *World J Diabetes*, vol. 14, no. 9, pp. 1341-1348, 2023.

[134] T. Hiyoshi et al., "Postprandial hyperglycemia and postprandial hypertriglyceridemia in type 2 diabetes," *J Biomed Res*, vol. 33, no. 1, pp. 1-16, 2017.

[135] M. D. Sans, "Pancreatic digestive enzyme synthesis and its translational control," *Pancreapedia: Exocrine Pancreas Knowledge Base*, 2021.

[136] M. Amherdt, Y. Patel, and L. Orci, "Binding and internalization of somatostatin, insulin, and glucagon by cultured rat islet cells," *J Clin Invest*, vol. 84, pp. 412-417, 1989.

[137] L. Orci et al., "Exocytosis-endocytosis coupling in the pancreatic beta cell occurs concomitantly, and consequently predator-prey interactions in continuous culture," *Science (80-)*, vol. 181, pp. 561-562, 1973.

[138] L. Eliasson et al., "Endocytosis of secretory granules in mouse pancreatic fl-cells evoked by transient elevation of cytosolic calcium cell preparation," *J Physiol*, vol. 493, pp. 755-767, 1996.

[139] K. Morishita et al., "Effects of therapeutic ultrasound on range of motion and stretch pain," *J. Phys Ther Sci*, vol. 26, no. 5, pp. 711-715, 2014.

[140] P. Qin et al., "Mechanistic understanding the bioeffects of ultrasound-driven microbubbles to enhance macromolecule delivery," *J. Controlled Release*, vol. 272, pp. 169-181, 2018.

[141] S. B. Barnett et al., "The sensitivity of biological tissue to ultrasound," *Ultrasound Med Biol*, vol. 23, no. 6, pp. 805-812, 1997.

[142] J. Shreffer and M. R. Huecker, "Type I and type II errors and statistical power," *StatPearls*, 2024.

[143] C. Sampias and G. Rolls, "H&E staining overview: A guide to best practices," An Intro to H&E Staining: Protocol, Best Practices, Steps & More, 2021. [Online]. Available: https://www.leicabiosystems.com/us/knowledge-pathway/he-staining-overview-a-guide-to-best-practices/.

[144] S. Pascoal et al., "Influence of ultrasound stimulation on the viability, proliferation and protein expression of osteoblasts and periodontal ligament fibroblasts," *Biomedicines*, vol. 12, no. 2, pp. 361, 2024.

[145] Q. Zhou and D. A. Melton, "Pancreas regeneration," *Nature*, vol. 557, no. 7705, pp. 351-358, 2018.

[146] M. J. Mueller and K. S. Maluf, "Tissue adaptation to physical stress: a proposed “physical stress theory” to guide physical therapist practice, education, and research," *Phys Ther*, vol. 82, no. 4, pp. 383-403, 2002.

Appendices

Appendix I

MATLAB Script

```
%simulation testing the pressure and thermal effects of treating insulinoma
beta cells with
% ultrasound in a perfusion chamber.
% Written by JH & JNM
clearvars;

% =========================================================================
% SIMULATION
% =========================================================================
% define the PML size.
pml_size = 20;              % [grid points]

%create grid such that y is 25 mm. x gel layer: 0.5 mm, x glass layer: 0.5 mm,
x
% x ins layer = .01mm, media layer= 3 mm,  plexiglass layer = 3 x layer =
7.01mm


%Choose nx and ny: 300 points in each direction. x*300 = 7.01 mm, and y*300 =
25 mm.
%solve for x and y to set dx,dy


 Nx = 320 - pml_size;    % [grid points]
 Ny = 320 - pml_size;    % [grid points]
 dx = 0.02337e-3;               % [m]
 dy = 0.083333e-3;               % [m]

% define the properties of the propagation medium
medium.sound_speed = 1500 * ones(Nx, Ny);   % [m/s] gel
medium.sound_speed((22):(43), :) = 1700;       % [m/s] glass coverslip
medium.sound_speed((44):(45), :) = 1591;       % [m/s] ins
medium.sound_speed((46):(174), :) = 1525;       % [m/s] media
medium.sound_speed((175):300, :) = 1700;       % [m/s] plexiglass



medium.density = 1000 * ones(Nx, Ny);   % [kg/m^3] gel
medium.density((22):(43), :) = 1190;       % glass coverslip
medium.density((44):(45), :) = 1087;       %  ins
medium.density((46):(174), :) = 1000;       % media
medium.density((175):300, :) = 1190;       %  plexiglass
```

```
medium.alpha_coeff = .0022 * ones(Nx, Ny);   % [db/cm] gel
medium.alpha_coeff((22):(43), :) = 0.6;       % glass coverslip
medium.alpha_coeff((44):(45), :) = 0.7904;       %  ins
medium.alpha_coeff((46):(174), :) = 0.0022;       % media
medium.alpha_coeff((175):300, :) = 0.51;       %  plexiglass


medium.alpha_power = 1.5;   % ins


% create the computational grid
kgrid = kWaveGrid(Nx, dx, Ny, dy);


%creates a "sandwich". This is to help visualize the simulation space by
%material.
figure;
imagesc(medium.sound_speed);
colorbar;
title('medium sound speed');
xlabel('x');
ylabel('y');
%% CW

%define the source parameters. change to driving force used in the lab.
%twice the size of the treatment area
diameter = 0;           % [m]
radius   = 7.50e-3;           % [m]
freq     = 800000;            % [Hz]
amp      = 0.182e6;        % [Pa]



% define a  ultrasound transducer. need to change to match the
% transducer shape used in the lab
source.p_mask = makeArc([Nx, Ny], [1, Ny/2], round(radius / dx),
round(diameter / dx) + 1, [Nx/2, Ny/2]);


% calculate the time step using an integer number of points per period
ppw = 2651 / (freq * dx); % points per wavelength. Choose highest medium sound
speed to ensure nothing is missed.
cfl = 0.3;                                % cfl number
ppp = ceil(ppw / cfl);                    % points per period
T   = 1 / freq;                           % period [s]
dt  = T / ppp;                            % time step [s]

% calculate the number of time steps to reach steady state
%t_end = sqrt( kgrid.x_size.^2 + kgrid.y_size.^2 ) / medium.sound_speed;
t_end = sqrt( kgrid.x_size.^2 + kgrid.y_size.^2 ) / 1520;
Nt = round(t_end / dt);

% create the time array
kgrid.setTime(Nt, dt);
```

```
% define the input signal
source.p = createCWSignals(kgrid.t_array, freq, amp, 0);

% set the sensor mask to cover the entire grid
sensor.mask = ones(Nx, Ny);
sensor.record = {'p', 'p_max_all'};

% record the last 3 cycles in steady state
num_periods = 3;
T_points = round(num_periods * T / kgrid.dt);
sensor.record_start_index = Nt - T_points + 1;

% set the input arguments
input_args = {'PMLInside', false, 'PlotPML', false, 'DisplayMask', ...
    'off', 'PlotScale', [-1, 1] * amp};

% run the acoustic simulation
sensor_data = kspaceFirstOrder2D(kgrid, medium, source, sensor,
input_args{:});

% =========================================================================
% CALCULATE HEATING
% =========================================================================

% convert the absorption coefficient to nepers/m
alpha_np = db2neper(medium.alpha_coeff, medium.alpha_power) * ...
    (2 * pi * freq).^medium.alpha_power;

% extract the pressure amplitude at each position
p = extractAmpPhase(sensor_data.p, 1/kgrid.dt, freq);

% reshape the data, and calculate the volume rate of heat deposition
p = reshape(p, Nx, Ny);
Q = alpha_np .* p.^2 ./ (medium.density .* medium.sound_speed);



%% OR PW: This would need a cluster to run at the same accuracy as the CW,
assuming everything else is kept the same

diameter = 0;           % [m]
radius   = 7.50e-3;           % [m]
freq     = 800000;            % [Hz]
amp      = .01;              % [Pa]

source.p_mask = makeArc([Nx, Ny], [1, Ny/2], round(radius / dx),
round(diameter / dx) + 1, [Nx/2, Ny/2]);


% Set up simulation parameters
ppw = 2651 / (freq * dx); % points per wavelength
cfl = 0.3;                % cfl number
ppp = ceil(ppw / cfl);    % points per period
T   = 1 / freq;           % period [s]
dt  = T / ppp;            % time step [s]
```

```
%dt = 1/freq; %save memory
t_end = sqrt(kgrid.x_size.^2 + kgrid.y_size.^2) / 1520;
Nt = round(t_end / dt);
kgrid.setTime(Nt, dt);
disp(dt);


%0.5 Hz Pulse Repetition frequency. 5% duty cycle. 5 minute treatment length.
%D = PW/T Duty cycle = pulse width / Time period of cycle.

% Create tone burst signal
t_on = 0.125; % [s]
t_off = 0.025; % [s]
num_cycles = 1;
t_total = num_cycles * (t_on + t_off); % [s]
t = 0:dt:t_total;
signal = toneBurst(1/dt, freq, t_on, 'SignalOffset', t_off);

% Repeat tone burst signal for the duration of the simulation
num_repeats = 100;
signal = repmat(signal, 1, num_repeats);
%signal = signal(1:length(t));
signal = signal(1:15);

% Scale signal amplitude
signal = amp * signal;

% Assign signal to source
source.p = signal;

sensor.mask = ones(Nx, Ny);
sensor.record = {'p', 'p_max_all'};

num_periods = 3;
T_points = round(num_periods * T / kgrid.dt);
sensor.record_start_index = Nt - T_points + 1;

input_args = {'PMLInside', false, 'PlotPML', false, 'DisplayMask', ...
    'off', 'PlotScale', [-1, 1] * amp};

sensor_data = kspaceFirstOrder2D(kgrid, medium, source, sensor,
input_args{:});


% =========================================================================
% CALCULATE HEATING
% =========================================================================

% convert the absorption coefficient to nepers/m
alpha_np = db2neper(medium.alpha_coeff, medium.alpha_power) * ...
    (2 * pi * freq).^medium.alpha_power;

% extract the pressure amplitude at each position
p = extractAmpPhase(sensor_data.p, 1/kgrid.dt, freq);
```

```
% reshape the data, and calculate the volume rate of heat deposition
p = reshape(p, Nx, Ny);
Q = alpha_np .* p.^2 ./ (medium.density .* medium.sound_speed);



%%

% =========================================================================
% THERMAL SIMULATION
% =========================================================================

% clear the input structures
clear medium source sensor;

% set the background temperature and heating term
source.Q = Q;
source.T0 = 37; %incubator temp in Celsius

% define medium properties related to diffusion. thermal properties of
% INS cells


medium.density = 1000 * ones(Nx, Ny);   % [kg/m^3] gel
medium.density((22):(43), :) = 1190;       % glass coverslip
medium.density((44):(45), :) = 1087;       %  ins
medium.density((46):(174), :) = 1000;       % media
medium.density((175):300, :) = 1190;       %  plexiglass


medium.thermal_conductivity = 0.6 * ones(Nx, Ny);   % [W/(m.K)] gel
medium.thermal_conductivity((22):(43), :) = 1.15;       % glass coverslip
medium.thermal_conductivity((44):(45), :) = 0.5;       %  media
medium.thermal_conductivity((46):(174), :) = 0.5;       % ins
medium.thermal_conductivity((175):300, :) = .19;       %  plexiglass


medium.specific_heat = 4184 * ones(Nx, Ny);   % [W/(m.K)] gel
medium.specific_heat((22):(43), :) = 830;       % glass coverslip
medium.specific_heat((44):(45), :) = 3500;       %  media
medium.specific_heat((46):(174), :) = 3164;       % ins
medium.specific_heat((175):300, :) = 1470;       %  plexiglass


% create kWaveDiffusion object
kdiff = kWaveDiffusion(kgrid, medium, source, []);

% set source on time and off time
on_time  = 300;  % [s]
off_time = 0;  % [s]

% set time step size
dt = 0.1;

% take time steps
```

```
kdiff.takeTimeStep(round(on_time / dt), dt);

% store the current temperature field. max temp (immediately after
% transducer ends)
T1 = kdiff.T;

% turn off heat source and take time steps (t2 is end of entire simulation
% after US and cooling).
kdiff.Q = 0;
kdiff.takeTimeStep(round(off_time / dt), dt);

% store the current temperature field
T2 = kdiff.T;

%%
% =========================================================================
% VISUALISATION
% =========================================================================

% plot the thermal dose and lesion map
figure;

% plot the acoustic pressure
imagesc(kgrid.y_vec * 1e3, kgrid.x_vec * 1e3, p * 1e-6);
h = colorbar;
xlabel(h, '[MPa]');
ylabel('x-position [mm]');
xlabel('y-position [mm]');
axis image;
title('Acoustic Pressure Amplitude');

figure;
% plot the volume rate of heat deposition
imagesc(kgrid.y_vec * 1e3, kgrid.x_vec * 1e3, Q * 1e-7);
h = colorbar;
xlabel(h, '[kW/cm^2]');
ylabel('x-position [mm]');
xlabel('y-position [mm]');
axis image;
title('Volume Rate Of Heat Deposition');

figure;
% plot the temperature after heating
imagesc(kgrid.y_vec * 1e3, kgrid.x_vec * 1e3, T1);
h = colorbar;
xlabel(h, '[degC]');
ylabel('x-position [mm]');
xlabel('y-position [mm]');
axis image;
title('Temperature After Heating');

figure;
% plot the temperature after cooling
imagesc(kgrid.y_vec * 1e3, kgrid.x_vec * 1e3, T2);
h = colorbar;
```

```
xlabel(h, '[degC]');
ylabel('x-position [mm]');
xlabel('y-position [mm]');
axis image;
title('Temperature After Cooling');

% % plot thermal dose
% subplot(2, 3, 5);
% imagesc(kgrid.y_vec * 1e3, kgrid.x_vec * 1e3, kdiff.cem43, [0, 1000]);
% h = colorbar;
% xlabel(h, '[CEM43]');
% ylabel('x-position [mm]');
% xlabel('y-position [mm]');
% axis image;
% title('Thermal Dose');

%Don't need this because  not ablating tissue, but it may helpful in
%future.

% % plot lesion map
% subplot(2, 3, 6);
% imagesc(kgrid.y_vec * 1e3, kgrid.x_vec * 1e3, kdiff.lesion_map, [0, 1]);
% colorbar;
% ylabel('x-position [mm]');
% xlabel('y-position [mm]');
% axis image;
% title('Ablated Tissue');

% set colormap and enlarge figure window
colormap(parula(256));
scaleFig(1.5, 1);
```